

A Particle-in-cell Method for Plasmas with a Generalized Momentum Formulation ^{*}

Andrew J. Christlieb [†] William A. Sands [‡] Stephen White [§]

Abstract

In this paper we formulate a new particle-in-cell method for the Vlasov-Maxwell system. Using the Lorenz gauge condition, Maxwell's equations for the electromagnetic fields are written as a collection of scalar and vector wave equations. The use of potentials for the fields motivates the adoption of a formulation for particles that is based on a generalized Hamiltonian. A notable advantage offered by this generalized formulation is the elimination of time derivatives of the potentials that are required in the standard Newton-Lorenz treatment of particles. This allows the fields to retain the full time-accuracy guaranteed by the field solver. The resulting updates for particles require only knowledge of the fields and their spatial derivatives. A method for constructing analytical spatial derivatives is presented that exploits the underlying integral solution used in the field solver for the wave equations. The field solvers considered in this work belong to a larger class of methods which are unconditionally stable, can address geometry, and leverage an $\mathcal{O}(N)$ fast summation method for efficiency, known as the Method of Lines Transpose (MOL^T). A time-consistency property of the proposed field solver for the vector potential form of Maxwell's equations is established, which ensures that the semi-discrete form of the proposed method satisfies the semi-discrete Lorenz gauge condition. We demonstrate the method on several well-established benchmark problems involving plasmas. The efficacy of the proposed formulation is demonstrated through a comparison with standard methods presented in the literature, including the popular FDTD method.

Keywords: Vlasov-Maxwell system, generalized Hamiltonian, particle-in-cell, method-of-lines-transpose, integral solution

1 Introduction

Particle-in-cell (PIC) methods [1, 2] have been extensively applied in numerical simulations of kinetic plasmas and are an important class of techniques used in the design of experimental devices including lasers, pulsed power systems, particle accelerators, among others [3]. The earliest work involving these methods began in the 1950s and 1960s, and it remains an active area of research to this day. At its core, a PIC method combines an Eulerian approach for the electromagnetic fields with a Lagrangian method that evolves collections of samples taken from general distribution functions in phase space. In other words, the fields are evolved using a mesh, while the distribution function is evolved using particles whose equations of motion are set according to characteristics of the partial differential equations (PDEs) used to evolve the distribution functions. Lastly, to combine the two approaches, an interpolation method is used to map data between the mesh and the particles. A typical selection for this map involves piece-wise constant or linear splines with tensor products being used to address multi-dimensional problems.

^{*}The research of the authors was supported by AFOSR grants FA9550-19-1-0281 and FA9550-17-1-0394, as well as NSF grant DMS-1912183.

[†]Department of Computational Mathematics, Science and Engineering, Michigan State University, East Lansing, MI, 48824, United States; christli@msu.edu.

[‡]Center for Predictive Engineering and Computational Science, Oden Institute for Computational Engineering and Sciences, The University of Texas at Austin, Austin, TX, 78712, United States; william.sands@austin.utexas.edu (corresponding author).

[§]Department of Computational Mathematics, Science and Engineering, Michigan State University, East Lansing, MI, 48824, United States; whites73@msu.edu.

The popularity of PIC methods in engineering applications can be largely attributed to its simplicity, efficiency, and capabilities in simulating complex nonlinear processes in plasmas. Early renditions of these methods were specifically constructed to circumvent the prohibitively expensive force calculation used to calculate the interactions between particles in electrostatic problems. The use of a mesh greatly simplifies the force calculation because the number of mesh points is typically smaller than the number of particles and fast algorithms exist to compute the potential. Simulation particles in these methods, which represent an ensemble of physical particles, are initialized by sampling from a prescribed probability distribution. A consequence of this sampling is that bulk processes in plasmas will be well represented, while the tails of the distribution will be largely underresolved even with good sampling methods. This, in turn, necessitates a large number of simulation particles for more systematic refinement studies to prevent certain numerical fluctuations. Realistic simulations of plasma devices have created a demand for new algorithms that simultaneously address the various challenges posed by accuracy constraints in modeling as well as scalability with new computational hardware [4]. The goal of this work is to supply new algorithms which aim to improve the computational efficiency of existing PIC methods for plasmas.

A comprehensive review of the literature for PIC methods up to 2005 can be found in the review article [5]. Much of the work highlighted by this reference is now largely considered standard, so, we shall emphasize more recent articles that are more aligned with the developments presented in this paper. Most PIC methods evolve the simulation particles explicitly using some form of leapfrog time integration along with the Boris rotation method [6] in the case of electromagnetic plasmas. The exploration of implicit PIC methods began in the 1980s [7, 8, 9]. These approaches suffered from a number of unattractive features, including issues with numerical heating and cooling [10], slow nonlinear convergence, and inconsistencies between the fluid moments and particle data. These approaches were later abandoned in favor of explicit treatments. Recent years have shown a resurgence of interest in implicit PIC methods [11, 12, 13]. In particular, the implicit PIC method proposed in [13] addressed many of these issues in the case of the Vlasov-Poisson system. Nonlinear convergence and self-consistency were enforced using a Jacobian-free Newton-Krylov method [14] with a novel fluid preconditioner [15] that enforced the continuity equation. The resulting solver demonstrated remarkable savings compared to explicit methods because they eliminated the need to resolve the charge separation in the plasma, allowing for a coarser mesh to be used. These techniques were later extended to curved geometries through the use of smooth grid mappings [16]. Recently, an effort has been made to extend these techniques to the full Vlasov-Maxwell system [17] to avoid the highly restrictive CFL condition posed by the gyrofrequency, as well as new with asymptotic-preserving particle treatments for particles [18, 19]. While these contributions are significant in their own right, there are many opportunities for improvement. Many of these methods are fundamentally stuck at second-order accuracy in both space and time and may greatly benefit from more accurate field solvers. Additionally, applications of interest involve complex geometries which introduce additional complications with stability and are often poorly resolved with uniform Cartesian meshes. Lastly, there is the concern of scalability. Krylov subspace methods pose a massive challenge for scalability on large machines due to the various collective operations used in the algorithms. It seems that the scalability of these methods could be significantly improved if similar implicit methods could be developed which eliminate the inner Krylov solve altogether, though this is beyond the scope of the present work.

A challenge associated with developing any solver for Maxwell's equations is the enforcement of the involutions for the fields, namely $\nabla \cdot \mathbf{E} = \rho/\epsilon_0$ and $\nabla \cdot \mathbf{B} = 0$. In the case of a structured Cartesian grid, Maxwell's equations can be discretized using a staggered grid technique introduced by Yee [20]. The use of a staggered mesh yields a structure-preserving discrete analogue of Maxwell's equations in integral form that automatically enforces the involutions for \mathbf{E} and \mathbf{B} without additional treatment. This is the basis of the well-known finite-difference time-domain method (FDTD) [21]. It is important to note that this is only true in the absence of moving charge. In the presence of moving charge, a linear current weighting will not satisfy the continuity equation $\nabla \cdot \mathbf{J} = -\frac{\partial \rho}{\partial t}$, so further cleaning is required in order to satisfy Gauss's law [22]. While the staggering in both space and time used in the FDTD method is second-order accurate, there exists a fourth-order extension of the spatial discretization that was developed as a way of dealing with certain dispersion errors known as Cerenkov radiation [23]. Pseudo-spectral type discretizations, free of numerical dispersion, have also been considered in simulations of relativistic plasmas [24, 25]. While the use of a staggered mesh with finite-differences is quite effective for Cartesian grids, issues arise in problems

defined with geometry, such as curved surfaces, in which one resorts to stair step boundaries [26]. To mitigate the effect of stair step boundaries in explicit methods, the mesh resolution is increased, resulting in a highly restrictive time step to meet the CFL stability criterion. Conformal PIC methods (see the review [27]) have been developed to address problems with geometry. In the case of cut-cell meshes, the time step will be limited by the size of the smallest cell, which can be prohibitively restrictive. This also applies to truly conformal PIC methods, which use smooth grid transformations to address curved boundaries [28]. Another approach for dealing with geometry in the Yee scheme, which avoids the stair stepping along the boundary, was developed for two-dimensional problems [29]. The grid cells along the boundary in the method are replaced with cut-cells which use generalized finite-difference updates that account for different intersections with the boundary. While this scheme was shown to be energy conserving, a more remarkable feature is that it eliminated the highly restrictive condition on the time step introduced by the cut-cells along the boundary. The theory in this article established half-order accuracy, yet demonstrated first-order accuracy in numerical experiments. While, these schemes have not yet been combined with PIC, they might eliminate some of the commonly encountered stability associated with cell-cells.

While many electromagnetic PIC methods solve Maxwell's equations on Cartesian meshes through the FDTD method, other methods have been developed specifically for addressing issues posed by geometries through the use of unstructured meshes. In [30], a finite-element method (FEM) was coupled with PIC to solve the Darwin model in which the fields move significantly faster than the plasma. Truly conformal PIC methods based on the FEM have also been considered to address problems concerning general geometries and parallel scalability [31]. Explicit finite-volume methods (FVM), which can address geometry, were considered in [32], which also developed divergence cleaning methods suitable for applications to PIC simulations of the Vlasov-Maxwell system. Discontinuous Galerkin (DG) methods have also been used to develop high-order PIC methods with elliptic [33] and hyperbolic [34] divergence cleaning methods being employed to enforce Gauss' law. Other work in this area has explored more generalized FEM discretizations to enforce charge conservation on arbitrary grids [35] as well as certain structure preserving discretizations [36, 37, 38]. In particular, [37, 38, 39] employed so called Whitney basis sets taken from the de Rham sequences to automatically enforce involutions for the electric and magnetic fields. Despite the advantages afforded by the use of such bases, these implicit field solvers rely on the solutions of large linear systems which need to be solved using GMRES [40]. Even with preconditioning, such methods can be slow and difficult to achieve scalability. In the case of explicit solvers, such as FVMs and DG methods, other challenges exist. The basic FVM, without additional reconstructions, is first-order in space. These methods can, of course, be improved to second-order accuracy by performing reconstructions based on a collection of cells. Beyond second-order accuracy, the reconstruction process becomes quite complicated due to the size of the interpolation stencils. DG methods, on the other hand, store cell-wise expansions in a basis, which eliminates the issue encountered in the FVM, typically at the cost of a highly restrictive condition on the size of a time step. Additionally, the significant amount of local work in DG methods makes them appealing for newer hardware, yet the restriction on the time step size is often left unaddressed. Notable exceptions to this restriction exist for the two-way wave equation including staggered formulations [41] and Hermite methods [42], which allow for a much larger time step. It will be interesting to see the performance of such methods in plasma problems, especially in problems with intricate geometric features.

Other methods for Maxwell's equations have been developed with unconditional stability for the time discretization. The first of these methods is the ADI-FDTD method [43, 44], which combined an ADI approach with a two-stage splitting to achieve an unconditionally stable solver. Time stepping in these methods was later generalized using a Crank-Nicolson splitting and several techniques for enhancing the temporal accuracy were proposed [45]. Of particular significance to this work are methods based on successive convolution, also known as the method-of-lines-transpose (MOL^T) [46, 47]. These methods are unconditionally stable in time and can be obtained by reversing the typical order in which discretization is performed. By first discretizing in time, one can solve a resulting boundary-value problem by formally inverting the differential operator using a Green's function in conjunction with a fast summation method. Mesh-free methods for plasmas [48] have also been developed, which have been extended to Maxwell's equations in the Darwin limit, under the Coulomb gauge [49, 50]. These formulations are in some ways similar to PIC in that they evolve particles with shapes, except no mesh is used in the simulation. The elliptic equations are solved using a Green's function on an unbounded domain and a fast summation method is used for efficiency. Green's

function methods have also been used to develop asymptotic preserving schemes [51]. This article utilized a boundary integral formulation with a multi-dimensional Green’s function, to obtain a method that recovers the Darwin limit under appropriate conditions. The methods considered in this work incorporate dimensional splittings, which results in algorithms with unconditional stability, high-order accuracy [52], parallel scalability [53] and geometric flexibility [54]. In [55], a PIC method was developed based on the MOL^T discretization combined with a staggered grid formulation of the Vlasov-Maxwell system. In this approach, the field equations were cast in terms of the Lorenz gauge, producing wave equations for the scalar and vector potentials. Additionally, the wave equation for the scalar potential was replaced with an elliptic equation to control errors in the gauge condition. Since the particle equations were written in terms of \mathbf{E} and \mathbf{B} , additional finite-difference derivatives were required to compute the electric and magnetic fields from the potentials. While the contributions of this work differ significantly from the methods in [55], we consider the latter work as a baseline to focus our efforts.

2 Problem Formulation

In this section, we provide relevant details of the problem formulation used by the plasma applications considered in this work. We begin with a discussion of the Vlasov-Maxwell system, which is the most general model used in this work, in section 2.1. Then, once we have introduced the model, we discuss the treatment of the fields in section 2.2, which expresses Maxwell’s equations in terms of potentials. In this work, the fields are cast as wave equations through the Lorenz gauge condition. The generalized momentum formulation used for the particles is presented in section 2.3. We then conclude the section with a brief summary to emphasize the key aspects of the proposed formulation.

2.1 Vlasov-Maxwell System

In this work, we develop numerical algorithms for plasmas described by the Vlasov-Maxwell (VM) system, which in SI units, reads as

$$\partial_t f_s + \mathbf{v} \cdot \nabla_{\mathbf{x}} f_s + \frac{q_s}{m_s} (\mathbf{E} + \mathbf{v} \times \mathbf{B}) \cdot \nabla_{\mathbf{v}} f_s = 0, \quad (1)$$

$$\nabla \times \mathbf{E} = -\partial_t \mathbf{B}, \quad (2)$$

$$\nabla \times \mathbf{B} = \mu_0 (\mathbf{J} + \epsilon_0 \partial_t \mathbf{E}), \quad (3)$$

$$\nabla \cdot \mathbf{E} = \frac{\rho}{\epsilon_0}, \quad (4)$$

$$\nabla \cdot \mathbf{B} = 0. \quad (5)$$

The first equation (1) is the Vlasov equation which describes the evolution of a probability distribution function $f_s(\mathbf{x}, \mathbf{v}, t)$ for particles of species s in phase space which have mass m_s and charge q_s . More specifically, it describes the probability of finding a particle of species s at the position \mathbf{x} , with a velocity \mathbf{v} , at any given time t . Since the position and velocity data are vectors with 3 components, the distribution function is a scalar function of 6 dimensions plus time. While the equation itself has fairly simple structure, the primary challenge in numerically solving this equation is its high dimensionality. This growth in the dimensionality has posed tremendous difficulties for grid-based discretization methods, where one often needs to use many grid points to resolve scales in the problem. This difficulty is compounded by the fact that many plasmas of interest contain multiple species. Despite the lack of a collision operator on the right-hand side of (1), collisions do exist in a certain mean-field sense, through the electric and magnetic fields which appear as coefficients of the velocity gradient.

Equations (2) - (5) are Maxwell’s equations, which describe the evolution of the background electric and magnetic fields. Since the plasma is a collection of moving charges, any changes in the distribution function for each species will be reflected in the charge density $\rho(\mathbf{x}, t)$, as well as the current density $\mathbf{J}(\mathbf{x}, t)$, which, respectively, are the source terms for Gauss’ law (4) and Ampère’s law (3). For N_s species, the total charge

density and current density are defined by summing over the species

$$\rho(\mathbf{x}, t) = \sum_{s=1}^{N_s} \rho_s(\mathbf{x}, t), \quad \mathbf{J}(\mathbf{x}, t) = \sum_{s=1}^{N_s} \mathbf{J}_s(\mathbf{x}, t), \quad (6)$$

where the species charge and current densities are defined through moments of the distribution function f_s :

$$\rho_s(\mathbf{x}, t) = q_s \int_{\Omega_v} f_s(\mathbf{x}, \mathbf{v}, t) d\mathbf{v}, \quad \mathbf{J}_s(\mathbf{x}, t) = q_s \int_{\Omega_v} \mathbf{v} f_s(\mathbf{x}, \mathbf{v}, t) d\mathbf{v}. \quad (7)$$

Here, the integrals are taken over the velocity components of phase space, which we have denoted by Ω_v . The remaining parameters ϵ_0 and μ_0 describe the permittivity and permeability of the media in which the fields propagate, which we take to be free-space. In free-space, Maxwell's equations move at the speed of light c , and we have the useful relation $c^2 = 1/(\mu_0\epsilon_0)$. The last two equations (4) and (5) are constraints placed on the fields to maintain charge conservation and prevent the appearance of so-called "magnetic monopoles". It is imperative that numerical schemes for Maxwell's equations satisfy these conditions. This requirement is one of the reasons we adopt a gauge formulation for Maxwell's equations, which is presented in the next section.

2.2 Maxwell's Equations with the Lorenz Gauge

Under the Lorenz gauge, Maxwell's equations transform to a system of decoupled wave equations of the form

$$\frac{1}{c^2} \frac{\partial^2 \psi}{\partial t^2} - \Delta \psi = \frac{1}{\epsilon_0} \rho, \quad (8)$$

$$\frac{1}{c^2} \frac{\partial^2 \mathbf{A}}{\partial t^2} - \Delta \mathbf{A} = \mu_0 \mathbf{J}, \quad (9)$$

$$\nabla \cdot \mathbf{A} + \frac{1}{c^2} \frac{\partial \psi}{\partial t} = 0, \quad (10)$$

where c is the speed of light, ϵ_0 and μ_0 represent, respectively, the permittivity and permeability of free-space. Further, we have used ψ to denote the scalar potential and \mathbf{A} is the vector potential. In fact, under any choice of gauge condition, given ψ and \mathbf{A} , one can recover \mathbf{E} and \mathbf{B} via the relations

$$\mathbf{E} = -\nabla \psi - \frac{\partial \mathbf{A}}{\partial t}, \quad \mathbf{B} = \nabla \times \mathbf{A}, \quad (11)$$

where " \times " denotes the vector cross product. The structure of equations (8) and (9) is appealing because the system, modulo the gauge condition (10), is essentially a system of four "decoupled" scalar wave equations. Since this system is over-determined, the coupling manifests itself through the gauge condition which should be thought of as a constraint. Moreover, Maxwell's equations (2) - (5) are equivalent to (8) and (9) as long as the Lorenz gauge condition (10) is satisfied by ψ and \mathbf{A} . This formulation is appealing for several reasons. This form of the system is purely hyperbolic, so it evolves in a local sense. Computationally, this means that a localized method can be used to evolve the system, which will likely be more efficient for parallel computers. Another attractive feature is that many of the methods developed for scalar wave equations, e.g., [52] and [47] can be applied to the system in a straightforward manner.

2.3 Generalized Momentum Formulation for the Particles

A particle formulation of the Vlasov equation (1) can be developed by writing the species distribution function f_s as a collection of Dirac delta distributions over phase space:

$$f_s(\mathbf{x}, \mathbf{v}, t) = \sum_{p=1}^{N_{ps}} \delta(\mathbf{x} - \mathbf{x}_p(t)) \delta(\mathbf{v} - \mathbf{v}_p(t)). \quad (12)$$

Here, N_{p_s} symbolizes the number of particles of species s . Notice that we also have the relation

$$\int_{\Omega_x} \int_{\Omega_v} f_s(\mathbf{x}, \mathbf{v}, t) d\mathbf{v} d\mathbf{x} = N_{p_s},$$

which holds at any time t . Furthermore, f_s can be converted into a proper distribution by including a normalization factor of $1/N_{p_s}$. By combining the ansatz (12) with the definitions (6) and (7), we obtain the following definitions of charge density and current density for a collection of N_p simulation particles:

$$\rho(\mathbf{x}, t) = \sum_{p=1}^{N_p} q_p \delta(\mathbf{x} - \mathbf{x}_p(t)), \quad (13)$$

$$\mathbf{J}(\mathbf{x}, t) = \sum_{p=1}^{N_p} q_p \mathbf{v}_p(t) \delta(\mathbf{x} - \mathbf{x}_p(t)). \quad (14)$$

In the above equations, q_p , \mathbf{x}_p , and \mathbf{v}_p denote the charge, position, and velocity, respectively, of a particle whose label is p . In defining things this way, we have dropped the reference to the species altogether, since each particle can be thought of as its own entity. These particles move along characteristics of the equation (1), which are given by the system of ordinary differential equations

$$\begin{aligned} \dot{\mathbf{x}}_i &= \mathbf{v}_i \\ \dot{\mathbf{v}}_i &= \frac{1}{m_i} \mathbf{F}(\mathbf{x}_i), \end{aligned}$$

with m_i being the mass of particle i . The vector field \mathbf{F} is the Lorentz force that acts on particles and is defined by

$$\mathbf{F} = q(\mathbf{E} + \mathbf{v} \times \mathbf{B}), \quad (15)$$

where we have removed the subscript that refers to a specific particle for simplicity. Next, we write the fields in terms of their potentials. Using (11), we can obtain the equivalent expression

$$\mathbf{F} = q\left(-\nabla\psi - \frac{\partial \mathbf{A}}{\partial t} + \mathbf{v} \times (\nabla \times \mathbf{A})\right).$$

This expression can be simplified with the aid of the vector identity

$$\nabla(\mathbf{a} \cdot \mathbf{b}) = \mathbf{a} \times \nabla \times \mathbf{b} + \mathbf{b} \times \nabla \times \mathbf{a} + (\mathbf{a} \cdot \nabla) \mathbf{b} + (\mathbf{b} \cdot \nabla) \mathbf{a}. \quad (16)$$

Using $\mathbf{a} \equiv \mathbf{A}$ and $\mathbf{b} \equiv \mathbf{v}$, along with the fact that the the velocity \mathbf{v} does not depend on \mathbf{x} , we obtain the relation

$$\mathbf{v} \times (\nabla \times \mathbf{A}) = \nabla(\mathbf{A} \cdot \mathbf{v}) - (\mathbf{v} \cdot \nabla) \mathbf{A}.$$

Inserting this expression into the force yields

$$\mathbf{F} = q\left(-\nabla\psi - \frac{\partial \mathbf{A}}{\partial t} + \nabla(\mathbf{A} \cdot \mathbf{v}) - (\mathbf{v} \cdot \nabla) \mathbf{A}\right).$$

Then we can use the definition of the total (convective) derivative to write

$$\frac{d\mathbf{A}}{dt} = \frac{\partial \mathbf{A}}{\partial t} + (\mathbf{v} \cdot \nabla) \mathbf{A},$$

which means the force is equivalent to

$$\mathbf{F} = q\left(-\nabla\psi - \frac{d\mathbf{A}}{dt} + \nabla(\mathbf{A} \cdot \mathbf{v})\right).$$

If we let \mathbf{p} denote the classical momentum $\mathbf{p} = m\mathbf{v}$, so that $\frac{d\mathbf{p}}{dt} = \mathbf{F}$, then we can move the time derivatives to the left side of the equation, which gives

$$\frac{d}{dt}(\mathbf{p} + q\mathbf{A}) = q\left(-\nabla\psi + \nabla(\mathbf{A} \cdot \mathbf{v})\right).$$

The expression on the left contains the canonical (generalized) momentum

$$\mathbf{P} := \mathbf{p} + q\mathbf{A}, \quad (17)$$

and the right side can be expressed as $-\nabla U$, if we let $U = q(\psi - \mathbf{A} \cdot \mathbf{v})$. Therefore, we obtain the canonical momentum equation

$$\frac{d\mathbf{P}}{dt} = q \left(-\nabla\psi + \nabla(\mathbf{A} \cdot \mathbf{v}) \right).$$

This is the penultimate form of the equation we seek. Instead, we want the derivatives to appear on the vector potential \mathbf{A} rather than $\mathbf{A} \cdot \mathbf{v}$. For this, we can use an equivalent form of the identity (16), namely

$$\nabla(\mathbf{a} \cdot \mathbf{b}) = (\nabla\mathbf{b}) \cdot \mathbf{a} + (\nabla\mathbf{a}) \cdot \mathbf{b}.$$

Again, we select $a \equiv \mathbf{A}$ and $b \equiv \mathbf{v}$, which shows that

$$\nabla(\mathbf{A} \cdot \mathbf{v}) = (\nabla\mathbf{v}) \cdot \mathbf{A} + (\nabla\mathbf{A}) \cdot \mathbf{v}.$$

Equation (17) provides the connection between the linear momentum $\mathbf{p} = m\mathbf{v}$ and the canonical momentum \mathbf{P} , so that the velocity is given by

$$\mathbf{v} \equiv \frac{1}{m}(\mathbf{P} - q\mathbf{A}). \quad (18)$$

Since \mathbf{v} is a function only of time

$$(\nabla\mathbf{v}) \cdot \mathbf{A} = 0.$$

Combining this with the other term yields an expanded form for the canonical momentum update:

$$\frac{d\mathbf{P}}{dt} = q \left(-\nabla\psi + \frac{1}{m}(\nabla\mathbf{A}) \cdot (\mathbf{P} - q\mathbf{A}) \right). \quad (19)$$

Note that since \mathbf{A} is a vector, taking the gradient increases its rank by 1, which means that $\nabla\mathbf{A}$ is a dyad. In component form, we can write $\nabla(\mathbf{a} \cdot \mathbf{b})$ as

$$\partial_i(a_j b_j) = (\partial_i a_j) b_j + (\partial_i b_j) a_j = \frac{\partial a^{(j)}}{\partial x_i} b_j + \frac{\partial b^{(j)}}{\partial x_i} a_j, \quad (20)$$

where the summation convention over repeated indices has been used. For our case, the vector \mathbf{b} in the above calculation does not depend on space. Therefore, one only requires computing the entries of the dyad

$$\frac{\partial A^{(j)}}{\partial x_i} \equiv J_{\mathbf{A}}^T \quad (21)$$

where $J_{\mathbf{A}}$ is the Jacobian matrix associated with \mathbf{A} . Another way to see that the (20) and (21) are the correct expressions for (19) is to use the fact that $\mathbf{A} \cdot \mathbf{v}$ is a scalar, then apply the usual gradient operator for scalar functions. In other words,

$$\begin{aligned} \nabla(\mathbf{A} \cdot \mathbf{v}) &= \nabla \left(A^{(1)}v^{(1)} + A^{(2)}v^{(2)} + A^{(3)}v^{(3)} \right), \\ &= \begin{bmatrix} \partial_x (A^{(1)}v^{(1)} + A^{(2)}v^{(2)} + A^{(3)}v^{(3)}) \\ \partial_y (A^{(1)}v^{(1)} + A^{(2)}v^{(2)} + A^{(3)}v^{(3)}) \\ \partial_z (A^{(1)}v^{(1)} + A^{(2)}v^{(2)} + A^{(3)}v^{(3)}) \end{bmatrix}. \end{aligned}$$

The result follows by distributing the derivatives in each row, using the fact that the components of the velocity do not depend on space, followed by use of the definition (18).

To obtain the position equation, we note that $\frac{d\mathbf{x}}{dt} = \mathbf{v}$ and that the classical momentum is given by $\mathbf{p} = m\mathbf{v}$. This implies that

$$\mathbf{P} = m \frac{d\mathbf{x}}{dt} + q\mathbf{A},$$

which can be arranged to obtain

$$\frac{d\mathbf{x}}{dt} = \frac{1}{m} (\mathbf{P} - q\mathbf{A}). \quad (22)$$

Since the transformed equations of motion given by (19) and (22) will be identical in structure among the particles (differing only by labels for the particles) this results in the system

$$\frac{d\mathbf{x}_i}{dt} = \frac{1}{m_i} (\mathbf{P}_i - q_i\mathbf{A}), \quad (23)$$

$$\frac{d\mathbf{P}_i}{dt} = q_i \left(-\nabla\psi + \frac{1}{m_i} (\nabla\mathbf{A}) \cdot (\mathbf{P}_i - q_i\mathbf{A}) \right). \quad (24)$$

The complete formulation for the VM system combines the particle equations (23) - (24) with the Lorenz gauge formulation of the fields given by equations (8)-(10). Notice that this formulation avoids the time derivative required to convert the potentials to the usual \mathbf{E} and \mathbf{B} fields. Instead, particles are updated from the potentials and their spatial derivatives; however, this new system is non-separable, as momentum appears in both equations, and necessitates special time integration methods that will be discussed in section 4. The details concerning the non-dimensionalization used in the numerical investigation of these models can be found in the Appendix A.

2.4 Summary

In this section, we introduced the VM system, which is the mathematical model that will be the focus of this work. Maxwell's equations for the fields were expressed in terms of the Lorenz gauge condition resulting in wave equations that are amenable to the class of unconditionally stable wave solvers developed in our earlier work. To eliminate the time derivatives of the vector potential, we adopt a formulation of the particles that uses a generalized Hamiltonian. This allows us to retain the full time accuracy of the fields at the expense of a more complex, non-separable system of equations for the particles. In the next section, we introduce the wave solvers and propose new methods for evaluating spatial derivatives of the fields that are required in the equations for the particles. A key feature of the proposed methods for derivatives is that they retain the convergence rates of the base solver. Additionally, these methods are constructed so that they naturally inherit the stability properties of the base method and can be applied to problems with geometry. While this work is largely focused on aspects concerning the formulation, preserving the geometric flexibility of the methods is essential for the applications we plan to explore in future work.

3 Numerical Methods for the Field Equations

In this section, we describe the algorithms used for wave propagation, which are required in the formulations of Maxwell's equations presented in the previous section. We begin with a general discussion of Green's function methods and integral equations in section 3.1. These techniques are the foundation of the approaches considered in this work, which incorporate dimensional-splitting for multi-dimensional problems. The solver considered in this work is first-order accurate (in time), and is presented in section 3.2.1 in its semi-discrete form. A short discussion is presented in section 3.2.2 that addresses the stability of the proposed method in its semi-discrete form. In section 3.2.3 we prove that this first-order semi-discrete scheme, when applied to the Lorenz gauge formulation of the VM system, satisfies a semi-discrete form of the Lorenz gauge condition. Using a dimensional splitting technique, which is presented at the end of the same section, we formulate the solution in terms of one-dimensional operators that can be inverted using the methods discussed in section 3.3. We then discuss the application of boundary conditions in section 3.4, which also includes caveats for multi-dimensional problems. Additionally, we show how to construct derivatives of the fields analytically, which retains the convergence rate of the original method. This section also discusses outflow boundary conditions, which have presented challenges for this class of methods. Following [52], we briefly discuss the extensions of these methods to higher-order accuracy in time and taking care to address complications for boundary conditions in these methods. We conclude with a brief summary in section 3.5.

3.1 Integral Equation Methods and Green's Functions

Integral equation methods or, more generally, Green's function methods, are a powerful class of techniques used in the solution of boundary value problems that occur in a range of applications, including acoustics, fluid dynamics, and electromagnetism [56, 57, 58, 59, 60, 61, 62, 63]. Such methods allow one to write an explicit solution of an elliptic PDE in terms of a fundamental solution or Green's function. While explicit, this solution can be difficult or impossible to evaluate, so numerical quadrature is used to evaluate these terms. Layer potentials can then be introduced in the form of surface integrals to adjust the solution to satisfy the prescribed boundary data [64]. This framework allows one to solve problems in complicated domains without resorting to the use of a mesh. We illustrate these features of the method with an example.

Suppose that we are solving the following modified Helmholtz equation

$$\left(\mathcal{I} - \frac{1}{\alpha^2}\Delta\right)u(\mathbf{x}) = S(\mathbf{x}), \quad \mathbf{x} \in \Omega, \quad (25)$$

where $\Omega \subset \mathbb{R}^n$ and \mathcal{I} is the identity operator, Δ is the Laplacian operator in \mathbb{R}^n , S is a source term, and $\alpha \in \mathbb{R}$ is a parameter. While this method can be broadly applied to other elliptic PDEs, equation (25) is of interest to us because it can be obtained from the time discretization of a parabolic or hyperbolic PDE. In this case, the source function would include additional time levels of u and the parameter $\alpha = \alpha(\Delta t)$ would be connected to the time discretization of this problem. We shall not prescribe boundary conditions for this problem, and instead consider the most general solution.

To apply a Green's function method to equation (25), one first needs to identify a function $G(\mathbf{x}, \mathbf{y})$ that solves the equation

$$\left(\mathcal{I} - \frac{1}{\alpha^2}\Delta\right)G(\mathbf{x}, \mathbf{y}) = \delta(\mathbf{x} - \mathbf{y}), \quad \mathbf{x}, \mathbf{y} \in \mathbb{R}^n \quad (26)$$

over free-space, with $\delta(\mathbf{x} - \mathbf{y})$ being the Dirac delta distribution. There are many ways to approach solving this equation. For example, it is common to take advantage of radial symmetry so that the problem reduces to a single variable, which can be solved using a Fourier transform. Green's functions have been tabulated for many different operators, including the modified Helmholtz operator [65]. Therefore, we shall not elaborate on this further and assume that the fundamental solution $G(\mathbf{x}, \mathbf{y})$ is known for our problem.

We now show the connection between fundamental solution $G(\mathbf{x}, \mathbf{y})$, which is defined on free-space and solves (26), and the original problem (25). First, let u be a solution of the problem (25). Multiplying the equation (26) by u , integrating over Ω , and applying the divergence theorem (or integration by parts in 1-D) leads to the integral identity

$$u(\mathbf{x}) = \int_{\Omega} G(\mathbf{x}, \mathbf{y})S(\mathbf{y})dV_{\mathbf{y}} + \frac{1}{\alpha^2} \int_{\partial\Omega} \left(G(\mathbf{x}, \mathbf{y})\frac{\partial u}{\partial \mathbf{n}} - u(\mathbf{y})\frac{\partial G}{\partial \mathbf{n}}\right) dS_{\mathbf{y}}. \quad (27)$$

Note that the above identity utilizes the assumption that the function u solves the PDE (25). Since the volume integral term does not enforce boundary conditions, the surface integral contributions involving u are replaced with an ansatz of the form

$$u(\mathbf{x}) = \int_{\Omega} G(\mathbf{x}, \mathbf{y})S(\mathbf{y})dV_{\mathbf{y}} + \int_{\partial\Omega} \left(\sigma(\mathbf{y})G(\mathbf{x}, \mathbf{y}) + \gamma(\mathbf{y})\frac{\partial G}{\partial \mathbf{n}}\right) dS_{\mathbf{y}}, \quad (28)$$

where $\sigma(\mathbf{y})$ is the single-layer potential and $\gamma(\mathbf{y})$ is the double-layer potential, which must now be determined to enforce the boundary conditions. The choice of names is reflected by the behavior of the Green's function associated with each of the terms. The Green's function itself is continuous, but its derivative will have a "jump". Based on the boundary conditions, one selects either a single or double layer form as the ansatz for the solution. The single layer form is used in the Neumann problem, while the double layer form is chosen for the Dirichlet problem.

Numerically evaluating the solution (28), first requires a discretization of the integrals using quadrature. The evaluation then proceeds by computing the volume integral term, which is the particular solution to the

problem (25). Using the particular solution, one obtains the homogeneous solution that corresponds to the boundary integral term, which is subject to modified boundary data that accounts for the particular solution's contributions along the boundary. This step for the homogeneous solution requires the identification of $\sigma(\mathbf{y})$ or $\gamma(\mathbf{y})$ at the quadrature points taken along the domain boundary, which results in a dense linear system. In contrast to other classes of solvers, e.g, finite-elements or finite-difference schemes, these linear systems are usually well-conditioned, so the application of an iterative solver, such as the GMRES method [40] yields rapid convergence. For efficiency, the fast-multipole method (FMM) [66] can also be used to reduce the evaluation time required in the GMRES iterations [62].

The algorithms presented in the subsequent sections are essentially a one-dimensional analogue of these methods. Rather than invert the multi-dimensional operator corresponding to (28), the methods presented here, instead, factor the Laplacian and invert one-dimensional operators, dimension-by-dimension, using the one-dimensional form of (28). We will see, later, the resulting methods solve for something that looks like a layer potential, with the key difference being that the linear system is now only a small, 2×2 matrix, which can be inverted by hand, rather than with an iterative method. Similarly, the particular solution along a given line segment can be rapidly computed with a lightweight, recursive, fast summation method, rather than a more complicated method, such as the FMM. Moreover, these methods retain the geometric flexibility since the domain can be represented using one-dimensional line segments with termination points specified by the geometry.

3.2 Description of the Wave Solver

Here we provide a description of the wave solver used to evolve the potentials in the Lorenz gauge formulation of Maxwell's equations. We first show how to derive the semi-discrete equation associated with the method, which takes the form of the modified Helmholtz equation (25). Unlike the high order methods from our previous work, here we choose to discretize the time derivatives of the wave equation using a first-order backwards difference formula (BDF). We then provide a short section on the stability analysis of the proposed semi-discrete method. Following the introduction of the scheme, we establish a time consistency property that applies when the proposed discretization is used for the potentials in the Lorenz gauge formulation. Then, we briefly discuss the splitting technique that is used for multi-dimensional problems.

3.2.1 The Semi-discrete BDF Scheme

To derive the first-order (time) BDF wave solver, we start with the equation

$$\frac{1}{c^2} \frac{\partial^2 u}{\partial t^2} - \Delta u = S(\mathbf{x}, t), \quad (29)$$

where c is the wave speed and S is a source function. Then, using the notation $u(\mathbf{x}, t^n) = u^n$, we can apply a second-order accurate backwards finite-difference stencil for the second derivative

$$\left. \frac{\partial^2 u}{\partial t^2} \right|_{t=t^{n+1}} = \frac{u^{n+1} - 2u^n + u^{n-1}}{\Delta t^2} + \mathcal{O}(\Delta t),$$

where $\Delta t = t^k - t^{k-1}$, for any k , is the grid spacing in time. Evaluating the remaining terms in equation (29) at time level t^{n+1} , and inserting the above difference approximation, we obtain

$$\frac{1}{c^2 \Delta t^2} (u^{n+1} - 2u^n + u^{n-1}) - \Delta u^{n+1} = S^{n+1}(\mathbf{x}) + \mathcal{O}\left(\frac{1}{\alpha}\right),$$

which can be rearranged to obtain the semi-discrete equation

$$\left(\mathcal{I} - \frac{1}{\alpha^2} \Delta \right) u^{n+1} = (2u^n - u^{n-1}) + \frac{1}{\alpha^2} S^{n+1}(\mathbf{x}) + \mathcal{O}\left(\frac{1}{\alpha^3}\right), \quad (30)$$

where we have introduced the parameter $\alpha = 1/(c\Delta t)$. We note that the source term is treated implicitly in this method, which creates additional complications if the source function S depends on u . This necessitates some form of iteration, which increases the cost of the method.

3.2.2 Stability Analysis of the Semi-discrete BDF Scheme

We now analyze the stability of the first-order semi-discrete BDF scheme given by equation (30). Suppose that the solution $u(\mathbf{x})$ takes the form of the plane wave given by

$$u^n(\mathbf{x}) = \lambda^n e^{i\mathbf{k}\cdot\mathbf{x}}.$$

Substituting this ansatz into the semi-discrete scheme (30) and ignoring contributions due to sources, we obtain the polynomial equation

$$(1 + z^2) \lambda^2 - 2\lambda + 1 = 0.$$

In the above equation, we have defined the real number $z^2 = k^2/\alpha^2$ for simplicity. The roots of this polynomial are a pair of complex conjugates that can be written as

$$\lambda = \frac{1}{1 + z^2} \left(1 \pm i\sqrt{z^2} \right),$$

which satisfy the condition $|\lambda| \leq 1$ for any Δt . This shows that the amplitude of the plane wave does not grow in time, so the scheme is stable.

3.2.3 Time-consistency of the Semi-discrete Lorenz Gauge Formulation

In this section we prove a theorem that establishes a certain time consistency property of the Lorenz gauge formulation of Maxwell's equations (8)-(10) when the semi-discrete BDF discretization (30) is applied to the potentials. By time-consistent, we mean that the semi-discrete system for the potentials induces both a gauge condition and continuity equation at the semi-discrete level that are preserved under this discretization. In the treatment of the semi-discrete equations, we shall ignore effects of dimensional splittings and instead consider the more general inverse induced by the boundary integral solution (28).

We first introduce the semi-discrete system for the Lorenz gauge formulation of Maxwell's equations given by (8)-(10). Appealing to equation (30), we obtain the semi-discrete system

$$\mathcal{L}\psi^{n+1} = 2\psi^n - \psi^{n-1} + \frac{1}{\alpha^2 \epsilon_0} \rho^{n+1}, \quad (31)$$

$$\mathcal{L}\mathbf{A}^{n+1} = 2\mathbf{A}^n - \mathbf{A}^{n-1} + \frac{\mu_0}{\alpha^2} \mathbf{J}^{n+1}, \quad (32)$$

$$\frac{\psi^{n+1} - \psi^n}{c^2 \Delta t} + \nabla \cdot \mathbf{A}^{n+1} = 0, \quad (33)$$

where we have used the usual operator notation

$$\mathcal{L} := \mathcal{I} - \frac{1}{\alpha^2} \Delta, \quad \alpha := \frac{1}{c \Delta t}. \quad (34)$$

Next, we show that this semi-discrete system is time-consistent in the sense of the semi-discrete Lorenz gauge. To simplify the presentation, we prove a lemma that connects the discrete gauge condition (33) to the semi-discrete equations for the potentials given by equations (31) and (32).

Lemma 3.1. *The semi-discrete Lorenz gauge condition (33) satisfies*

$$\epsilon^{n+1} = \mathcal{L}^{-1} \left(2\epsilon^n - \epsilon^{n-1} + \frac{\mu_0}{\alpha^2} \left(\frac{\rho^{n+1} - \rho^n}{\Delta t} + \nabla \cdot \mathbf{J}^{n+1} \right) \right). \quad (35)$$

where we have defined the semi-discrete residual

$$\epsilon^n = \frac{\psi^n - \psi^{n-1}}{c^2 \Delta t} + \nabla \cdot \mathbf{A}^n. \quad (36)$$

Proof. First, we note that the modified Helmholtz operator \mathcal{L} can be formally “inverted” with the boundary integral solution given by equation (28). From this, we can calculate the terms involving the potentials in the residual (36). Proceeding, the equation for the scalar potential is found to be

$$\psi^{n+1} = \mathcal{L}^{-1} \left(2\psi^n - \psi^{n-1} + \frac{1}{\alpha^2 \epsilon_0} \rho^{n+1} \right), \quad (37)$$

which can be evaluated at time level n to yield

$$\psi^n = \mathcal{L}^{-1} \left(2\psi^{n-1} - \psi^{n-2} + \frac{1}{\alpha^2 \epsilon_0} \rho^n \right). \quad (38)$$

Next, we take the divergence of \mathbf{A} in equation (32) and find that

$$\mathcal{L}(\nabla \cdot \mathbf{A}^{n+1}) = 2\nabla \cdot \mathbf{A}^n - \nabla \cdot \mathbf{A}^{n-1} + \frac{\mu_0}{\alpha^2} \nabla \cdot \mathbf{J}^{n+1}.$$

Formally inverting the operator \mathcal{L} , we obtain the relation

$$\nabla \cdot \mathbf{A}^{n+1} = \mathcal{L}^{-1} \left(2\nabla \cdot \mathbf{A}^n - \nabla \cdot \mathbf{A}^{n-1} + \frac{\mu_0}{\alpha^2} \nabla \cdot \mathbf{J}^{n+1} \right). \quad (39)$$

With the aid of equations (37), (39), and (38) along with the linearity of the operator \mathcal{L} , a direct calculation reveals that the residual (36) at time level $n+1$ is given by

$$\frac{\psi^{n+1} - \psi^n}{c^2 \Delta t} + \nabla \cdot \mathbf{A}^{n+1} = \mathcal{L}^{-1} \left(\frac{2\psi^n - 3\psi^{n-1} + \psi^{n-2}}{c^2 \Delta t} + 2\nabla \cdot \mathbf{A}^n - \nabla \cdot \mathbf{A}^{n-1} + \frac{\mu_0}{\alpha^2} \left(\frac{\rho^{n+1} - \rho^n}{\Delta t} + \nabla \cdot \mathbf{J}^{n+1} \right) \right).$$

Note that we have used the relation $c^2 = 1/(\mu_0 \epsilon_0)$. From these calculations, we can see that the corresponding semi-discrete continuity equation

$$\frac{\rho^{n+1} - \rho^n}{\Delta t} + \nabla \cdot \mathbf{J}^{n+1} = 0, \quad (40)$$

acts as a source for the residual (36). The remaining terms in the operand for the inverse can be also be expressed directly in terms of this semi-discrete gauge, since

$$\begin{aligned} \frac{2\psi^n - 3\psi^{n-1} + \psi^{n-2}}{c^2 \Delta t} + 2\nabla \cdot \mathbf{A}^n - \nabla \cdot \mathbf{A}^{n-1} &= 2 \left(\frac{\psi^n - \psi^{n-1}}{c^2 \Delta t} + \nabla \cdot \mathbf{A}^n \right) - \left(\frac{\psi^{n-1} - \psi^{n-2}}{c^2 \Delta t} + \nabla \cdot \mathbf{A}^{n-1} \right), \\ &\equiv 2\epsilon^n - \epsilon^{n-1}. \end{aligned}$$

This completes the proof. \square

With the aid of Lemma 3.1, we are now prepared to prove the following theorem that establishes the time-consistency of the semi-discrete system.

Theorem 3.1. *The semi-discrete Lorenz gauge formulation of Maxwell’s equations (31)-(33) is time-consistent in the sense that the semi-discrete Lorenz gauge condition (33) is satisfied at any discrete time t^{n+1} if and only if the corresponding semi-discrete continuity equation (40) is also satisfied.*

Proof. We use a simple inductive argument to prove both directions. In the case of the forward direction, we assume that the semi-discrete gauge condition is satisfied at any discrete time t^n such that $\epsilon^n \equiv 0$. Combining this with equation (35) established by Lemma 3.1, it follows that the next time level satisfies

$$0 = \mathcal{L}^{-1} \left(\frac{\mu_0}{\alpha^2} \left(\frac{\rho^1 - \rho^0}{\Delta t} + \nabla \cdot \mathbf{J}^1 \right) \right).$$

Applying the operator \mathcal{L} to both sides leads to

$$\frac{\rho^1 - \rho^0}{\Delta t} + \nabla \cdot \mathbf{J}^1 = 0.$$

This argument can be iterated n times to show that

$$\frac{\rho^{n+1} - \rho^n}{\Delta t} + \nabla \cdot \mathbf{J}^{n+1} = 0,$$

holds at any discrete time t^n , as well, which establishes the forward direction.

A similar argument can be used for the converse. Here, we show that if the semi-discrete continuity equation (40) is satisfied for any time level n , then the residual for the discrete gauge condition also satisfies $\epsilon^{n+1} \equiv 0$. First, we assume that the initial data and starting values satisfy $\epsilon^{-1} \equiv \epsilon^0 \equiv 0$. Appealing to equation (35) with this initial data, it is clear that after a single time step, the residual in the gauge condition satisfies

$$\epsilon^1 = \mathcal{L}^{-1} \left(2\epsilon^0 - \epsilon^{-1} + \frac{\mu_0}{\alpha^2} \left(\frac{\rho^1 - \rho^0}{\Delta t} + \nabla \cdot \mathbf{J}^1 \right) \right) \equiv \mathcal{L}^{-1}(0).$$

This argument can also be iterated n more times to obtain the result, which finishes the proof. \square

Theorem 3.1 motivates, to a large extent, the adoption of a low-order time discretization for the fields. An important consequence of this time-consistency is that it eliminates the need for potentially expensive cleaning methods to ensure that the gauge condition is properly satisfied. While we have neglected the error introduced by dimensional splittings, our results for the numerical experiments presented in section 5 suggest that this effects of this approximation can be neglected. We find this to be the true even in the case of more challenging beam problems, which are known to be quite sensitive to subtle violations in the gauge condition.

3.2.4 Splitting Method Used for Multi-dimensional Problems

The semi-discrete equation (30) is a modified Helmholtz equations of the form (25). Instead of appealing to (28), which formally inverts the multi-dimensional modified Helmholtz operator, we apply a factorization into a product of one dimensional operators. For example, in two-spatial dimensions, the factorization is given by

$$\begin{aligned} \mathcal{I} - \frac{1}{\alpha^2} \Delta &= \left(\mathcal{I} - \frac{1}{\alpha^2} \partial_{xx} \right) \left(\mathcal{I} - \frac{1}{\alpha^2} \partial_{yy} \right) + \frac{1}{\alpha^4} \partial_{xx} \partial_{yy}, \\ &\equiv \mathcal{L}_x \mathcal{L}_y + \frac{1}{\alpha^4} \partial_{xx} \partial_{yy}, \end{aligned}$$

where \mathcal{L}_x and \mathcal{L}_y are one-dimensional operators and the last term represents the splitting error associated with the factorization step. Note that the coefficient of the splitting error is $1/\alpha^4 = \mathcal{O}(\Delta t^4)$, which can be ignored for first-order accuracy. Therefore, the semi-discrete equation (30) in two-dimensions can be written more compactly (dropping error terms) as

$$\mathcal{L}_x \mathcal{L}_y u^{n+1}(\mathbf{x}) = 2u^n(\mathbf{x}) - u^{n-1}(\mathbf{x}) + \frac{1}{\alpha^2} S^{n+1}(\mathbf{x}), \quad \alpha := \frac{1}{c\Delta t}. \quad (41)$$

Considerable effort has been made to address issues associated with the splitting error. For example, in [67], iterative techniques were developed to remove the splitting error in multi-dimensional applications concerning phase-field models with parabolic equations. Successive convolution methods for the wave equation, introduced in the paper [52], achieve higher-order accuracy in time through more elaborate operator expansions that perform additional sweeps to remove this error. Such approaches are not considered in this paper, as we are primarily concerned with the formulation of new particle methods. Methods with higher-order time accuracy that address the splitting error will be explored in later work. Next, we discuss the procedure used to invert the one-dimensional operators used in the factorization.

3.3 Inverting One-dimensional Operators

The choice of factoring the multi-dimensional modified Helmholtz operator means we now have to solve a sequence of one-dimensional boundary value problems (BVPs) of the form

$$\left(\mathcal{I} - \frac{1}{\alpha^2} \partial_{xx}\right) w(x) = f(x), \quad x \in [a, b], \quad (42)$$

where $[a, b]$ is a one-dimensional line and f is a new source term that can be used to represent a time history or an intermediate variable constructed from the inversion of an operator along another direction. We also point out that the parameter α depends on the choice of the semi-discrete scheme employed to solve the problem. For the BDF scheme presented in this paper, we take $\alpha = 1/(c\Delta t)$. We will show the process by which one obtains the general solution to the problem (42), deferring the application of boundary conditions to section 3.4.

3.3.1 Integral Solution

Since the BVP (42) is linear, its general solution can be expressed using the one-dimensional analogue of equation (27):

$$w(x) = \int_a^b G(x, y) f(y) dy + \frac{1}{\alpha^2} [G(x, y) \partial_y u(y) - u(y) \partial_y G(x, y)] \Big|_{y=a}^{y=b}, \quad (43)$$

where the free-space Green's function in one-dimension is

$$G(x, y) = \frac{\alpha}{2} e^{-\alpha|x-y|}. \quad (44)$$

In order to use the relation (43), we need to evaluate the derivatives of the Green's function near the boundary. We note that

$$\partial_y G(x, y) = \begin{cases} \frac{\alpha}{2} e^{-\alpha(x-y)}, & x \geq y, \\ -\frac{\alpha}{2} e^{-\alpha(y-x)}, & x < y. \end{cases}$$

Taking limits, we find that

$$\begin{aligned} \lim_{y \rightarrow a} \partial_y G(x, y) &= \frac{\alpha}{2} e^{-\alpha(x-a)}, \\ \lim_{y \rightarrow b} \partial_y G(x, y) &= -\frac{\alpha}{2} e^{-\alpha(b-x)}. \end{aligned}$$

Combining these limits with (43), we obtain the general solution

$$w(x) = \frac{\alpha}{2} \int_a^b e^{-\alpha|x-y|} f(y) dy + A e^{-\alpha(x-a)} + B e^{-\alpha(b-x)}, \quad (45)$$

where A and B are constants that are determined by boundary conditions. Comparing with (28), these terms serve the same purpose as the layer potentials. Further, we identify the general solution (45) as the inverse of the one-dimensional modified Helmholtz operator. In other words, we define \mathcal{L}_x^{-1} so that

$$w(x) = \mathcal{L}_x^{-1} [f](x), \quad (46)$$

$$\equiv \frac{\alpha}{2} \int_a^b e^{-\alpha|x-y|} f(y) dy + A e^{-\alpha(x-a)} + B e^{-\alpha(b-x)}, \quad (47)$$

$$\equiv \mathcal{I}_x[f](x) + A e^{-\alpha(x-a)} + B e^{-\alpha(b-x)}. \quad (48)$$

Section 3.4 will make repeated use of definitions (46)-(48) to illustrate the application of boundary conditions. The integral operator $\mathcal{I}_x[f](x)$ is evaluated as

$$\mathcal{I}_x[f](x) = \frac{1}{2} \left(\mathcal{I}_x^R[f](x) + \mathcal{I}_x^L[f](x) \right). \quad (49)$$

where the integrals

$$\mathcal{I}_x^R[f](x) \equiv \alpha \int_a^x e^{-\alpha(x-y)} f(y) dy, \quad (50)$$

$$\mathcal{I}_x^L[f](x) \equiv \alpha \int_x^b e^{-\alpha(y-x)} f(y) dy, \quad (51)$$

are computed with a recursive fast summation method. Details of this evaluation exist in numerous instances of previous work, e.g., [52, 53, 67, 68, 69]. For completeness, details of the method are included in the Appendices B.1 and B.2.

3.4 Applying Boundary Conditions

In this section, we discuss the application of boundary conditions for the proposed method, which is based on a first-order BDF time discretization of a second time derivative. Boundary conditions are presented from the perspective of one-dimensional problems and are applied in a dimension-by-dimension fashion in multi-dimensional problems.

To set the stage for the ensuing discussion, note that the semi-discrete update for the first-order BDF method, in one-spatial dimension, can be obtained by combining (45) with the semi-discrete equation (30). Defining the operand

$$R(x) = 2u^n(x) - u^{n-1}(x) + \frac{1}{\alpha^2} S^{n+1}(x),$$

we obtain the update

$$u^{n+1}(x) = \frac{\alpha}{2} \int_a^b e^{-\alpha|x-y|} R(y) dy + Ae^{-\alpha(x-a)} + Be^{-\alpha(b-x)}, \quad (52)$$

$$\equiv \mathcal{I}_x[R](x) + Ae^{-\alpha(x-a)} + Be^{-\alpha(b-x)}, \quad (53)$$

where we have used $\mathcal{I}_x[\cdot]$ to denote the term involving the convolution integral which is not to be confused with the identity operator. Applying different boundary conditions amounts to determining the values of A and B used in (53). In the description of boundary conditions for the method, we shall assume that the boundary conditions at the ends of the one-dimensional domain are the same. Using slight variations of the methods illustrated below, one can mix the boundary conditions at the ends of the line segments.

In order to enforce conditions on the derivatives of the solution, we will also need to compute a derivative of the update (52) (equivalently (53)). For this, we observe that the dependency for x appears only on analytical functions, i.e., the Green's function (kernel) and the exponential functions in the boundary terms. To differentiate (52) we start with the definition (49), which splits the integral at the point $y = x$ and makes the kernel easier to manipulate. Then, using the fundamental theorem of calculus, we can calculate derivatives of (50) and (51) to find that

$$\frac{d}{dx} (\mathcal{I}_x^R[f](x)) = \frac{d}{dx} \left(\alpha \int_a^x e^{-\alpha(x-y)} f(y) dy \right) = -\alpha \mathcal{I}_x^R[f](x) + \alpha f(x), \quad (54)$$

$$\frac{d}{dx} (\mathcal{I}_x^L[f](x)) = \frac{d}{dx} \left(\alpha \int_x^b e^{-\alpha(y-x)} f(y) dy \right) = \alpha \mathcal{I}_x^L[f](x) - \alpha f(x), \quad (55)$$

These results can be combined according to (49), which provides an expression for the derivative of the convolution term:

$$\frac{d}{dx} (\mathcal{I}_x[f](x)) = \frac{\alpha}{2} \left(-\mathcal{I}_x^R[f](x) + \mathcal{I}_x^L[f](x) \right). \quad (56)$$

Additionally, by evaluating this equation at the ends of the interval, we obtain the identities

$$\frac{d}{dx} \left(\mathcal{I}_x[f](a) \right) = \alpha \mathcal{I}_x[f](a), \quad (57)$$

$$\frac{d}{dx} \left(\mathcal{I}_x[f](b) \right) = -\alpha \mathcal{I}_x[f](b), \quad (58)$$

which are helpful in enforcing the boundary conditions. The relation (56) can be used to obtain a derivative for the solution at the new time level. From the update (53), a direct computation reveals that

$$\frac{du^{n+1}}{dx} = \frac{\alpha}{2} \left(-\mathcal{I}_x^R[R](x) + \mathcal{I}_x^L[R](x) \right) - \alpha A e^{-\alpha(x-a)} + \alpha B e^{-\alpha(b-x)}. \quad (59)$$

Notice that no additional approximations have been made beyond what is needed to compute \mathcal{I}_x^R and \mathcal{I}_x^L . These terms are already evaluated as part of the base method. For this reason, we think of equation (59) as an analytical derivative. The boundary coefficients A and B appearing in (59) will be calculated in the same way as the update (53), and are discussed in the remaining subsections. This treatment ensures that the discrete derivative will be consistent with the conditions imposed on the solution variable.

3.4.1 Dirichlet Boundary Conditions

Suppose we are given the function values along the boundary, which is represented by the data

$$u^{n+1}(a) = g_a(t^{n+1}), \quad u^{n+1}(b) = g_b(t^{n+1}).$$

If we evaluate the BDF-1 update (53) at the ends of the interval, we obtain the conditions

$$\begin{aligned} g_a(t^{n+1}) &= \mathcal{I}_x[R](a) + A + \mu B, \\ g_b(t^{n+1}) &= \mathcal{I}_x[R](b) + \mu A + B, \end{aligned}$$

where we have defined $\mu = e^{-\alpha(b-a)}$. This is a simple linear system for the boundary coefficients A and B , which can be inverted by hand. Proceeding, we find that

$$\begin{aligned} A &= \frac{g_a(t^{n+1}) - \mathcal{I}_x[R](a) - \mu(g_b(t^{n+1}) - \mathcal{I}_x[R](b))}{1 - \mu^2}, \\ B &= \frac{g_b(t^{n+1}) - \mathcal{I}_x[R](b) - \mu(g_a(t^{n+1}) - \mathcal{I}_x[R](a))}{1 - \mu^2}. \end{aligned}$$

3.4.2 Neumann Boundary Conditions

We can also enforce conditions on the derivatives at the end of the domain. Given the Neumann data

$$\frac{du^{n+1}(a)}{dx} = h_a(t^{n+1}), \quad \frac{du^{n+1}(b)}{dx} = h_b(t^{n+1}),$$

we can evaluate the derivative formula for the update (59) and use the identities (57) and (58). Performing these evaluations, we obtain the system of equations

$$\begin{aligned} -A + \mu B &= \frac{1}{\alpha} h_a(t^{n+1}) - \mathcal{I}_x[R](a), \\ -\mu A + B &= \frac{1}{\alpha} h_b(t^{n+1}) + \mathcal{I}_x[R](b), \end{aligned}$$

where, again, $\mu = e^{-\alpha(b-a)}$. Solving this system, we find that

$$\begin{aligned} A &= -\frac{\frac{1}{\alpha} h_a(t^{n+1}) - \mathcal{I}_x[R](a) - \mu \left(\frac{1}{\alpha} h_b(t^{n+1}) + \mathcal{I}_x[R](b) \right)}{1 - \mu^2}, \\ B &= -\frac{\mu \left(\frac{1}{\alpha} h_a(t^{n+1}) - \mathcal{I}_x[R](a) \right) - \left(\frac{1}{\alpha} h_b(t^{n+1}) + \mathcal{I}_x[R](b) \right)}{1 - \mu^2}. \end{aligned}$$

We note that Robin boundary conditions, which combine Dirichlet and Neumann conditions can be enforced in a nearly identical manner.

3.4.3 Periodic Boundary Conditions

Periodic boundary conditions are enforced by taking

$$u^{n+1}(a) = u^{n+1}(b), \quad \partial_x u^{n+1}(a) = \partial_x u^{n+1}(b).$$

Enforcing these conditions through the update (53) and its derivative (59), using the identities (57)-(58), leads to the system of equations

$$\begin{aligned} (1 - \mu)A + (\mu - 1)B &= \mathcal{I}_x[R](b) - \mathcal{I}_x[R](a), \\ (\mu - 1)A + (\mu - 1)B &= -\mathcal{I}_x[R](b) - \mathcal{I}_x[R](a), \end{aligned}$$

with $\mu = e^{-\alpha(b-a)}$. The solution of this system, after some simplifications is given by

$$\begin{aligned} A &= \frac{\mathcal{I}_x[R](b)}{1 - \mu}, \\ B &= \frac{\mathcal{I}_x[R](a)}{1 - \mu}. \end{aligned}$$

3.4.4 Outflow Boundary Conditions

In problems defined over free-space, we must allow for waves to exit the computational domain. Additionally, as the waves exit the domain, we would like to minimize the number of reflections, which are non-physical, along this boundary. Exit conditions can be formulated in one-dimension in the sense of characteristics, by requiring that

$$\frac{\partial u}{\partial t} - c \frac{\partial u}{\partial x} = 0, \quad x = a, \tag{60}$$

$$\frac{\partial u}{\partial t} + c \frac{\partial u}{\partial x} = 0, \quad x = b, \tag{61}$$

where $c > 0$ is the wave speed.

To formulate the boundary conditions for the first-order BDF update (52), we follow the approach used in [47]. This paper developed outflow boundary conditions for a variant of the proposed solver, in which the time derivatives are discretized with time-centered stencils. The development of outflow boundary conditions starts from the free-space solution that is defined over the real line:

$$u^{n+1}(x) = \frac{\alpha}{2} \int_{-\infty}^{\infty} e^{-\alpha|x-y|} R(y) dy.$$

Here, $R(x)$ is the operand for the BDF-1 method given by (ignoring sources)

$$R(x) = 2u^n - u^{n-1}.$$

Using the finite speed of propagation and assuming that the support of $u(x, 0)$ and $R(x)$ is entirely contained within the domain $[a, b]$, it follows that the free-space solution can be written in the familiar form (53):

$$u^{n+1}(x) = \mathcal{I}_x[R](x) + A^n e^{-\alpha(x-a)} + B^n e^{-\alpha(b-x)}.$$

In the above, we have employed the definitions

$$A^n = \frac{\alpha}{2} \int_{a-ct^n}^a e^{-\alpha(a-y)} R(y) dy, \tag{62}$$

$$B^n = \frac{\alpha}{2} \int_b^{b+ct^n} e^{-\alpha(y-b)} R(y) dy. \tag{63}$$

Since these integrals are defined over regions of space outside of the computational domain, the idea is now to exchange space with time, using the characteristics of equations (60) and (61).

A key difference between the BDF and time-centered approaches is the definition of the operand in the convolution operators. In the time centered approach, the operand consists of a single time level $u^n(x)$, while the BDF methods use additional time levels, e.g., $u^{n-1}(x)$, $u^{n-2}(x)$, etc; however, the outflow approach developed for the time-centered method [47] can still be used in the BDF method. Through Taylor expansion, it is straightforward to verify that

$$2u^n(x) - u^{n-1}(x) = u^n + \partial_t u^n(x)\Delta t + \mathcal{O}(\Delta t^2). \quad (64)$$

The linearization (64), which is used only along the boundary points, turns out to be quite effective for problems with slow variations in time as well as steady-state problems. The Taylor expansion shows that in such situations, the time derivatives become small so that higher-order terms can be neglected. Therefore, if we approximate the operand R along the boundary $x = b$ with $u(b, t^n - y)$, it follows that

$$\begin{aligned} B^n &= \frac{\alpha c}{2} \int_0^{t^n} e^{-\alpha c y} u(b, t^n - y) dy, \\ &= \frac{\alpha c}{2} \int_0^{\Delta t} e^{-\alpha c y} u(b, t^n - y) dy + \frac{\alpha c}{2} \int_{\Delta t}^{t^n} e^{-\alpha c y} u(b, t^n - y) dy, \\ &\equiv I_1 + I_2, \end{aligned}$$

where the second integral I_2 can be written in the form

$$\begin{aligned} I_2 &= \frac{\alpha c}{2} \int_0^{t^{n-1}} e^{-\alpha c(y+\Delta t)} u(b, t^{n-1} - y) dy, \\ &= e^{-1} \left(\frac{\alpha c}{2} \int_0^{t^{n-1}} e^{-\alpha c y} u(b, t^{n-1} - y) dy \right), \\ &\equiv e^{-1} B^{n-1}. \end{aligned} \quad (65)$$

Note that the simplifications shown above use the definition $\alpha = 1/(c\Delta t)$ for the BDF-1 method.

Likewise, the first integral I_1 , can be expressed as

$$I_1 = \frac{1}{2} \int_0^1 e^{-z} u(b, t^n - z\Delta t) dz, \quad (66)$$

using the definition $\alpha = 1/(c\Delta t)$. As with the BDF-1 method, this integral can be evaluated analytically after constructing an interpolating function for $u(b, t^n - z\Delta t)$. If we approximate the function $u(b, t^n - z\Delta t)$ using algebraic polynomials with the data $\{u^{n-2}(b), u^{n-1}(b), u^n(b)\}$ as the stencil, we obtain the coefficient

$$B^n = e^{-\beta} B^{n-1} + \gamma_0 u^n(b) + \gamma_1 u^{n-1}(b) + \gamma_2 u^{n-2}(b),$$

where the integration weights are given by

$$\begin{aligned} \gamma_0 &= \frac{2e^{-\beta} - \beta + 2\beta^2 + 3\beta e^{-\beta} - 2}{4\beta^2}, \\ \gamma_1 &= -\frac{2e^{-\beta} - 2\beta + 3\beta^2 e^{-\beta} + 4\beta e^{-\beta} - 2}{6\beta^2}, \\ \gamma_2 &= -\frac{\beta + 2e^{-\beta} + \beta e^{-\beta} - 2}{12\beta^2}, \end{aligned}$$

with $\beta = 1$.

3.4.5 Treatment of Boundary Conditions in Multi-dimensional Problems

In this section we briefly discuss some of the issues concerning the application of boundary conditions for the multi-dimensional update given by (41) for the BDF-1 method. For convenience, the two-dimensional BDF-1 update is

$$\mathcal{L}_x \mathcal{L}_y u^{n+1}(\mathbf{x}) = 2u^n(\mathbf{x}) - u^{n-1}(\mathbf{x}) + \frac{1}{\alpha^2} S^{n+1}(\mathbf{x}), \quad \alpha := \frac{1}{c\Delta t}.$$

By inverting the operator, one direction at a time, using the techniques presented in 3.3, it follows that the solution is given by

$$u^{n+1} = \mathcal{L}_x^{-1} \mathcal{L}_y^{-1} \left(2u^n - u^{n-1} + \frac{1}{\alpha^2} S^{n+1} \right) (\mathbf{x}).$$

We wish to point out here that things are assumed to be smooth so that the ordering conventions used for operators are irrelevant. In other words, we can assume

$$\mathcal{L}_x \mathcal{L}_y = \mathcal{L}_y \mathcal{L}_x.$$

3.4.5.1 A Comment on Sweeping Patterns in Multi-dimensional Problems

In the two-dimensional case, we need to construct terms of the form

$$\mathcal{L}_y \mathcal{L}_x w = f \implies w = \mathcal{L}_x^{-1} \mathcal{L}_y^{-1} (f),$$

with boundary data being prescribed for the variable w . The construction is performed over two steps. The first step inverts the y operator, so we obtain

$$\mathcal{L}_x w = \mathcal{L}_y^{-1} (f). \tag{67}$$

The first layer of sweeps given by equation (67) requires boundary data for the intermediate variable $\mathcal{L}_x w$ when we are only given boundary data for w . From the definition of \mathcal{L}_x , we note that

$$\mathcal{L}_x w \equiv \left(\mathcal{I} - \frac{1}{\alpha^2} \partial_{xx} \right) w = w + \mathcal{O} \left(\frac{1}{\alpha^2} \right), \tag{68}$$

In other words, boundary conditions for $\mathcal{L}_x w$ can be approximated to second-order in time by those of w ; however, unless we are dealing with outflow boundary conditions, we do not need to sweep along the boundary of the domain, so the approximation (68) is not necessary. Proceeding further, the second step of the inversion process leads to the solution w

$$w = \mathcal{L}_x^{-1} \mathcal{L}_y^{-1} (f), \tag{69}$$

which simply enforces the known boundary data on w . In the subsections that follow, we briefly summarize the changes associated with moving to multi-dimensional problems, including any changes necessitated by the proposed methods for calculating derivatives.

3.4.5.2 Dirichlet Boundary Conditions

In the case of Dirichlet boundary conditions, the values of the function are known along the boundary. Therefore, we only need to update the grid points corresponding to the interior of the domain. As mentioned earlier, rather than approximating the boundary conditions for the intermediate sweep, e.g., (68), we simply avoid sweeping along the boundary points of the domain, since these values are known. The direction corresponding to the intermediate sweep will now only use boundary data set by the solution, since the boundaries are left untouched. In the case of homogeneous Dirichlet conditions, the sweeps can be performed on the boundary with no effect. When sweeping over different directions for the derivatives, we note that along the boundary, the derivative information is not known. Therefore, the sweeps should extend all the way to the boundary. Otherwise the derivative will not be available there. In this case, the boundary data for the intermediate data can be approximated according to (68).

3.4.5.3 Neumann Boundary Conditions

The treatment of Neumann boundary conditions in multi-dimensional problems is identical to the procedure used to enforce Dirichlet boundary conditions discussed in the previous section for the case of Cartesian grids. In problems defined on complex geometries with embedded boundaries, the theory presented in [70] suggests that dissipation is necessary to obtain stable numerical solutions [47] to the Neumann problem. This is not a problem for the BDF method, which is known to be dissipative. The treatment of Neumann boundary conditions for problems with curved boundaries was given in [47]. In such a setting, the normal direction along the curved boundary couples the sweeping directions of the interior grid points in a non-trivial manner. Authors in [47] devised an iterative technique that uses Hermite interpolation in the vicinity of the boundary to supply Dirichlet data at the ends of the lines over which sweeps are performed. Note that these caveats are also relevant to the proposed method for computing derivatives.

3.4.5.4 Periodic Boundary Conditions

Periodic boundary conditions in multi-dimensional problems can be enforced in a straightforward way by directly applying the one-dimensional approaches outlined in section 3.4.3 along each dimension. No modifications are required for either the scheme or the proposed method for calculating derivatives.

3.4.5.5 Outflow Boundary Conditions

In section 3.4.4, we obtained expressions for the boundary coefficients that enforce outflow boundary conditions. Using a Taylor expansion in time along the boundary points, the operand was approximated using data from a single time level. This has several advantages. Firstly, the simplifications made possible by the Taylor expansion allow us to appeal to an earlier outflow approach developed for the time-centered method [47] with minimal changes. Among the approaches introduced in this reference, we advocate for the “explicit” treatment of outflow, which essentially utilizes an extrapolant for the data along the boundary. This choice is effective at eliminating the spurious reflections introduced by the alternative “implicit” approach, which is generally inconsistent in the multi-dimensional setting because it relies on the particular form of the update. Second, the structure of the time history used in the convolution integral follows a regular pattern in the sense that the first and second layers of sweeps, respectively defined by (67) and (69), operate on data from single time level. This greatly simplifies the implementation since the structure of the operand remains unchanged between the layers of sweeps. To illustrate, with the sweeping pattern (69), we would first need to evaluate the term (ignoring sources)

$$v^{(1)}(\mathbf{x}) = \mathcal{L}_y^{-1} (2u^n - u^{n-1})(\mathbf{x}),$$

which requires tracking a time history for the difference $2u^n - u^{n-1}$ at the y boundary points. In contrast, the second set of sweeps (following (69)), which performs the evaluation

$$v^{(2)}(\mathbf{x}) = \mathcal{L}_x^{-1} (v^{(1)})(\mathbf{x}),$$

requires the time history for $v^{(1)}$, now along boundary the x boundary points.

Lastly, we remark on the treatment of derivatives in multi-dimensional problems. In section 3.4, we obtained an equation for spatial derivatives of the scalar fields through a direct calculation involving the one-dimensional BDF-1 method. This, in turn, led to equation (59). Since the directions over which sweeps occur are treated independently, the one-dimensional derivatives can be applied in a dimensionally-split manner for multi-dimensional problems. When combined with outflow boundary conditions, care should be taken to ensure that the time history used in the reconstruction is consistent with the operand of a particular convolution integral. To illustrate, assuming a sweeping pattern of the form (69), we find that the BDF-1 update in two spatial dimensions has the form

$$u^{n+1}(\mathbf{x}) = \mathcal{L}_x^{-1} \mathcal{L}_y^{-1} (R)(\mathbf{x}), \quad (70)$$

where we used

$$R(\mathbf{x}) = 2u^n(\mathbf{x}) - u^{n-1}(\mathbf{x}) + \frac{1}{\alpha^2} S^{n+1}(\mathbf{x}).$$

Alternatively, if we swapped the order in which sweeps are performed, we obtain a similar update

$$u^{n+1}(\mathbf{x}) = \mathcal{L}_y^{-1} \mathcal{L}_x^{-1}(R)(\mathbf{x}), \quad (71)$$

with R being unchanged. Now, consider a y -derivative of the schemes (70) and (71). Since the inverse operator \mathcal{L}_x^{-1} varies only with respect to x and remains constant in y , then these sweeping patterns provide two options to compute y -derivatives, namely

$$\partial_y u^{n+1}(\mathbf{x}) = \mathcal{L}_x^{-1} \left(\partial_y \mathcal{L}_y^{-1}(R) \right), \quad (72)$$

$$\partial_y u^{n+1}(\mathbf{x}) = \partial_y \mathcal{L}_y^{-1} \left(\mathcal{L}_x^{-1}(R) \right). \quad (73)$$

Both options are equally valid ways of computing derivatives for the multi-dimensional setting, but, in problems with outflow boundary conditions, the data that is stored in each approach is different. In the first approach (72), the outflow boundary conditions require the time history for the intermediate variable whose derivative we seek. The second approach (73) proceeds in a manner which is more closely related to the update of the solution, since the derivative (59) does not change A and B along a given line. For this reason, we prefer the structure of the second option (71) in our implementation to compute the y derivative. Similarly, the x derivative follows the pattern (70).

3.5 Summary

In this section we discussed the methods used for the fields. Inspired by the underlying connection to integral equations, we obtained analytical expressions for the spatial derivatives of the scalar fields. The evaluation of the derivatives relies on the same core algorithms used to evolve the scalar fields, allowing the proposed methods for derivatives to naturally inherit the geometric flexibility offered by the base field solver. We discussed the essential components used to solve these one-dimensional problems including the fast summation method, as well as the application of boundary conditions. In the next section, we combine the proposed methods for fields and their derivatives with time integration methods for particles to construct new particle-in-cell methods for plasmas.

4 Development of a New Particle-in-cell Method

This section describes the construction of a particle-in-cell (PIC) method for plasmas that leverages the field solvers introduced in the previous section. We begin by introducing the concept of a macro-particle that is the foundation of all PIC methods in section 4.1. Then, we present several recently developed time integration methods for non-separable Hamiltonian systems in section 4.2, which are designed to advance the particles in the generalized momentum formulation. Algorithms which couple the time integration methods for particles with the proposed field solvers are also presented. A brief summary of the section contents is presented in section 4.3.

4.1 Moving from Point-particles to Macro-particles

An essential feature of PIC methods is that the simulation particles are not physical particles. Instead, they represent a collection of particles sampled from an underlying probability distribution function. For this reason, they are often called super-particles or macro-particles. It is important to note that the motion of the physical particles that comprise a given macro-particle are not tracked during a simulation. The

particular “size” of this sample is reflected in the weight associated with a given macro-particle w_{mp} , which can be calculated as

$$w_{mp} = \frac{N_{\text{real}}}{N_{\text{simulation}}}.$$

Here, we use N_{real} to denote the number of physical particles contained within a simulation domain and $N_{\text{simulation}}$ to be the number of simulation particles. The calculation of N_{real} is problem dependent, but can be expressed in terms of the average macroscopic number density \bar{n} that describes the plasma and a volume that is associated with either the domain or beam being considered. Once the weight for each particle is calculated, it can be absorbed into properties of the particle species, such as the charge, so that $w_{mp}q_i$ can be shortened to q_i .

In section 2.3, the charge density and current density were defined in equations (13) and (14) using a linear combination of Dirac delta distributions for a collection of N_p simulation particles. While PIC methods can be developed to work with these point-particle representations (see e.g., [38]), most PIC methods, including the ones developed in this work, represent particles using shape functions so that

$$\rho(\mathbf{x}, t) = \sum_{p=1}^{N_p} q_p S(\mathbf{x} - \mathbf{x}_p(t)), \quad (74)$$

$$\mathbf{J}(\mathbf{x}, t) = \sum_{p=1}^{N_p} q_p \mathbf{v}_p(t) S(\mathbf{x} - \mathbf{x}_p(t)), \quad (75)$$

where the shape function S is now used to represent a simulation particle. The shape functions most often employed in PIC simulations are B-splines, which are compact (local) and positive. Furthermore, they can be easily extended to include additional dimensions using tensor products of univariate splines. While higher-order splines produce smoother mappings to the mesh and possess higher degrees of continuity, the extended support regions create complications in plasma simulations on bounded domains. For simplicity, the particle methods developed in this work employ linear splines to represent particle shapes. The linear spline function that represents the particle x_p on the mesh with spacing Δx is given by

$$S(x - x_p) = \begin{cases} 1 - \frac{|x - x_p|}{\Delta x}, & 0 \leq \frac{|x - x_p|}{\Delta x} \leq 1, \\ 0, & \frac{|x - x_p|}{\Delta x} > 1. \end{cases} \quad (76)$$

The shape function (76) generally serves two purposes: (1) It provides a way to map particle data onto the mesh (scatter operation) and (2) can be used to interpolate mesh based quantities to the particles during the time integration (gather operation). For consistency in a PIC method, it is important that these maps be identical. In the next section, we discuss methods used to evolve the generalized momentum formulation for particles.

4.2 Time Integration with Non-separable Hamiltonians

In this section, we describe the time integration methods used to evolve the simulation particles. In contrast to the usual Newton-Lorenz treatment for particles, the adoption of generalized momentum results in a non-separable Hamiltonian system that requires a special integration method. We provide an outline of the base time integration method in section 4.2.1 and offer an improvement in section 4.2.2 that includes a correction from a Taylor expansion.

4.2.1 The Asymmetrical Euler Method

A time integration method suitable for non-separable Hamiltonian systems was recently proposed in [50], which developed mesh-free methods for solving the VM system in the Darwin limit. Their adoption of a generalized Hamiltonian model for particles was largely motivated by the numerical instabilities associated

with time derivatives of the vector potential in this particular limit, which effectively sends the speed of light $c \rightarrow \infty$. The resulting model, which is essentially identical to the formulation (23)-(24) considered in this work, trades additional coupling of phase space for numerical stability through the elimination of this time derivative. They proposed a semi-implicit method, dubbed the asymmetrical Euler method (AEM), which has the form

$$\mathbf{x}_i^{n+1} = \mathbf{x}_i^n + \mathbf{v}_i^n \Delta t, \quad (77)$$

$$\mathbf{P}_i^{n+1} = \mathbf{P}_i^n + q_i \left(-\nabla \psi^{n+1} + \nabla \mathbf{A}^{n+1} \cdot \mathbf{v}_i^n \right) \Delta t, \quad (78)$$

$$\mathbf{v}_i^n \equiv \frac{1}{m_i} (\mathbf{P}_i^n - q_i \mathbf{A}^n). \quad (79)$$

This method, which is first-order in time, proceeds by, first, performing an explicit update of the particle positions using (77). Next, with the new positions \mathbf{x}^{n+1} and the old velocity \mathbf{v}^n , we obtain the charge density ρ^{n+1} and an approximate current density $\tilde{\mathbf{J}}^{n+1}$ which are used to evolve the fields under the BDF-1 discretization. We note that the use of \mathbf{v}^n in the construction of $\tilde{\mathbf{J}}^{n+1}$ is consistent with a first-order approximation of the true current density \mathbf{J}^{n+1} . Finally, once the fields are updated, the generalized momentum \mathbf{P}^{n+1} and its corresponding velocity \mathbf{v}^{n+1} are updated according to equations (78) and (79), respectively.

4.2.2 An Improved Asymmetrical Euler Method

One of the issues with the AEM, which was discussed in the previous section, concerns the explicit treatment of velocity in the generalized momentum equation for problems with magnetic fields. In such cases this update resembles the explicit Euler method, which is known to generate artificial energy when applied to Hamiltonian systems. We offer a simple modification for such problems in an effort to increase the accuracy and reduce such energy violations. If the update for the generalized momentum equation (78) were treated implicitly with a backwards Euler discretization, then we would instead compute

$$\mathbf{P}_i^{n+1} = \mathbf{P}_i^n + q_i \left(-\nabla \psi^{n+1} + \nabla \mathbf{A}^{n+1} \cdot \mathbf{v}_i^{n+1} \right) \Delta t.$$

Unfortunately, this approach necessitates iteration on \mathbf{P}_i^{n+1} , which we are trying to avoid. Instead, with the aid of a Taylor expansion, we linearize the velocity about time level t^n so that

$$\begin{aligned} \mathbf{v}_i^{n+1} &= \mathbf{v}_i^n + \frac{d\mathbf{v}_i^n}{dt} \Delta t + \mathcal{O}(\Delta t^2), \\ &\approx 2\mathbf{v}_i^n - \mathbf{v}_i^{n-1}, \\ &\equiv \mathbf{v}_i^*. \end{aligned}$$

This treatment is still not symplectic; however, the numerical results presented in section 5 for the evolution of a single particle indicate that the improved accuracy from the linear correction manages to tame the otherwise significant energy increase introduced by the explicit Euler discretization. Therefore, in problems with magnetic fields, we shall, instead, use the modified update

$$\begin{aligned} \mathbf{P}_i^{n+1} &= \mathbf{P}_i^n + q_i \left(-\nabla \psi^{n+1} + \nabla \mathbf{A}^{n+1} \cdot \mathbf{v}_i^* \right) \Delta t, \\ \mathbf{v}_i^* &= 2\mathbf{v}_i^n - \mathbf{v}_i^{n-1}, \end{aligned}$$

as an improvement to the generalized momentum update (78). Since this approach is used to evolve particles in the electromagnetic examples considered in this work, its integration with the PIC lifecycle is presented in Algorithm 1. Henceforth, we shall call refer to this as the improved asymmetrical Euler methods (IAEM).

Algorithm 1 Outline of the PIC algorithm with the improved asymmetric Euler method (IAEM)

Perform one time step of the PIC cycle using the improved asymmetric Euler method.

- 1: **Given:** $(\mathbf{x}_i^0, \mathbf{P}_i^0, \mathbf{v}_i^0)$, as well as the fields $(\psi^0, \nabla\psi^0)$ and $\mathbf{A}^0, \nabla\mathbf{A}^0$
- 2: Initialize $\mathbf{v}_i^{-1} = \mathbf{v}_i(-\Delta t)$ using the second-order Taylor approximation

$$\mathbf{v}_i^{-1} \approx \mathbf{v}_i^0 - \frac{q_i}{m_i} (-\nabla\psi^0 + \nabla\mathbf{A}^0 \cdot \mathbf{v}^0) \Delta t.$$

- 3: **while** stepping **do**

- 4: Update the particle positions with

$$\mathbf{x}_i^{n+1} = \mathbf{x}_i^n + \mathbf{v}_i^n \Delta t.$$

- 5: Using the position data \mathbf{x}_i^{n+1} , compute the charge density ρ^{n+1} .
- 6: Using the position data \mathbf{x}_i^{n+1} and velocity data \mathbf{v}_i^n , compute the current density

$$\tilde{\mathbf{J}}^{n+1} = \mathbf{J}^{n+1} + \mathcal{O}(\Delta t).$$

- 7: Compute the potentials and their derivatives at time level t^{n+1} using the BDF-1 field solver.
- 8: Evaluate the Taylor corrected particle velocities

$$\mathbf{v}_i^* = 2\mathbf{v}_i^n - \mathbf{v}_i^{n-1}.$$

- 9: Calculate the new generalized momentum according to

$$\mathbf{P}_i^{n+1} = \mathbf{P}_i^n + q_i \left(-\nabla\psi^{n+1} + \nabla\mathbf{A}^{n+1} \cdot \mathbf{v}_i^* \right) \Delta t.$$

- 10: Convert the new generalized momenta into new particle velocities with

$$\mathbf{v}_i^{n+1} = \frac{1}{m_i} (\mathbf{P}_i^{n+1} - q_i \mathbf{A}^{n+1}).$$

- 11: Shift the time history data and return to step 4 to begin the next time step.
-

4.3 Summary

In this section we proposed new PIC methods for the numerical simulation of plasmas. To this end, we combined methods for fields and their derivatives, which were introduced in section 3, with time integration methods for non-separable Hamiltonian systems. A high level description of the particle method was presented. In the next section, we present results from the numerical experiments conducted with the algorithms introduced in this paper. First, we establish the refinement properties of the field solver and methods for derivatives. Then, we demonstrate the performance of the proposed PIC methods in several key test problems involving plasmas with varying complexity.

5 Numerical Examples

This section presents numerical results that demonstrate the proposed methods for fields and particles that comprise the formulation adopted in this work. First, we establish the convergence properties of the BDF field solver and methods for evaluating spatial derivatives. The proposed methods are demonstrated using boundary conditions that will be considered in the applications involving plasmas. Once the refinement properties of the field solver are established, we focus on applications to plasmas. We begin with a single particle example involving cyclotron motion before moving to more complex problems involving self-fields.

After benchmarking the time integration methods used for the generalized momentum formulation, we apply the proposed PIC methods to a suite of electrostatic and electromagnetic test problems.

5.1 Numerical Experiments for Field Solvers

In this section we establish the refinement properties of the BDF field solver and the proposed methods for computing spatial derivatives. Results for space and time refinement experiments are presented from a suite of two-dimensional test problems using boundary conditions that are relevant to the plasma examples considered in this work.

5.1.1 Periodic Boundary Conditions

We first consider the two-dimensional in-homogeneous scalar wave equation

$$\partial_{tt}u - \Delta u = S(x, y), \quad (80)$$

and

$$S(x, y) = 3e^{-t} \sin(x) \cos(y). \quad (81)$$

We apply two-way periodic boundary conditions on the domain $[0, 2\pi] \times [0, 2\pi]$ and use the initial data

$$u(x, y, 0) = \sin(x) \cos(y), \quad \partial_t u(x, y, 0) = -\sin(x) \cos(y). \quad (82)$$

The problem (80) is associated with the manufactured solution

$$u(x, y, t) = e^{-t} \sin(x) \cos(y), \quad (83)$$

and defines the source function (81). The partial derivatives of this solution are calculated to be

$$\partial_x u(x, y, t) = e^{-t} \cos(x) \cos(y), \quad (84)$$

$$\partial_y u(x, y, t) = -e^{-t} \sin(x) \sin(y). \quad (85)$$

For the space refinement experiment, we varied the spatial mesh in each direction from 16 points to 512 points. To keep the temporal error in the methods small during the refinement, we applied the methods for 1 time step using a step size of $\Delta t = 1 \times 10^{-4}$. The refinement plots in Figure 1 indicate fifth-order accuracy in space for all methods. We note that the derivatives in the methods begin to level-off as the error approaches 1×10^{-11} . This is likely due to a different error coefficient in time, which arises from the differentiation process. A smaller time step would be necessary to remove this feature, but this requires some modification of the quadrature.

In the temporal refinement study, the solution is computed until a final time of $T = 1$ using a fixed 256×256 mesh in space. We successively double the number of time steps from $N_t = 8$ until $N_t = 512$. We use the analytical solution to initialize the method, since it is available. The results of the temporal refinement study are presented in Figure 1, in which all methods, including those for the derivatives, display the expected first-order convergence rate in time.

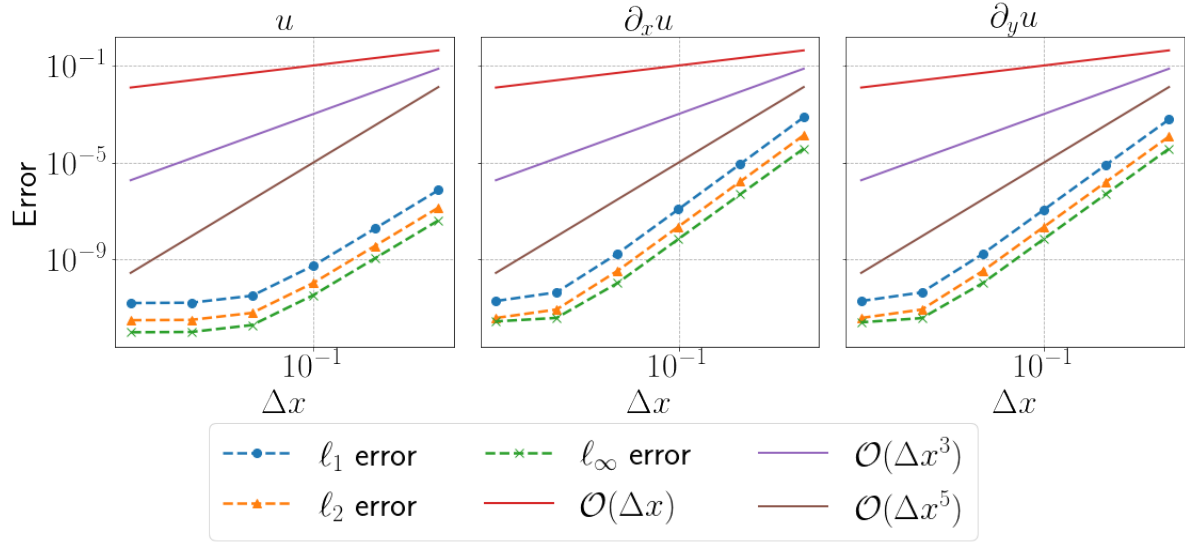
5.1.2 Dirichlet Boundary Conditions

For the Dirichlet problem, we consider the two-dimensional in-homogeneous scalar wave equation

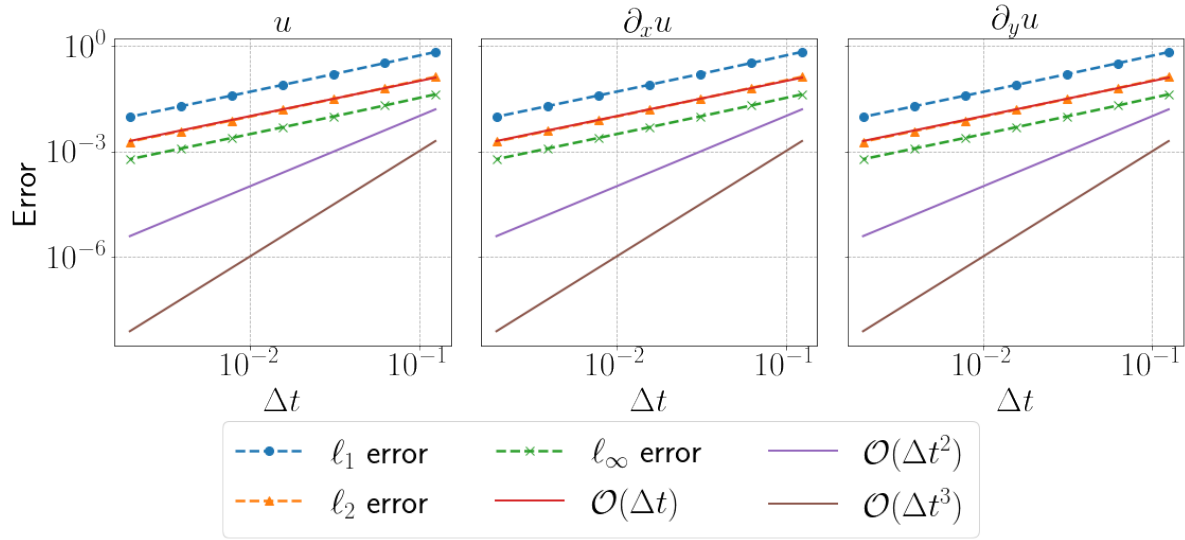
$$\partial_{tt}u - \Delta u = S(x, y), \quad (86)$$

and

$$S(x, y) = 3e^{-t} \sin(x) \sin(y). \quad (87)$$

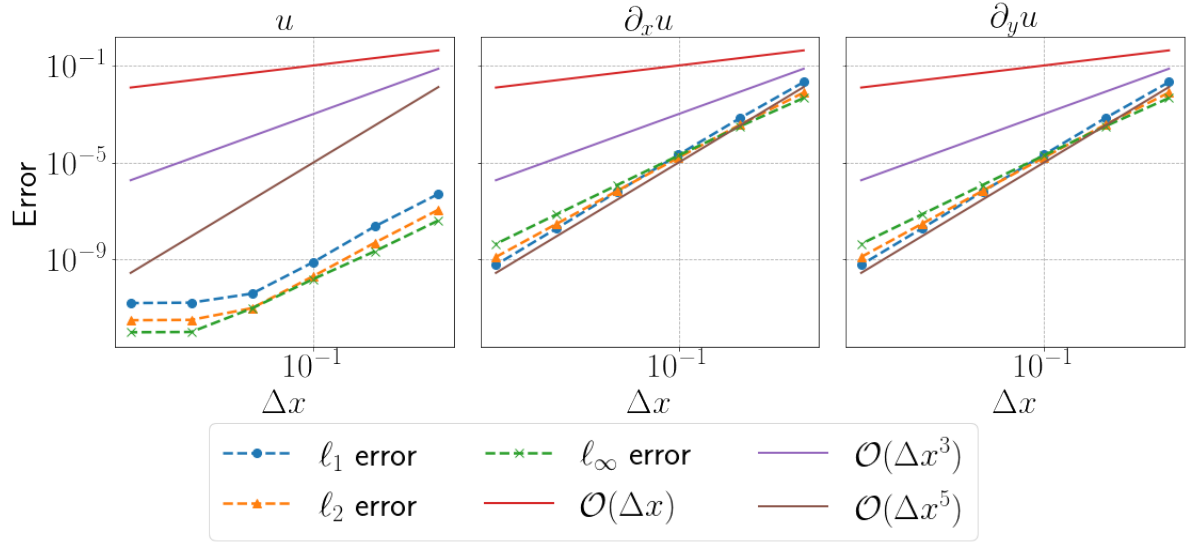


(a)

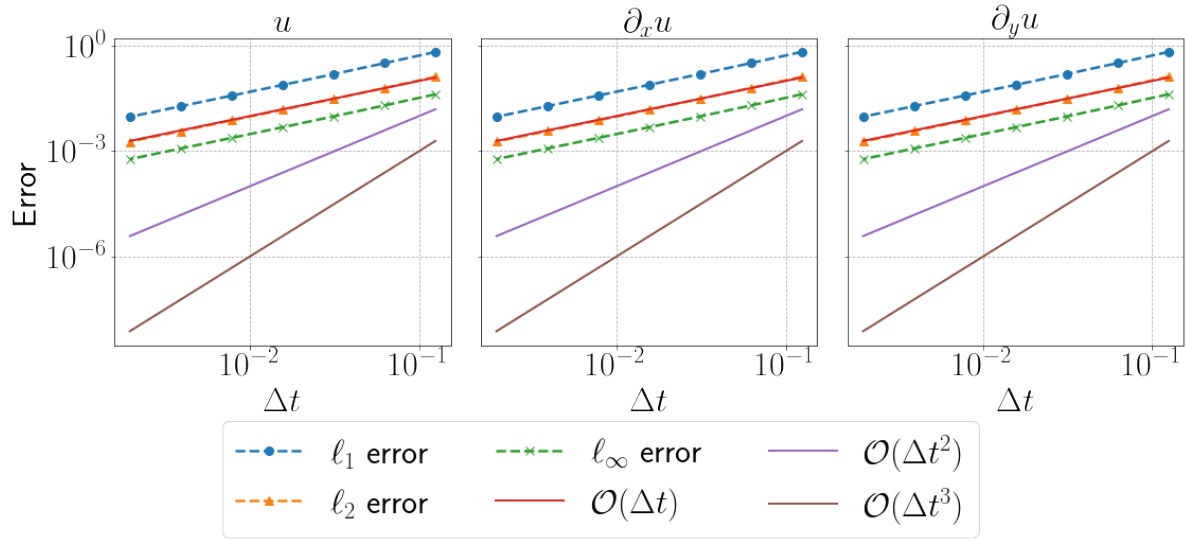


(b)

Figure 1: Space-time refinement of the solution and its spatial derivatives for the two-dimensional periodic example 5.1.1 obtained with the first-order BDF method.



(a)



(b)

Figure 2: Space-time refinement of the solution and its spatial derivatives for the two-dimensional Dirichlet problem 5.1.2 obtained with the first-order BDF method.

We apply homogeneous Dirichlet boundary conditions on the domain $[0, 2\pi] \times [0, 2\pi]$ and use the initial data

$$u(x, y, 0) = \sin(x) \sin(y), \quad \partial_t u(x, y, 0) = -\sin(x) \sin(y). \quad (88)$$

The problem (80) is associated with the manufactured solution

$$u(x, y, t) = e^{-t} \sin(x) \sin(y), \quad (89)$$

and defines the source function (87). The partial derivatives of this solution are calculated to be

$$\partial_x u(x, y, t) = e^{-t} \cos(x) \sin(y), \quad (90)$$

$$\partial_y u(x, y, t) = e^{-t} \sin(x) \cos(y). \quad (91)$$

We performed the spatial refinement study by varying the number of mesh points in each direction from 16 points to 512 points. Again, to keep the temporal error in the methods small while space is refined, we applied the methods for only 1 time step with a step size of $\Delta t = 1 \times 10^{-4}$. The same remark about small time step sizes mentioned in the space refinement experiment for the periodic case applies here, as well (see section 5.1.1). The refinement plots in Figure 2 indicate that the methods refine, approximately, to fifth-order in space. In both the mixed and pure BDF approaches, the error in the derivatives behaves differently from what was observed in the periodic example. In particular, we do not observe a flattening of the error when the spacing Δx is small.

In the temporal refinement study, the solution is computed until a final time of $T = 1$. We use a fixed 256×256 spatial mesh and the number of time steps in each case is successively doubled from $N_t = 8$ until $N_t = 512$. Errors can be directly measured with the analytical solution and its derivatives. The results of the temporal refinement study are presented in Figure 2, in which all methods, including those for the derivatives, display the expected first-order convergence rate. The behavior is essentially identical to the results obtained for the periodic problem presented in Figure 1.

5.1.3 Outflow Boundary Conditions

To test outflow boundary conditions, we use the homogeneous scalar wave equation

$$\partial_{tt} u - \Delta u = 0. \quad (92)$$

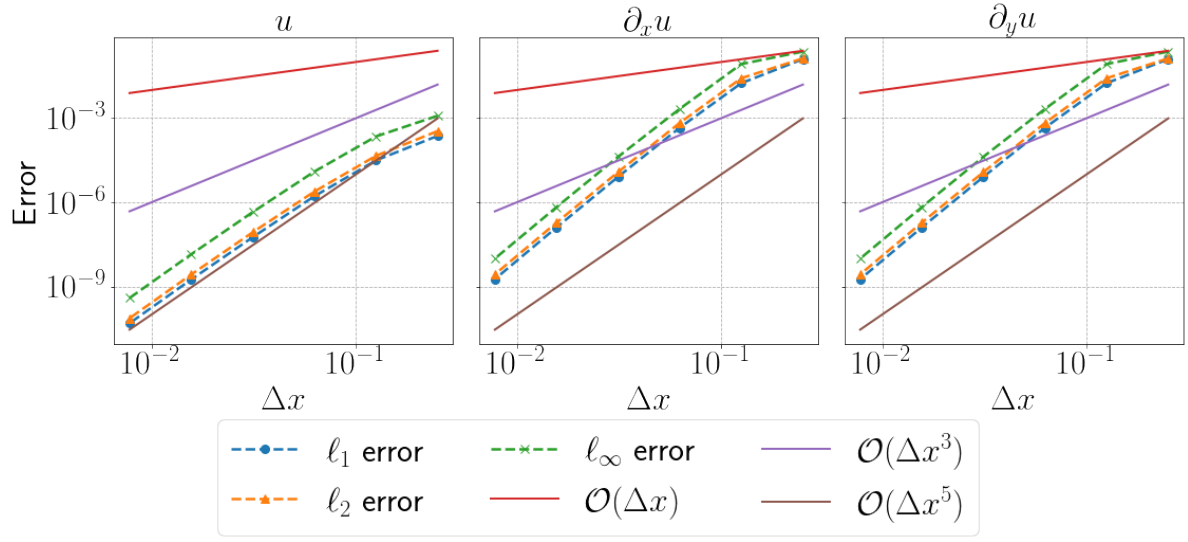
We solve the problem (92) using the two-dimensional domain $[-2, 2] \times [-2, 2]$ and use the initial data

$$u(x, y, 0) = e^{-16(x^2+y^2)}, \quad \partial_t u(x, y, 0) = 0, \quad (93)$$

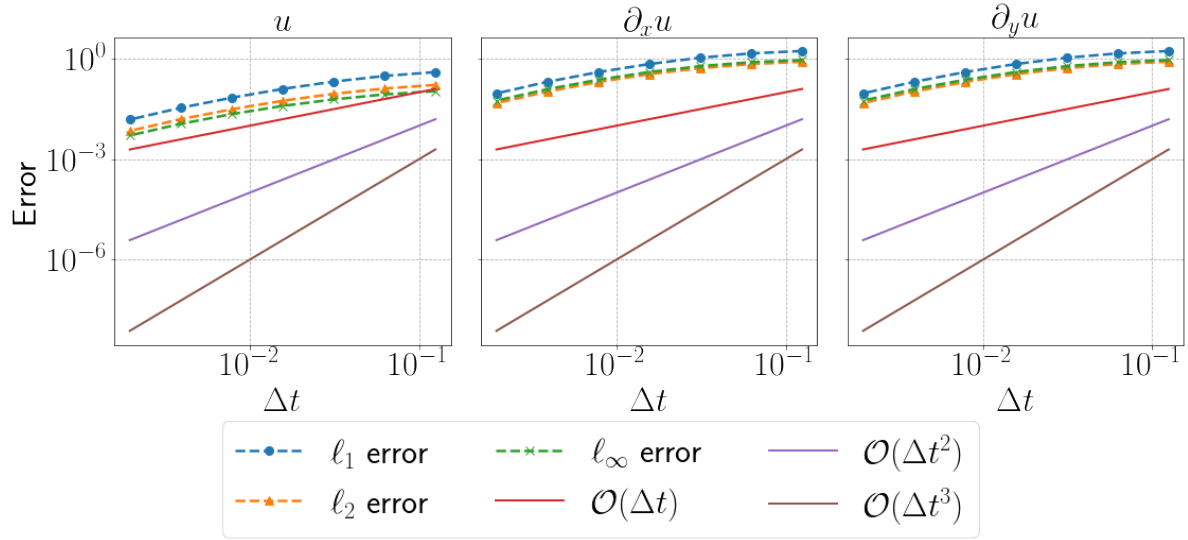
which is a Gaussian centered at the origin. Note that the width of the Gaussian is chosen so that the data is essentially machine zero at points along the boundary. If the initial data is not zero outside of the domain, then a specialized approach for initializing the boundary coefficients in the temporal recursion for outflow is required. This is not the case for this problem, so we can initialize the recursion for the boundary coefficients with zeroes.

The spatial refinement study was performed by varying the number of mesh points in each direction from 17 points to 513 points. The methods were applied for only 1 time step with step size of $\Delta t = 1 \times 10^{-4}$ and the errors were measured against a reference solution computed on a 2049×2049 spatial mesh using $\Delta t = 1 \times 10^{-4}$, here, as well. The refinement plots in Figure 3 show that each of these methods is approximately fifth-order in space.

In the refinement study for time, we evolve the solution on a fixed 512×512 mesh until the final time $T = 1.0$, which is before the wave leaves the domain. The number of time steps are successively doubled from $N_t = 8$ until $N_t = 512$. We note that the coarsest time discretization gives a $\text{CFL} \approx 16$, which is much larger than we would typically use for the first-order scheme. The reference solution is obtained with the same spatial mesh with a total of $N_t = 2048$ time steps. The methods for the solution and the



(a)



(b)

Figure 3: Space-time refinement of the solution and its spatial derivatives for the two-dimensional outflow problem 5.1.3 obtained with the first-order BDF method.

| Parameter | Value |
|--|-------------------------------------|
| Ion mass (m_i) [kg] | $9.108379025973462 \times 10^{-29}$ |
| Electron mass (m_e) [kg] | $9.108379025973462 \times 10^{-31}$ |
| Boltzmann constant (k_B) [$\text{kg m}^2 \text{s}^{-2} \text{K}^{-1}$] | $1.38064852 \times 10^{-23}$ |
| Permittivity of free space (ϵ_0) [$\text{kg}^{-1} \text{m}^{-3} \text{s}^4 \text{A}^2$] | $8.854187817 \times 10^{-12}$ |
| Permittivity of free space (μ_0) [$\text{kg m s}^{-2} \text{A}^{-2}$] | $1.25663706 \times 10^{-6}$ |
| Speed of light (c) [m/s] | 2.99792458×10^8 |

Table 1: Table of the physical constants, given in SI units, used in the numerical experiments.

corresponding derivatives refine to first-order accuracy in time, with the overall error in these methods being notably larger than for the periodic and Dirichlet test problems. One reason for this is that periodic and Dirichlet conditions can be enforced exactly, while outflow conditions are only approximately enforced. This error is further amplified in the case of the derivatives which introduce an additional factor that is roughly $\mathcal{O}(1/\Delta t)$ and increases the overall size of the error.

5.2 Plasma Test Problems

In this section, we present numerical results that demonstrate the performance of the proposed methods for fields in PIC applications. The PIC method we use implements standard conservative charge weighting for electrostatic problems and conservative current weighting [22] for electromagnetic problems in 2D. The electrostatic problems use FFT to solve Poisson’s equation, while the electromagnetic problems use the staggered Yee grid [20]. First, we test the particle methods and test the formulation with a single particle moving through known fields. We then focus on applying the methods to problems involving fields that respond to the motion of the particles. This includes the well-known two-stream instability as well as more challenging beam problems which can be used to demonstrate divergence cleaning techniques. We use the physical constants listed in Table 1 in the plasma test problems presented in this work.

5.2.1 Motion of a Single Charged Particle

We first compare the time integration methods for non-separable Hamiltonians with the well-known Boris method [6]. This is a natural first step before applying the method to problems with dynamic “self-fields” that respond to particle motion. Here, we consider a simple model for the motion of a single charged particle that is given by

$$\begin{aligned}\dot{\mathbf{x}} &= \mathbf{v}, \\ \dot{\mathbf{v}} &= \frac{q}{m} (\mathbf{E} + \mathbf{v} \times \mathbf{B}).\end{aligned}$$

We use electro- and magneto-static fields here and suppose that the magnetic field lies along the $\hat{\mathbf{z}}$ unit vector

$$\mathbf{B} = B_0 \hat{\mathbf{z}}, \quad \mathbf{E} = E^{(1)} \hat{\mathbf{x}} + E^{(y)} \hat{\mathbf{y}} + E^{(z)} \hat{\mathbf{z}},$$

where B_0 is a constant. Again, component-based definitions have been used for the fields $\mathbf{E} = (E^{(1)}, E^{(2)}, E^{(3)})$ and $\mathbf{B} = (B^{(1)}, B^{(2)}, B^{(3)})$. Consequently, we have that

$$\mathbf{v} \times \mathbf{B} = v^{(2)} B_0 \hat{\mathbf{x}} - v^{(1)} B_0 \hat{\mathbf{y}},$$

so the full equations of motion are

$$\begin{aligned}\frac{dx^{(1)}}{dt} &= v^{(1)}, & \frac{dv^{(1)}}{dt} &= \frac{q}{m} \left(E^{(1)} + v^{(2)} B_0 \right), \\ \frac{dx^{(2)}}{dt} &= v^{(2)}, & \frac{dv^{(2)}}{dt} &= \frac{q}{m} \left(E^{(2)} - v^{(1)} B_0 \right), \\ \frac{dx^{(3)}}{dt} &= v^{(3)}, & \frac{dv^{(3)}}{dt} &= \frac{q}{m} E^{(3)}.\end{aligned}$$

We can then use the classical momentum $\mathbf{p} = m\mathbf{v}$ to obtain

$$\begin{aligned}\frac{dx^{(1)}}{dt} &= \frac{1}{m} p^{(1)}, & \frac{dp^{(1)}}{dt} &= q \left(E^{(1)} + \frac{1}{m} p^{(2)} B_0 \right), \\ \frac{dx^{(2)}}{dt} &= \frac{1}{m} p^{(2)}, & \frac{dp^{(2)}}{dt} &= q \left(E^{(2)} - \frac{1}{m} p^{(1)} B_0 \right), \\ \frac{dx^{(3)}}{dt} &= \frac{1}{m} p^{(3)}, & \frac{dp^{(3)}}{dt} &= q E^{(3)}.\end{aligned}$$

Next, we show how to convert the electric and magnetic fields to potentials for the generalized momentum formulation.

Using the potentials ψ and $\mathbf{A} \equiv (A^{(1)}, A^{(2)}, A^{(3)})$, one can compute the electric and magnetic fields via (11), which is equivalent to writing

$$\begin{aligned}E^{(1)} &= -\partial_x \psi - \partial_t A^{(1)}, & B^{(1)} &= \partial_y A^{(3)} - \partial_z A^{(2)}, \\ E^{(2)} &= -\partial_y \psi - \partial_t A^{(2)}, & B^{(2)} &= -\partial_x A^{(3)} + \partial_z A^{(1)}, \\ E^{(3)} &= -\partial_z \psi - \partial_t A^{(3)}, & B^{(3)} &= \partial_x A^{(2)} - \partial_y A^{(1)}.\end{aligned}$$

The time-independence of the magnetic field for this problem implies that $\partial_t \mathbf{A} = 0$, so that

$$\mathbf{E} = -\nabla \psi \implies E^{(1)} = -\partial_x \psi, \quad E^{(2)} = -\partial_y \psi, \quad E^{(3)} = -\partial_z \psi.$$

Therefore, for this problem, we can use

$$\psi = -E^{(1)}x - E^{(2)}y - E^{(3)}z.$$

Moreover, since the magnetic field lives only in the z-direction, then this implies that the vector potential can be written as

$$\mathbf{B} = (0, 0, B_0) = (0, 0, \partial_x A^{(2)} - \partial_y A^{(1)})$$

As the choice of functions for gauges are not unique, it suffices to pick

$$A^{(1)} \equiv 0, \quad A^{(2)} = B_0 x, \quad A^{(3)} \equiv 0.$$

In summary, the values and required derivatives for the potentials are given by

$$\begin{aligned}-\partial_x \psi &= E^{(1)}, & -\partial_y \psi &= E^{(2)}, & -\partial_z \psi &= E^{(3)}, \\ A^{(1)} &= 0, & A^{(2)} &= B_0 x, & A^{(3)} &= 0, \\ \partial_x A^{(1)} &= 0, & \partial_y A^{(1)} &= 0, & \partial_z A^{(1)} &= 0, \\ \partial_x A^{(2)} &= B_0, & \partial_y A^{(2)} &= 0, & \partial_z A^{(2)} &= 0, \\ \partial_x A^{(3)} &= 0, & \partial_y A^{(3)} &= 0, & \partial_z A^{(3)} &= 0,\end{aligned}$$

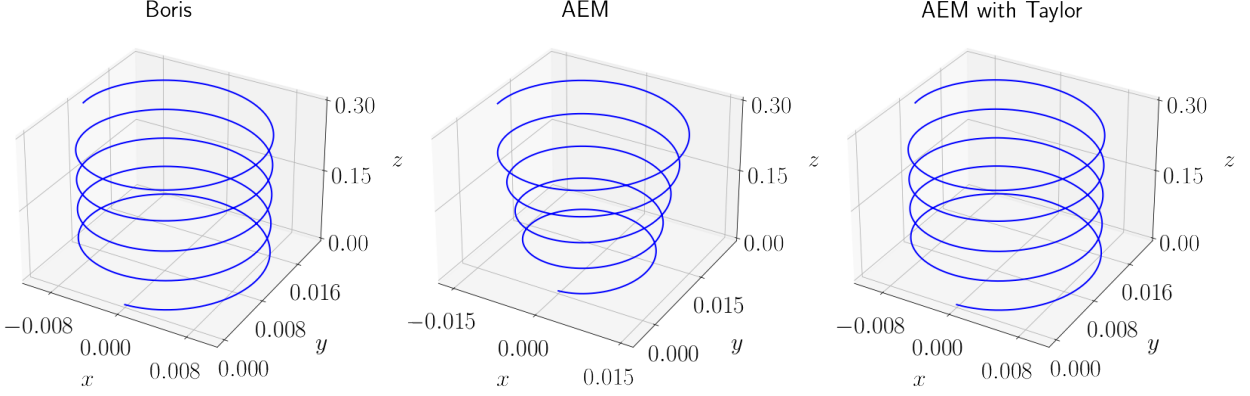


Figure 4: Trajectories for the single particle test, which are obtained using the Boris method [6], AEM [50], and the IAEM that uses a Taylor correction. The particles rotate about the magnetic field which points in the z -direction.

which results in the simplified equations of motion

$$\begin{aligned} \frac{dx^{(1)}}{dt} &= \frac{1}{m} P^{(1)}, & \frac{dP^{(1)}}{dt} &= qE^{(1)} + \frac{q}{m} \left[B_0 \left(P^{(2)} - qB_0 x^{(1)} \right) \right], \\ \frac{dx^{(2)}}{dt} &= \frac{1}{m} \left(P^{(2)} - qB_0 x^{(1)} \right), & \frac{dP^{(2)}}{dt} &= qE^{(2)}, \\ \frac{dx^{(3)}}{dt} &= \frac{1}{m} P^{(3)}, & \frac{dP^{(3)}}{dt} &= qE^{(3)}. \end{aligned}$$

The setup for the test consists of a single particle with mass $m = 1.0$ and charge $q = -1.0$ whose initial position is at the origin of the domain $\mathbf{x}(0) = (0, 0, 0)$. Initially, the particles have momentum components only in the x and z directions so as to generate so called “cyclotron” motion. We choose the initial momenta to be $\mathbf{p}(0) = \mathbf{P}(0) = (1.0 \times 10^{-2}, 0, 1.0 \times 10^{-2})$. The strength of the magnetic field in the z direction is selected to be $B_0 = 1.0$, and we ignore the contributions from the electric field, so that $\mathbf{E} = (0, 0, 0)$. Both methods are run to a final time of $T = 30.0$ and a total of 1000 time steps are used so that $\Delta t = 0.03$. The position of the particle is tracked through time and plotted as a curve in 3-D. In Figure 4, we compare the particle trajectories obtained with each of the methods. We note that the gyroradius for the AEM increases over time because the method is not volume-preserving. Over time, this causes the total energy to increase. In contrast, we see that the correction used in the IAEM reduces this behavior; however, the correction does not completely eliminate this behavior in the case of longer simulations as the truncation errors accumulate over time.

Next, we perform a refinement study of the methods to examine their error properties using the same experimental parameters from the cyclotron test. We measure the errors with the ℓ_∞ norm using a reference solution computed with 10^6 time steps, so that $\Delta t = 3.0 \times 10^{-5}$. The test successively doubles the number of steps, starting with 100 steps and uses, at most, 1.28×10^4 steps. The results of the refinement study are shown in Figure 5. Interestingly, both the base and improved versions of the AEM refine to first-order accuracy, we see that the Taylor correction decreases the error in the base method by roughly an order of magnitude. For coarser time step sizes, the improved method has errors that are (in some sense) comparable to the Boris method which is second-order accurate. Of course, the second-order method will outperform both versions of the AEM as the time step decreases.

5.2.2 The Cold Two-stream Instability

We consider the motion of “cold” streams electrons restricted to a one-dimensional periodic domain by a sufficiently strong (uniform) magnetic field in the two remaining directions. Ions are taken to be uniformly

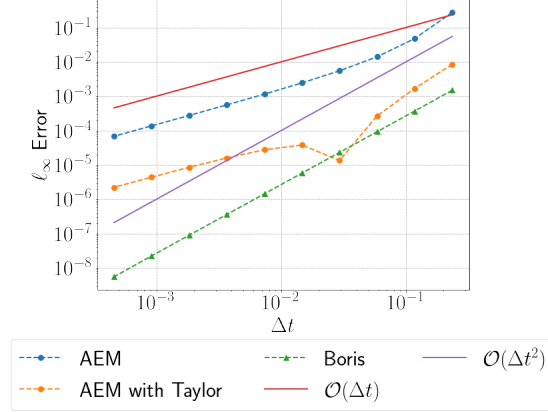


Figure 5: Refinement study for the trajectory of a single particle obtained using the Boris method [6], AEM [50], and an “improved” AEM that uses a Taylor correction. Errors are measured against a reference solution obtained using the Boris method. Even though the AEM with the Taylor correction is first-order accurate, the improvement is quite apparent (roughly an order of magnitude).

distributed in space and sufficiently heavy compared to the electrons so that their motion can be ignored in the simulation. The ions, which remain stationary, act as a neutralizing background against the dynamic electrons. The electron velocities are represented as a sum of two Dirac delta distributions that are symmetric in velocity space:

$$f(v) = \delta(v - v_b) + \delta(v + v_b).$$

The stream velocity $v_b > 0$ is set according to a drift velocity whose value ultimately controls the interaction of the streams. A slight perturbation in the electron velocities is then introduced to force a charge imbalance, which generates an electric field that attempts to restore the neutrality of the system. This causes the streams to interact or “roll-up”, corresponding to regions of trapped particles.

In order to describe the models used in the simulation, let us denote the components of the position and momentum vectors for particle i as $\mathbf{x}_i \equiv (x_i^{(1)}, x_i^{(2)}, x_i^{(3)})$ and $\mathbf{P}_i \equiv (P_i^{(1)}, P_i^{(2)}, P_i^{(3)})$, respectively, the equations for the motion of particle i assume the form

$$\begin{aligned} \frac{dx_i^{(1)}}{dt} &= \frac{1}{m_i} P_i^{(1)}, \\ \frac{dP_i^{(1)}}{dt} &= -q_i \partial_x \psi. \end{aligned}$$

Therefore, the motion in this plane requires knowledge of ψ , $\partial_x \psi$, which can be obtained by solving a two-way wave equation for the scalar potential:

$$\frac{1}{c^2} \frac{\partial^2 \psi}{\partial t^2} - \Delta \psi = \frac{1}{\epsilon_0} \rho. \quad (94)$$

As this is an electrostatic problem, the gauge condition can be safely ignored. In the limit where the characteristic thermal velocity V of the particles become well-separated from the speed of light c , so that $\kappa = c/V \gg 1$, one instead solves the Poisson equation

$$-\Delta \psi = \frac{1}{\epsilon_0} \rho. \quad (95)$$

Using asymptotic analysis, it can be shown that the approximation error made by using the Poisson model for the scalar potential is $\mathcal{O}(1/\kappa)$ [71].

We establish the efficacy of the proposed algorithms for time stepping particles and evolving fields by comparing with well-known methods. The setup for this test problem consists of a non-dimensional spatial

| Parameter | Value |
|---|---------------------------|
| Average number density (\bar{n}) [m^{-3}] | 7.856060×10^1 |
| Average temperature (\bar{T}) [K] | 2.371698×10^6 |
| Debye length (λ_D) [m] | 1.199170×10^4 |
| Inverse angular plasma frequency (ω_{pe}^{-1}) [s/rad] | 2.000000×10^{-3} |
| Thermal velocity (v_{th}) [m/s] | 5.995849×10^6 |

Table 2: Table of the plasma parameters used in the two-stream instability example.

mesh defined on the interval $[-10\pi/3, 10\pi/3]$, which is discretized using 128 total grid points and is supplied with periodic boundary conditions. The non-dimensional final time for the simulation is taken to be $T_f = 100.0$ with 4,000 time steps being used to evolve the system. The plasma is represented with a total of 30,000 macro-particles, consisting of 10,000 ions and 20,000 electrons. As mentioned earlier, the positions of the ions and electrons are taken to be uniformly spaced along the grid. Ions remain stationary in the problem so we set their velocity to zero. The construction of the streams begins by first splitting the electrons into two equally sized groups, whose respective (non-dimensional) drift velocities are set to be ± 1 . To generate an instability we add a perturbation to the electron velocities of the form

$$\epsilon \sin\left(\frac{2\pi k(x-a)}{L_x}\right).$$

Here, $\epsilon = 5.0 \times 10^{-4}$ controls the strength of the perturbation, $k = 1$ is the wave number for the perturbation, x is the position of the particle (electron), a is the left-most grid point, and L_x is the length of the domain. In a more physically realistic simulation, the perturbation would be induced by some external force, which would also result in a perturbation of the position data for the particles. Such a perturbation of the position data requires a self-consistent field solve to properly initialize the potentials. In our simulation, we assume that no spatial perturbation is present, so that the problem the fields are identically zero at the initial time step. The plasma parameters used in the non-dimensionalization for this test problem, are displayed in Table 2. Note that in this configuration, the normalized speed of light $\kappa = 50$. In some sense, this value is close to the relativistic regime, but it remains sufficiently far away to avoid modifications to the particle integrator. Additionally, we find that this configuration adequately resolves the plasma Debye length (≈ 6 cells/ λ_D), angular plasma period (≈ 40 steps/ ω_{pe}^{-1}), and the particle CFL < 1 , which are all necessary for maintaining stability in explicit PIC methods.

We first assessed the behavior of the particle integrator by considering the Poisson model (95) for the scalar potential. The Taylor correction version of the AEM was not considered in this problem because the contributions from the magnetic field are ignored. Since the combination of leapfrog time integration with an FFT field solver is such a commonly used approach to this problem, it allowed us to identify key differences attributed solely to the choice of time integration method used for particles. We note that the particular initial condition for this problem lead to a special case in which the AEM is equivalent to leapfrog integration. Since the problem starts out as charge neutral, there is no electric field at time $t = 0$. This means that there is no modification to the particle velocities in the step that generates the staggering required by the leapfrog method. Of course, this is no longer true for problems which have an initial charge imbalance because the electric field would be non-zero. Plots that compare the evolution of the electron beams, obtained with both methods and an FFT field solver, are presented in Figure 6. As expected, we see that the AEM produces structures that are identical to those which are generated with the leapfrog scheme. Using basic linear response theory (see e.g., [72]) one obtains the dispersion relation for the cold problem as

$$\omega^4 - 2\omega^2 (\omega_{pe} + k^2 v_b^2) + k^2 v_b^2 (k^2 v_b^2 - 2\omega_{pe}) = 0.$$

While the dispersion relation for the warm problem can certainly be derived, it is more complicated than the cold problem, as it requires a bit of complex analysis and special functions [73]. Taking $v_b = 1$, $\omega_{pe} = 1$, and $k = 2\pi/L_x$ in the dispersion relation above, we identify a growth rate ≈ 0.2760 . In Figure 7, we compare the growth rate of the electric field in from both methods with the analytical growth rate. Again, we see identical results among both methods, which reproduce the correct growth rate.

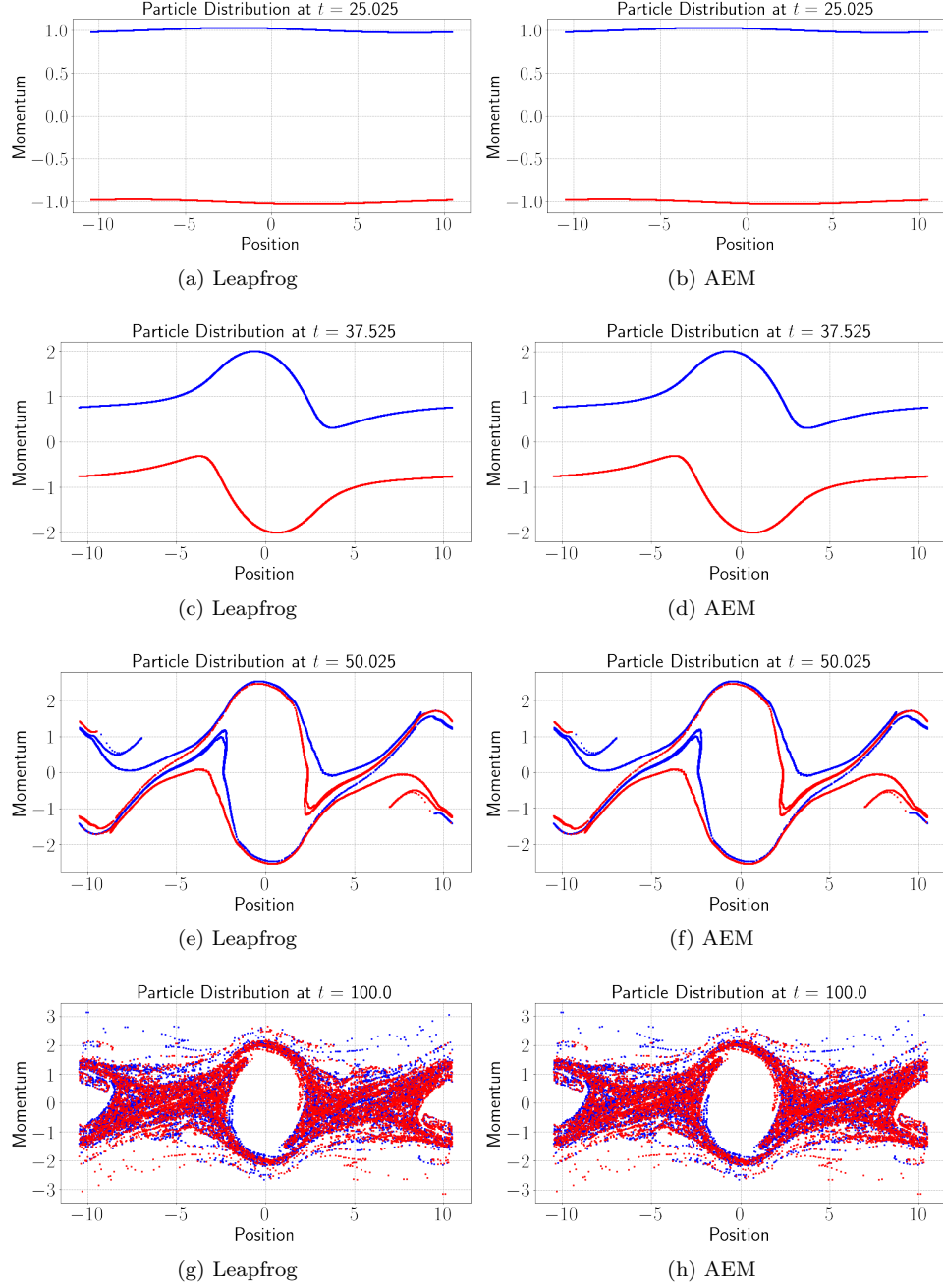


Figure 6: We present plots of the electrons in phase space obtained using the Poisson model for the two-stream instability problem. Results obtained using leapfrog time integration are shown in the left column, while the right column applies the AEM. The version of the AEM that applies the Taylor correction is not considered here because the contributions from the magnetic fields are ignored. The FFT is used to compute the scalar potentials (as well as its gradient). Identical results are observed with both approaches.

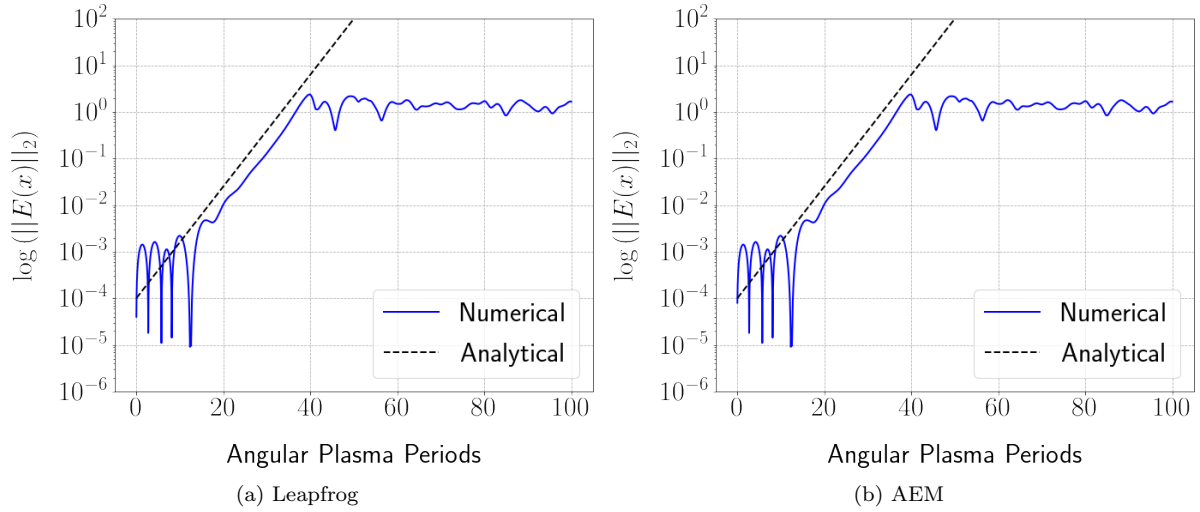


Figure 7: We plot the growth rate in the electric field for the Poisson model using both methods, which is compared against an analytical growth rate obtained from linear response theory. Using this experimental configuration, the analytical growth rate is determined to be ≈ 0.2760 . We can see that the AEM reproduces the growth rate of the leapfrog method.

The same experiment was repeated using a two-way wave model (94) in the place of the Poisson model (95) for the scalar potential. For strongly electrostatic problems (i.e., $\kappa \gg 1$), the wave model should produce results which are similar to those of the Poisson model shown in Figure 6. This feature allows us to benchmark the performance of the wave solver and proposed methods for derivatives by comparing against the elliptic model. The results for the two methods are displayed in Figure 8. We see that the early behavior is quite similar to the results in Figure 6 obtained with the elliptic model. At later times, however, the trapping regions are more “compressed” than those generated with the Poisson model. This is a likely consequence of the finite speed of propagation in the wave model, where the potential responds more slowly to an imbalance in charge. We can also check the growth rate in the electric field, as we did with the Poisson model. In this configuration, the Poisson equation is a good approximation of the wave equation for the potential, so we can use the growth rate presented above to access the validity of the method. The growth rates for the wave model are displayed in Figure 9, which show good agreement with the theory.

5.2.3 Numerical Heating

We now discuss the numerical heating study, which is used to characterize the effect of resolving the Debye length λ_D . These numerical properties turn out to be connected to the symplecticity of the method. Explicit PIC methods are not symplectic because the fields and the particles are not self-consistent with one another. Consequently, the grid should be sufficiently fine so that a given particle can “see” the correct potential that is otherwise screened by particles of opposite charge. In other words, with explicit PIC methods, one needs to resolve the charge separation in the plasma, whose characteristic length scale is according to the Debye length. A general rule of thumb for explicit PIC simulations is that the grid spacing Δx should satisfy $4\Delta x < \lambda_D$ to prevent substantial numerical heating. Otherwise, the temperature of the plasma increases in an attempt to set a “new” Debye length that is adequately resolved on the given mesh.

The setup for this problem is slightly different from the two-stream example discussed earlier. Here, we provide, as input, a Debye length λ_D and a normalized speed of light κ , which can be used to calculate the average number density \bar{n} and macroscopic temperature \bar{T} for the plasma. The remaining parameters can be derived from these values and are shown in Table 3. Here we consider both 1D-1V (1D-1P) electrostatic and 2D-2V (2D-2P) electromagnetic configurations that consist of ions and electrons in a periodic domain. The spatial domain for the electrostatic case is $[-25, 25]$, while the electromagnetic case uses $[-25, 25]^2$. In

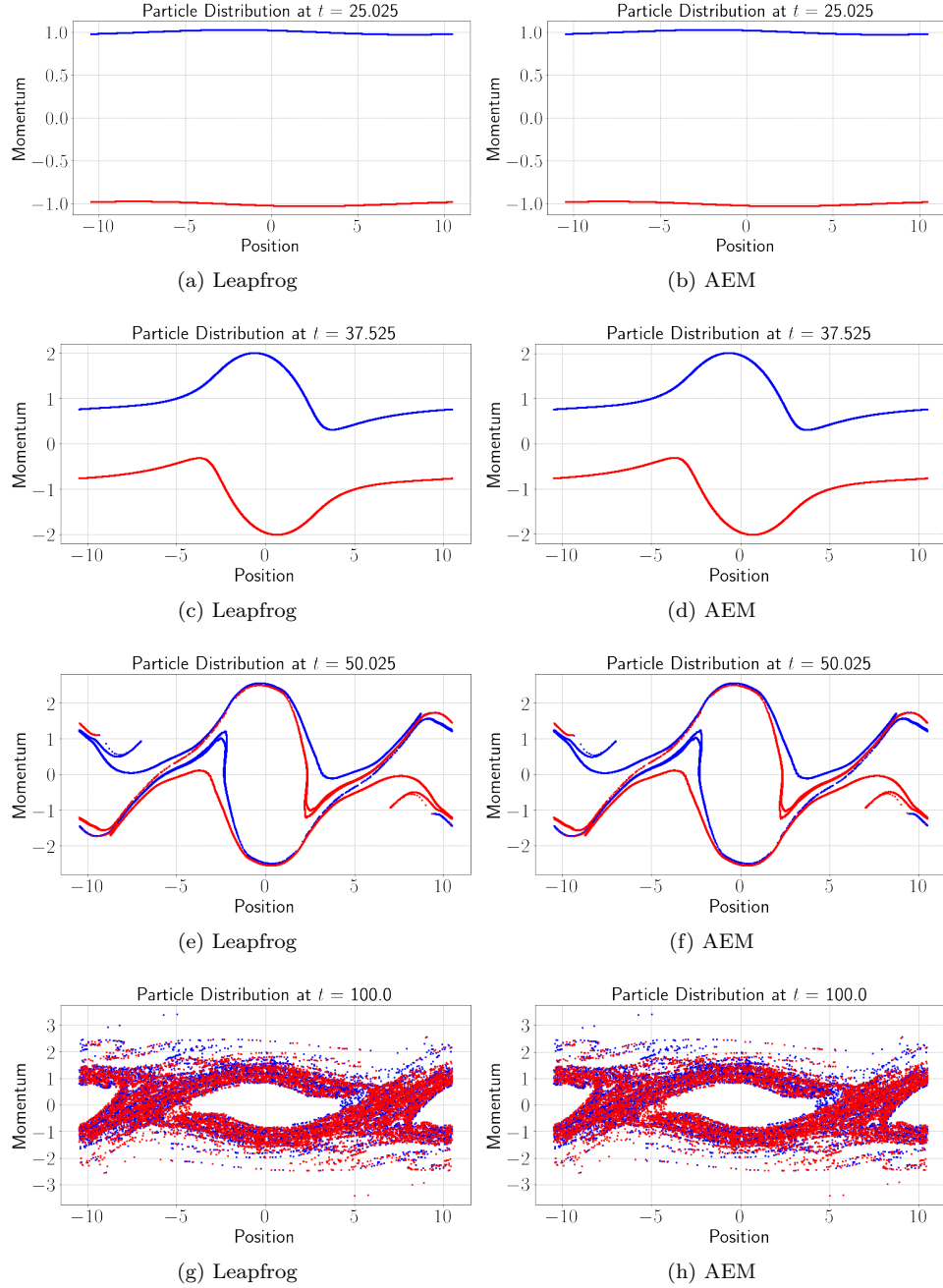


Figure 8: We present plots of the electrons in phase space obtained using the wave model for the two-stream example. Results obtained using leapfrog time integration are shown in the left column, while the right column applies the AEM. The first-order (diffusive) BDF scheme (BDF-1) is used to compute the scalar potentials and their derivatives in both approaches. Unlike the results obtained with the Poisson model, in which the FFT was used as the field solver (see Figure 6), we observe differences in the structure of the trapping regions. Such regions in the wave model appear to be more compressed than those in the elliptic model.

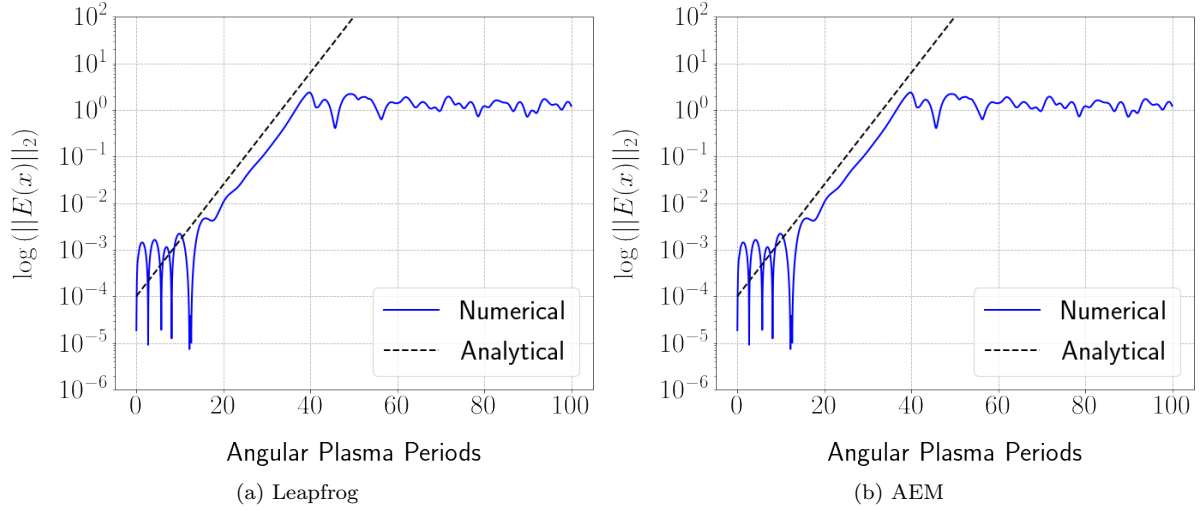


Figure 9: We plot the growth rate in the electric field obtained with both methods, which use the BDF-1 field solver to evolve the scalar potential and its derivatives. This data is compared against an analytical growth rate obtained from linear response theory for the Poisson model. Using this experimental configuration, the analytical growth rate is determined to be ≈ 0.2760 . We, again, see that the AEM reproduces the growth rate of the leapfrog method.

both cases, the spatial domain is refined by successively doubling the number of mesh points from 16 to 256 in each dimension. The simulations use 1×10^6 time steps with the non-dimensional final time $T_f = 1 \times 10^3$. In the 1D-1V electrostatic simulation, we use 5×10^3 particles for each species, and 2.5×10^5 for the 2D-2V electromagnetic simulation. As before, we assume that the ions remain stationary since they are heavier than the electrons. Electrons are given uniform positions in space and their velocities are initialized by sampling from the standard normal distribution. A drift velocity is not used in these tests. To ensure consistency across the runs, we also seed the random number generator prior to sampling.

We monitor heating during the simulations by computing the variance in the components of the electron velocities, since this is connected to the temperature of a Maxwellian distribution. In the 1D-1V case, the variance data at a given given time step is converted to a temperature using

$$\bar{T} = \frac{m_e}{k_B} \text{var}(v^{(1)}).$$

For the 2D-2V case, we compute the average of the variance for each component of the velocity, which is similarly converted to a temperature using

$$\bar{T} = \frac{m_e (\text{var}(v^{(1)}) + \text{var}(v^{(2)}))}{2k_B}.$$

We use the superscripts in the above metrics to refer to the individual velocity components across all of the particles. The factor of 2 is used to average the variance among these components.

The models used in the 1D-1V electrostatic tests are identical to the ones presented for the two-stream instability example, so we shall skip these details for brevity. In the case of the 2D-2V electromagnetic

| Parameter | Value |
|---|---------------------------|
| Average number density (\bar{n}) [m^{-3}] | 1.129708×10^{14} |
| Average temperature (\bar{T}) [K] | 2.371698×10^6 |
| Debye length (λ_D) [m] | 1.000000×10^{-2} |
| Inverse angular plasma frequency (ω_{pe}^{-1}) [s/rad] | 1.667820×10^{-9} |
| Thermal velocity (v_{th}) [m/s] | 5.995849×10^6 |

Table 3: Table of the plasma parameters used in the numerical heating examples.

experiment, the particle equations in the generalized momentum formulation are

$$\begin{aligned}
\frac{dx_i^{(1)}}{dt} &= \frac{1}{m_i} \left(P_i^{(1)} - q_i A^{(1)} \right), \\
\frac{dx_i^{(2)}}{dt} &= \frac{1}{m_i} \left(P_i^{(2)} - q_i A^{(2)} \right), \\
\frac{dP_i^{(1)}}{dt} &= -q_i \partial_x \psi + \frac{q_i}{m_i} \left[\left(\partial_x A^{(1)} \right) \left(P_i^{(1)} - q_i A^{(1)} \right) + \left(\partial_x A^{(2)} \right) \left(P_i^{(2)} - q_i A^{(2)} \right) \right], \\
\frac{dP_i^{(2)}}{dt} &= -q_i \partial_y \psi + \frac{q_i}{m_i} \left[\left(\partial_y A^{(1)} \right) \left(P_i^{(1)} - q_i A^{(1)} \right) + \left(\partial_y A^{(2)} \right) \left(P_i^{(2)} - q_i A^{(2)} \right) \right].
\end{aligned}$$

The contributions from the fields are obtained by solving a system of wave equations for the potentials, which take the form

$$\begin{aligned}
\frac{1}{c^2} \frac{\partial^2 \psi}{\partial t^2} - \Delta \psi &= \frac{1}{\epsilon_0} \rho, \\
\frac{1}{c^2} \frac{\partial^2 A^{(1)}}{\partial t^2} - \Delta A^{(1)} &= \mu_0 J^{(1)}, \\
\frac{1}{c^2} \frac{\partial^2 A^{(2)}}{\partial t^2} - \Delta A^{(2)} &= \mu_0 J^{(2)}.
\end{aligned}$$

To establish the heating properties of the proposed methods in an electromagnetic setting, an identical experiment is performed using a standard FDTD-PIC approach in which the equations of motion for the particles are expressed in terms of \mathbf{E} and \mathbf{B} . For this example, these equations take the form

$$\begin{aligned}
\frac{dx_i^{(1)}}{dt} &= v_i^{(1)}, & \frac{dv_i^{(1)}}{dt} &= \frac{q_i}{m_i} \left(E^{(1)} + v_i^{(2)} B^{(3)} \right), \\
\frac{dx_i^{(2)}}{dt} &= v_i^{(2)}, & \frac{dv_i^{(2)}}{dt} &= \frac{q_i}{m_i} \left(E^{(2)} - v_i^{(1)} B^{(3)} \right),
\end{aligned}$$

and are evolved in a leapfrog format through the Boris method [6]. Since we have restricted the system to two spatial dimensions, the curl equations decouple into the so-called Transverse Electric (TE) and Transverse Magnetic (TM) modes. Through no requirement of this particular problem, but for purposes of consistency with the expanding beam problem (see below), we retain the following TE mode curl equations for the fields:

$$\begin{aligned}
\frac{\partial E^{(2)}}{\partial x} - \frac{\partial E^{(1)}}{\partial y} &= -\frac{\partial B^{(3)}}{\partial t}, \\
-\frac{\partial B^{(2)}}{\partial z} &= \mu_0 J^{(1)} + \frac{1}{c^2} \frac{\partial E^{(1)}}{\partial t}, \\
-\frac{\partial B^{(3)}}{\partial x} &= \mu_0 J^{(2)} + \frac{1}{c^2} \frac{\partial E^{(2)}}{\partial t}.
\end{aligned}$$

The equations for the fields, which are evolved in an explicit manner, are discretized using a staggered Yee mesh (see Figure 10) [20].

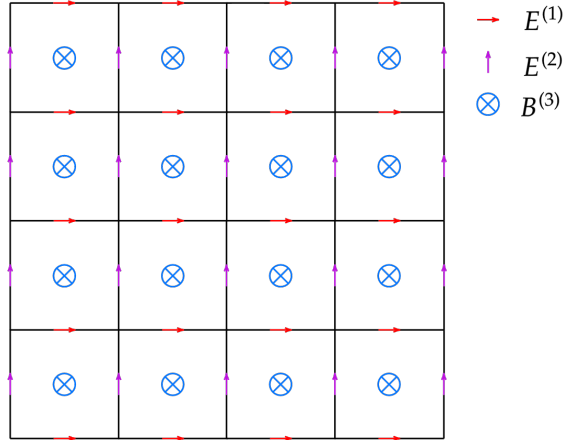


Figure 10: The staggered Yee grid in TE mode.

The results of our heating experiments can be found in Figures 11, 12 and 13. Figures 11 and 12 present the results for the 1D-1V electrostatic problem in which we consider both Poisson and wave equation models, respectively, for the scalar potential. Figure 13 shows the results for the 2D-2V electromagnetic heating experiment that compares the FDTD-PIC method and the IAEM. For the 1D-1V electrostatic experiments, we observe significant differences in the heating behavior due to the choice of models used for the scalar potential. In particular, comparing Figures 11 and 12, we can clearly see the rate of heating is far more significant when the Poisson model is used instead of the wave equation. This is partly due to the finite speed of propagation offered by the wave model, which causes the potential to respond more slowly to variations in the charge density ρ . We find this to be true even in cases where the Debye length would normally be considered underresolved by practitioners, resulting in far less severe fluctuations in temperature. Similar behaviors are also observed in the more complicated 2D-2V electromagnetic experiment. We note that the benchmark FDTD-PIC approach displays significant fluctuations in the temperature even in cases where the grid resolves the Debye length. In contrast, the proposed methods show notably smaller temperature fluctuations across the grid configurations, over many plasma periods. This suggests that it may be possible to use a much coarser grid than what is generally permitted by explicit particle methods, resulting in more efficient calculations. In simulations on bounded domains, particles may not be present in the domain long enough to see any noticeable effects of heating, as they could be removed via an absorption mechanism or a particle collector. The potential efficiency of the proposed method in solving such problems will also be the subject of future work.

5.2.4 The Bennett Equilibrium Pinch

We consider the Bennett Equilibrium pinch, named after its discoverer W. H. Bennett who first analyzed the problem [74]. In this paper, Bennett constructed a steady-state solution for the ideal MHD equations using a cylindrical coordinate system. Electrons are modeled as a fluid that drifts along the z -direction, creating currents that generate magnetic fields with x and y components that confine or “squeeze” the plasma towards the axis of the cylinder. To create a proper equilibrium balance, the electron fluid velocity along the axis of the cylinder is carefully in such a way that the forces generated by the plasma are equal and opposite to those of the confining magnetic field that surrounds it.

Our particle simulation of the Bennett pinch closely follows the description provided in chapter 13 of Bittencourt [75]. We consider the motion of electrons inside a cross-section of a cylindrical column of plasma whose radius is R_b and suppose that the axis of the beam is centered at the origin of a bounding box specified by the intervals $[-2R_b, 2R_b] \times [-2R_b, 2R_b]$. Let $\mathbf{J} = (J^{(1)}, J^{(2)}, J^{(3)})$ denote the components of the current density. In the x - y plane, the particles are sampled from a Maxwellian distribution, so we ignore

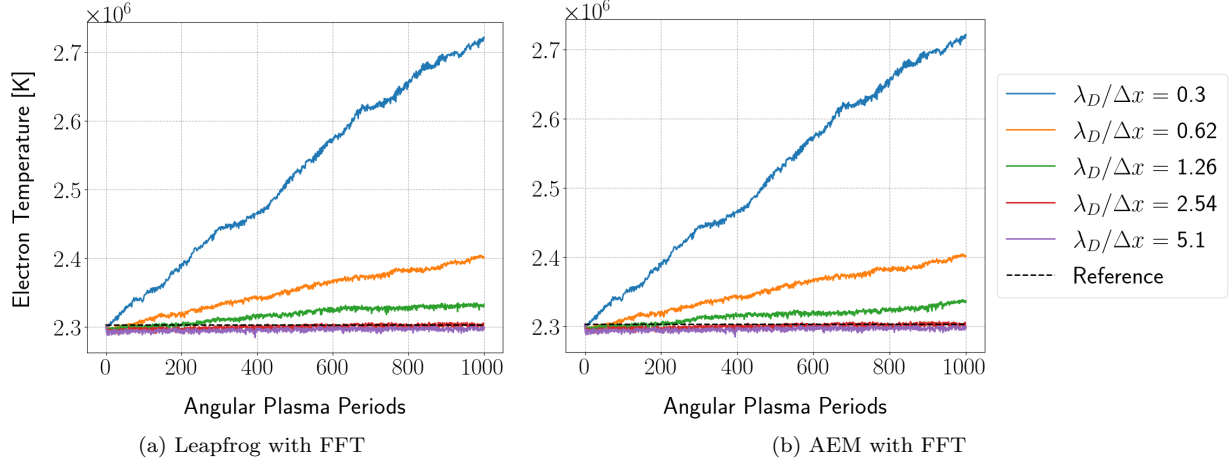


Figure 11: We present results from the 1D-1V electrostatic heating tests with a Poisson model for the potential. We plot the average electron temperature as a function of the number of angular plasma periods. On the left, we show the results obtained with the standard leapfrog time integration scheme, while the plot on the right uses the base AEM [50]. Since the magnetic field is ignored in the model, the AEM and its improved version are identical. Additionally, the since the problem is charge neutral, the results for the two methods will be identical. Fields and their derivatives are constructed using a FFT field solver. The results suggest that heating can be prevented if we use ≈ 2.54 grid cells per plasma Debye length. This is quite close to the usual rule of thumb which recommends roughly 4 cells per Debye length.

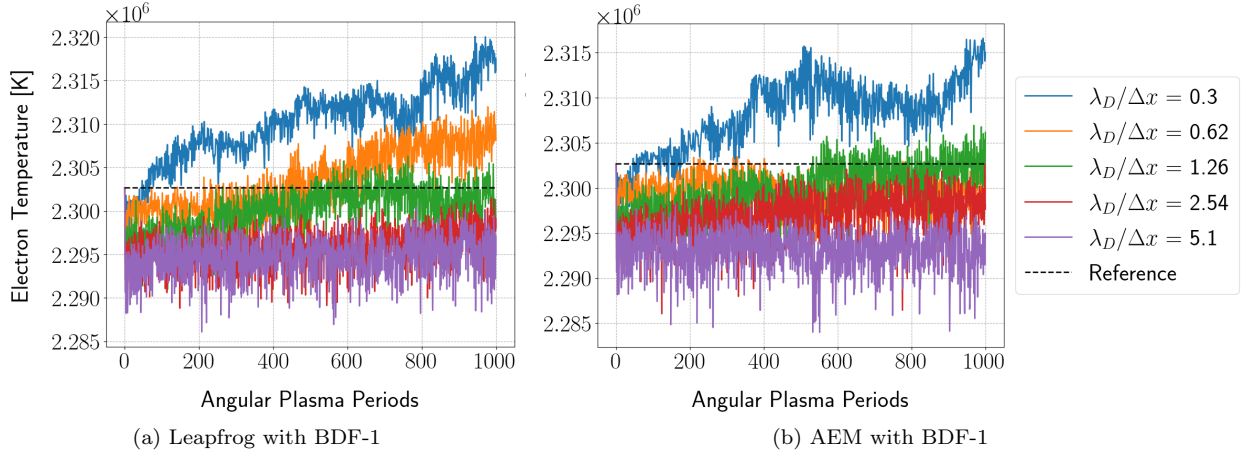


Figure 12: We present results from the 1D-1V electrostatic heating tests with a wave model for the potential. We plot the average electron temperature as a function of the number of angular plasma periods. On the left, we show the results obtained with the standard leapfrog time integration scheme, while the plot on the right uses the base AEM [50]. Since the magnetic field is ignored in the model, the AEM and its improved version are identical. Additionally, the since the problem is charge neutral, the results for the two methods will be identical. Fields and their derivatives are constructed using the proposed BDF-1 field solver. In contrast to the results obtained with the Poisson model (see Figure 11) we observe less severe fluctuations in temperature due to the finite speed of propagation in the wave model. Furthermore, the temperature fluctuations are not severe even in grid configurations which are less adequate at resolving the Debye length.

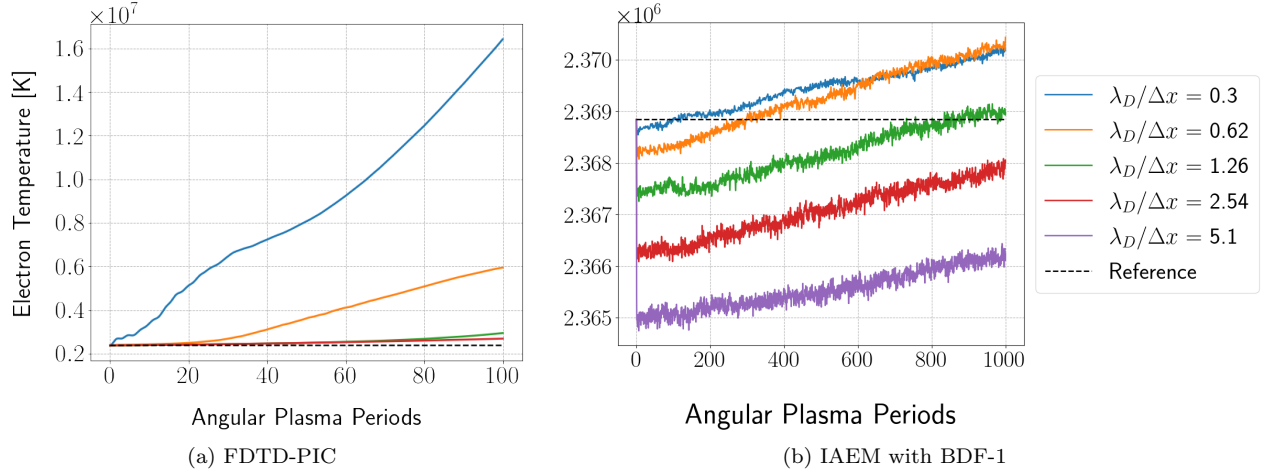


Figure 13: We present results from the 2D-2V electromagnetic heating experiments that plot the average electron temperature as a function of the number of angular plasma periods. The plot on the left was obtained with the FDTD-PIC method, while the plot on the right uses the IAEM and the proposed BDF-1 field solver. Since the IAEM is not symplectic, it will, over time, generate additional sources of energy causing the simulation to heat even if the plasma Debye length is sufficiently resolved; however, the results indicate that fluctuations in the temperature are not substantial, even in cases where the Debye length would normally be considered underresolved by the mesh. In contrast, the FDTD-PIC method displays more significant fluctuations over a smaller time window, even when the Debye length is resolved by the mesh.

the contributions from $J^{(1)}$ and $J^{(2)}$ because they will have a net-zero current. Since the particles drift along the axis of the beam, we retain the third component of the current density $J^{(3)}$. Consequently, we choose to retain only $A^{(3)}$ and ignore the wave equations for $A^{(1)}$ and $A^{(2)}$. Ions are spatially distributed by sampling the same distribution as the electrons and are assumed to be stationary within the cross-section, since their mass is taken to be much larger than the electrons. If we denote the components of the position and momentum vectors for particle i as $\mathbf{x}_i \equiv (x_i^{(1)}, x_i^{(2)}, x_i^{(3)})$ and $\mathbf{P}_i \equiv (P_i^{(1)}, P_i^{(2)}, P_i^{(3)})$, respectively, the equations for the motion of each particle assume the form

$$\begin{aligned} \frac{dx_i^{(1)}}{dt} &= \frac{1}{m_i} P_i^{(1)}, & \frac{dP_i^{(1)}}{dt} &= -q_i \partial_x \psi + \frac{q_i}{m_i} \left(\partial_x A^{(3)} \right) \left(P_i^{(3)} - q_i A^{(3)} \right), \\ \frac{dx_i^{(2)}}{dt} &= \frac{1}{m_i} P_i^{(2)}, & \frac{dP_i^{(2)}}{dt} &= -q_i \partial_y \psi + \frac{q_i}{m_i} \left(\partial_y A^{(3)} \right) \left(P_i^{(3)} - q_i A^{(3)} \right). \end{aligned}$$

Note that while we retain the last component of the momentum, we do not include an equation for $P_i^{(3)}$, since each term involves z -derivatives which are ignored. Additionally, we do not update $v^{(3)}$ in the implementation of the IAEM for this problem. Otherwise, slight changes in the velocity inevitably create new currents that change the steady-state fields. It is this behavior which permits the types instabilities encountered in more “dynamic” pinching problems, which will be investigated at a later time.

The particle equations of motion for this problem can also be formulated in terms of \mathbf{E} and \mathbf{B} and solved with the Boris method [6]. Given the potentials ψ and \mathbf{A} , we can calculate the \mathbf{E} and \mathbf{B} fields using (11):

$$\mathbf{E} = -\nabla \psi - \partial_t \mathbf{A}, \quad \mathbf{B} = \nabla \times \mathbf{A}.$$

| Parameter | Value |
|--|----------------------------|
| Beam radius (R_b) [m] | 1.0×10^{-6} |
| Average number density (\bar{n}) [m ⁻³] | 4.391989×10^{19} |
| Average temperature (\bar{T}) [K] | 5.929245×10^1 |
| Debye length (λ_D) [m] | 8.019042×10^{-8} |
| Inverse angular plasma frequency (ω_{pe}^{-1}) [s/rad] | 2.674864×10^{-12} |
| Thermal velocity (v_{th}) [m/s] | 2.997925×10^4 |
| Electron drift velocity (v_{drift}) [m/s] | 2.997925×10^7 |
| Fraction of particles contained in the beam (α) [non-dimensional] | 0.99 |

Table 4: Table of the parameters used in the setup for the Bennett pinch problem.

The particles are then evolved according to

$$\begin{aligned}\frac{dx_i^{(1)}}{dt} &= v_i^{(1)}, & \frac{dv_i^{(1)}}{dt} &= \frac{q_i}{m_i} \left(E^{(1)} - v_i^{(3)} B^{(2)} \right), \\ \frac{dx_i^{(2)}}{dt} &= v_i^{(2)}, & \frac{dv_i^{(2)}}{dt} &= \frac{q_i}{m_i} \left(E^{(2)} + v_i^{(3)} B^{(1)} \right).\end{aligned}$$

To be consistent with the generalized momentum formulation of the problem, we have neglected the equation for $v_i^{(3)}$. We remark that contributions in $E^{(3)}$ are negligible since $\partial_z \psi = 0$ and $\partial_t A^{(3)} = 0$ in the true problem.

Particles that leave the domain due to inadequate confinement by the fields can be prescribed new positions by sampling the initial distribution, which essentially re-injects them into the beam. The velocity and momenta are left unchanged in an effort to keep the total current density constant. Next, we provide the experimental parameters for the simulations along with details regarding the initialization procedure for the problem.

During the initialization and time evolution phases of the simulation, we use an analytical solution for the toroidal magnetic field to verify the correctness of the numerical fields, which maintain the steady-state. To derive the analytical solution for the toroidal magnetic field $B^{(\theta)}$, we solve the differential equation (equation 13.3.5 in [75])

$$\frac{d}{dr} \left(r B^{(\theta)} \right) = \mu_0 q_e v_e^{(3)} r n(r),$$

where μ_0 is the permeability of free space, q_e is the electron charge, $v_e^{(3)}$ is the z -component of the electron velocity, and $n(r)$ is the *Bennett distribution* for the electrons (equation 13.3.8 in [75]) given as

$$n(r) = \frac{n_0}{(1 + n_0 b r^2)^2}. \quad (96)$$

The on-axis number density n_0 is calculated according to equation 13.3.14 of [75]

$$n_0 = \frac{1}{b R_b^2} \left(\frac{\alpha}{1 - \alpha} \right),$$

where $\alpha \in [0, 1)$ is a parameter the fraction of particles in the cross-section contained within the beam. We use the constant b , whose form is given in equation 13.3.9 of [75], namely

$$b = \frac{\mu_0 \left(q_e v_e^{(3)} \right)^2}{8 k_B \bar{T}}.$$

Note that the above expression is equivalent to assuming that the ions are cold so that $T_i = 0$ and $T_e = \bar{T}$. Solving the differential equation above gives the analytical toroidal magnetic field

$$B^{(\theta)}(r) = \frac{\mu_0 q_e v_e^{(3)}}{2} \frac{n_0 r}{1 + n_0 b r^2}. \quad (97)$$

Numerically, we solve the problem in a Cartesian coordinate system, instead of a cylindrical coordinate system. Therefore, we will have to convert $B^{(1)} \equiv B^{(x)}$ and $B^{(2)} \equiv B^{(y)}$ to $B^{(\theta)}$. The required transformation that converts between these coordinate systems is

$$\begin{bmatrix} B^{(r)} \\ B^{(\theta)} \\ B^{(z)} \end{bmatrix} = \begin{bmatrix} \cos(\theta) & \sin(\theta) & 0 \\ -\sin(\theta) & \cos(\theta) & 0 \\ 0 & 0 & 1 \end{bmatrix} \begin{bmatrix} B^{(x)} \\ B^{(y)} \\ B^{(z)} \end{bmatrix},$$

Note that this transformation can be further simplified with $\cos(\theta) = \frac{x}{r}$ and $\sin(\theta) = \frac{y}{r}$, with $r > 0$, so that we obtain for the θ -component

$$B^{(\theta)}(r) = -\frac{y}{r}B^{(x)} + \frac{x}{r}B^{(y)}, \quad r = \sqrt{x^2 + y^2} > 0.$$

For the case of $r = 0$, we can appeal to the analytical solution (97), so that $B^{(\theta)}(0) = 0$.

The setup of our PIC simulation requires an average or macroscopic number density \bar{n} . This can be obtained from a variation of equation 13.3.11 in [75] to obtain

$$\bar{n} = \frac{2\pi}{16R_b^2} \int_0^{R_b} n(r)r \, dr = \frac{n_0\pi R_b^2}{16R_b^2(1 + n_0bR_b^2)}, \quad (98)$$

where we have used the definition (96). A summary of the plasma parameters used in the simulation of the Bennett pinch is presented in Table 4.

Next, we describe the initialization procedure for the fields ψ and \mathbf{A} that recovers the steady-state solution with enough accuracy to achieve particle confinement. This problem is defined over free-space, so we prescribe outflow boundary conditions along the boundary of the box that encloses the beam. To initialize the steady-state with the wave solvers, we first set $\psi = 0$ and $\mathbf{A} = 0$, and step the corresponding wave equations to steady-state, while holding the sources ρ and \mathbf{J} fixed. Although it is more expensive than direct evaluation of the free-space integral solution, this technique allows for a self-consistent initialization of the data used by the outflow procedure for this problem. Furthermore, since the data is stepped to steady-state, this approach is general enough that it can also be used to provide the boundary data for both the Poisson and wave models.

We first compare the IAEM against the Boris method for the true steady-state problem described by the elliptic system

$$\begin{aligned} -\Delta\psi &= \frac{1}{\epsilon_0}\rho, \\ -\Delta A^{(3)} &= \mu_0 J^{(3)}, \end{aligned}$$

defined over free-space. An approach based on Green's functions is quite natural, as the free-space solution of this decoupled elliptic system is given explicitly by the volume integrals

$$\begin{aligned} \psi(\mathbf{x}) &= -\frac{1}{2\pi\epsilon_0} \int \ln(\|\mathbf{x} - \mathbf{x}'\|) \rho(\mathbf{x}') \, d\mathbf{x}', \\ A^{(3)}(\mathbf{x}) &= -\frac{\mu_0}{2\pi} \int \ln(\|\mathbf{x} - \mathbf{x}'\|) J^{(3)}(\mathbf{x}') \, d\mathbf{x}', \end{aligned}$$

which are taken over all of \mathbb{R}^2 with $\|\cdot\|$ being the usual Euclidean distance. The evaluation of these integrals can be performed efficiently with a fast summation method such as a tree-code [76] or fast multipole method [66], which is beyond the scope of the present work. Instead, we solve this elliptic system using second-order finite-differences with a sparse direct solver that enforces Dirichlet boundary conditions. Derivatives of the fields are computed with second-order finite-differences, as well. The Dirichlet data used in the elliptic solves is supplied by evolving the wave equations for the potentials with the BDF-1 method using outflow boundary conditions. While there are many possible approaches to this problem, it is important that this data be

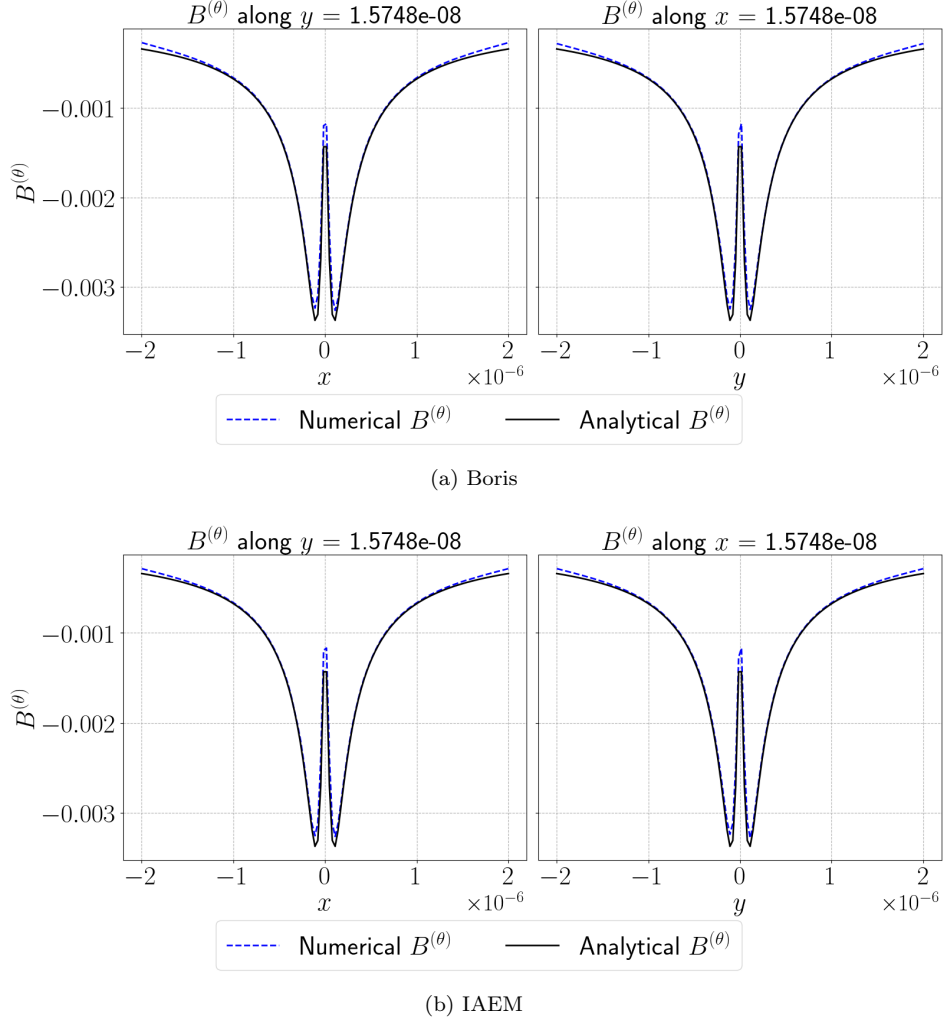


Figure 14: Cross-sections of the steady-state magnetic field $B^{(\theta)}$ for the Bennett problem with the Poisson fields. We compare the numerical fields against the analytical solution at 50 thermal crossing times. The results for the figure on the left were obtained with the Boris method, while the IAEM was used in the plot on the right. We observe good agreement in the magnetic field with its analytical solution.

updated at each time step so that the boundary data is consistent with the source. Our implementation of the Boris method uses an iterative approach for the current density to compute $v^{n+1/2}$. Based on some preliminary experiments, we found that no significant qualitative improvements in the results were achieved with more than 2 iterates. We applied both the Boris and IAEM solvers for 50 thermal crossings using a total of 2×10^6 steps, which gives a CFL ≈ 7.94 . For each species, we used 16,384 particles. In Figure 14, compare the fields generated with the Boris and IAEM after 50 thermal crossing times. We note that the CFL for this test is quite large for the first-order wave solver; however, we only use the data from the wave solver along the boundary of the simulation domain. In these regions, the fields are mostly flat, so this is an acceptable approximation, even with a diffusive solver. We observe good agreement in the fields around the axis of the beam, specifically in capturing the wells, where the gradients are a considerably larger.

Allowing for time variation in the fields requires that we now solve a system of two wave equations for

the potentials. These equations take the form of

$$\begin{aligned}\frac{1}{c^2} \frac{\partial^2 \psi}{\partial t^2} - \Delta \psi &= \frac{1}{\epsilon_0} \rho, \\ \frac{1}{c^2} \frac{\partial^2 A^{(3)}}{\partial t^2} - \Delta A^{(3)} &= \mu_0 J^{(3)},\end{aligned}$$

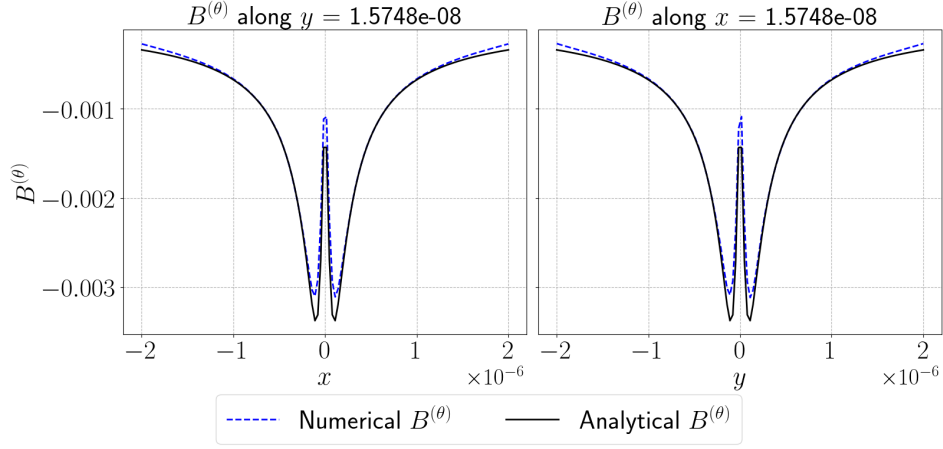
subject to outflow boundary conditions. The field contributions, which include both the potentials and their derivatives, are evaluated with the proposed BDF-1 solver. We applied the same iterative approach for the Boris method that was used to solve the Poisson equations in the elliptic formulation. Both solvers (Boris and IAEM) were applied for a total of 50 thermal crossings using 1×10^7 steps, which gives a CFL ≈ 1.59 . For each species, we used 16,384 particles, as with the elliptic formulation considered previously. In Figure 15, we show cross-sections of the Toroidal magnetic field B^θ computed with the BDF-1 wave solver using the formulations based on the Boris method and the IAEM. Compared to the elliptic formulation (see Figure 14), we observe some slight inaccuracies near the axis of the beam attributed to the use of a diffusive wave solver. The use of a finer mesh improves the quality of the solution in these regions, but necessitates additional time steps to avoid excessive CFL numbers and is beyond the capabilities of our existing implementation. Near the boundary, we can see a discrepancy with the analytical solution due to the approximate outflow boundary conditions used by the wave solver. Future work will focus on improving the accuracy of the solvers, so that the fields and their derivatives will be more accurate in these regions.

5.2.5 The Expanding Particle Beam

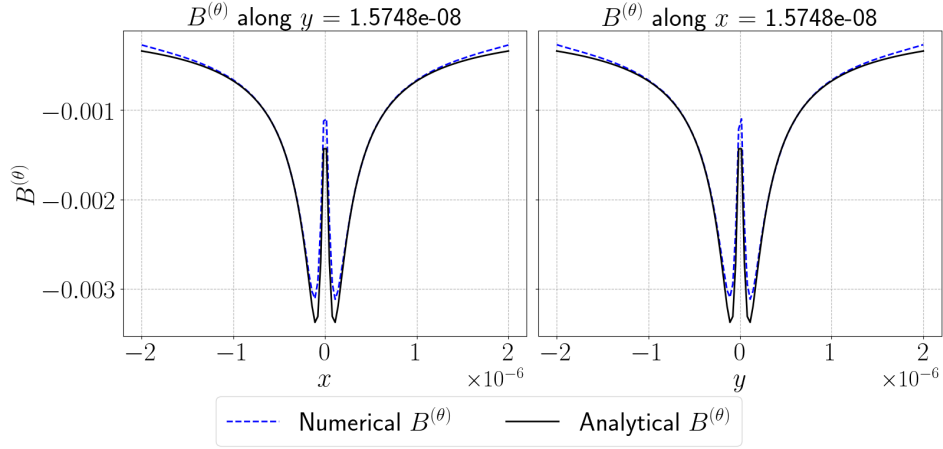
We now consider an application of the proposed methods to expanding particle beams [37]. This example is well-known for its sensitivity to issues concerning charge conservation, which makes it well-suited for evaluating methods used to enforce gauge conditions and involutions. While this particular example is normally solved in cylindrical coordinates, our simulation consists of a two-dimensional rectangular grid that retains the fields $E^{(1)}$ and $E^{(2)}$, as well as $B^{(3)}$. An injection zone is placed on one of the faces of the box and injects a steady beam of particles into the domain. The beam expands as particles move along the box due to the electric field and eventually settles into a steady-state. Particles are absorbed or “collected” once they reach the edge of the domain and are removed from the simulation. Along the boundary of the domain, the electric and magnetic fields are prescribed perfectly electrically conducting (PEC) boundary conditions, which, in two spatial dimensions, is equivalent to enforcing homogeneous Dirichlet boundary conditions on the potentials ψ , $A^{(1)}$, and $A^{(2)}$. Since the problem is PEC, there can be no (tangential) currents or charge on the boundary.

The equations considered for the fields and particles in this experiment are identical to those used in the 2D-2V (2D-2P) electromagnetic heating test discussed earlier in this section. As with the numerical heating experiment, the proposed methods were benchmarked using the popular FDTD-PIC method, which (again) adopts the TE mode convention; however, this selection for the staggering with the FDTD mesh is motivated by the PEC boundary conditions for the fields, which require $E^{(1)}$ to be zero along the x -axis and $E^{(2)}$ to be zero along the y -axis. Furthermore, since $B^{(3)}$ is cell-centered, its values along the boundary do not need to be specified. This leads to the staggered grid depicted in Figure 10. In our implementation of the FDTD-PIC method, we extend the $E^{(1)}$ field a half-cell in the x direction and the $E^{(2)}$ field a half-cell in the y direction. This ensures that $E^{(1)}$ and $E^{(2)}$ are positioned on the boundary and that $B^{(3)}$ remains on the interior of the domain. We note that this is not a requirement for the numerical heating problem, which uses periodic boundaries and therefore has no such half-cell extensions.

As discussed earlier, the Yee scheme is known to preserve the involutions of Maxwell’s equations in the absence of moving charge [21]; however, this is not applicable to the examples considered in this work. In order to update the fields, we need to map the current density components $J^{(1)}$ and $J^{(2)}$ to mesh points that are collocated with $E^{(1)}$ and $E^{(2)}$, respectively, according to the Yee mesh. It has been observed that the use of a bilinear map (also known as area weighting) for depositing current to the mesh results in serious errors due to violations of charge conservation [5]. The resulting fields cause the charged particles to “focus” in certain regions, leading to the appearance of striation patterns. An example is presented in Figure 16, which



(a) Boris



(b) IAEM

Figure 15: Cross-sections of the steady-state magnetic field $B^{(\theta)}$ for the Bennett problem in which wave equations are used to evolve the fields. The numerical fields are compared with the analytical steady-state solution for the fields at 50 thermal crossing times. The results for the figure on the left were obtained with the Boris method, while the IAEM was used in the plot on the right. We observe good agreement in the magnetic field with its analytical solution.

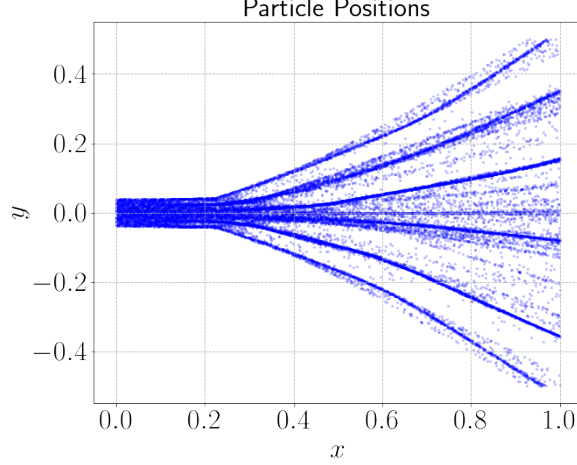


Figure 16: Striation patterns in an expanding beam simulated using the FDTD-PIC method with naive current scattering (area weighting). Irrotational errors in the electric field introduced by the mapping cause the particles to focus in regions of the domain. No cleaning method is used here.

shows the formation of the striations within twenty particle crossings using area weightings, though these patterns begin emerging as early as two crossings. Verbonceour [5] discusses a mapping for the current, which reduces the severity of these striations; however, after approximately ten crossings, smaller striations begin to form along the edge of the beam (see Figure 17a). These errors are strikingly similar to those discussed in [22], which considered applications to relativistic beams. To prevent the appearance of striations and other non-physical errors, they examined several divergence cleaning approaches. Among these, we chose to implement the Langdon-Marder divergence cleaning approach with the FDTD-PIC method. The effectiveness of the divergence cleaning step can be observed in Figure 17b along the beam edges. Using the cleaned fields, the position and velocity data for the particles can be updated with the Boris method discussed earlier.

To setup the simulation, we first create a box specified by the region $[0, 1] \times [-\frac{1}{2}, \frac{1}{2}]$, which has been normalized by some length scale L . We shall further assume that the beam consists only of electrons, which are prescribed some injection velocity $v_{\text{injection}}$ and travel along the x -axis of the box. An estimate of the crossing time for a particle can be obtained using the injection velocity and the length of the domain, which sets the time scale T for the simulation. The duration of the simulation is given in terms of particle crossings, which are then used to set the time step Δt . In each time step, particles are initialized in an injection region specified by the interval $[-L_{\text{ghost}}, 0] \times [-R_b, R_b]$, where R_b is the radius of the beam, and the width of the injection zone L_{ghost} is chosen such that

$$L_{\text{ghost}} = v_{\text{injection}} \Delta t.$$

This condition ensures that all particles initialized in the injection zone will be in the domain after one time step. Particle positions in the injection region are set according to samples taken from a uniform distribution, and the number of particles injected for a given time step is set by the injection rate. In each time step, the injection procedure is applied before the particle position update, so that, at the end of the time step, the injection zone is empty. To prevent the introduction of an impulse response in the fields due to the initial injection of particles, we apply a linear ramp function to the macro-particle weights over one particle crossing. The methods were applied using both wide and narrow beam configurations, whose parameters can be found in Tables 5 and 6, respectively.

The proposed method was compared against the FDTD-PIC method using the problem configurations specified according to Tables 5 and 6. Each simulation was evolved to a final time corresponding to 3000 particle crossings with a 128×128 mesh. A total of 4×10^6 time steps were used, which gave a CFL of ≈ 0.576 for the fields. In Figure 18, we plot the particle positions of the beams generated using the IAEM with the BDF-1 PIC solver and the FDTD-PIC method. We observe excellent agreement with the

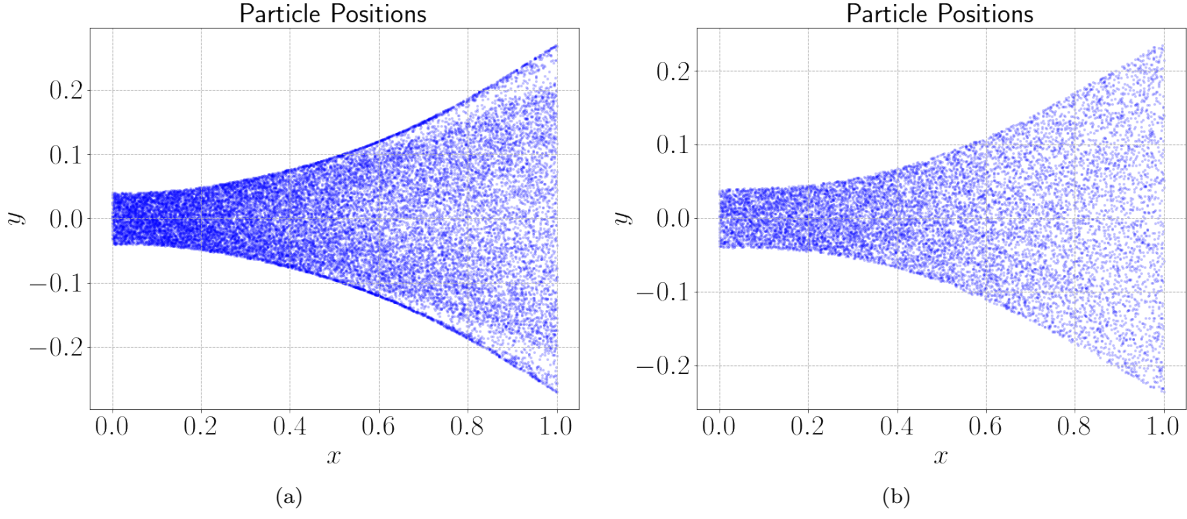


Figure 17: We demonstrate the effect of the divergence cleaning step on the structure of an expanding particle beam. The figure on the left uses the current mapping prescribed by Verboncoeur [5] without any divergence cleaning. The beam on the right is obtained using the same techniques in addition to the Langdon-Marder divergence cleaning approach presented in [22]. The additional cleaning step removes the smaller striations along the edge of the beam.

| Parameter | Value |
|--|-------------------------|
| Beam radius (R_b) [m] | 8.0×10^{-3} |
| Average number density (\bar{n}) [m^{-3}] | 7.8025×10^{14} |
| Largest box dimension (L) [m] | 1.0×10^{-1} |
| Electron injection velocity ($v_{\text{injection}}$) [m/s] | 5.0×10^7 |
| Electron crossing time (T) [s] | 2.0×10^{-9} |

Table 5: Table of the parameters used in the setup for the wide beam configuration.

| Parameter | Value |
|--|----------------------------|
| Beam radius (R_b) [m] | 8.0×10^{-3} |
| Average number density (\bar{n}) [m^{-3}] | 1.5522581×10^{14} |
| Largest box dimension (L) [m] | 1.0×10^{-1} |
| Electron injection velocity ($v_{\text{injection}}$) [m/s] | 5.0×10^7 |
| Electron crossing time (T) [s] | 2.0×10^{-9} |

Table 6: Table of the parameters used in the setup for the narrow beam problem.

benchmark FDTD-PIC method despite the first-order time accuracy of the method. Additionally, we find that the steady-state structure of the beam is well-preserved with the proposed method without the use of a divergence cleaning method. This provides a clear computational advantage over existing methods as it eliminates the need for solutions of auxiliary elliptic or parabolic equations for enforcing charge conservation. Additionally, the results presented for the IAEM were generated using simple bilinear maps for the charge and current densities without appealing to more intricate path integral mappings [5]. We find that the potentials and their spatial derivatives, which are (both) computed using the BDF-1 wave solver are quite smooth and do not show signs of excessive dissipation even after 3000 particle crossings. A collection of plots of the potentials and their spatial derivatives obtained with the proposed methods are displayed in figure 19. We show this data for the wide beam configuration provided in Table 5, and note that the results are quite similar for the narrow beam configuration provided in Table 6. While the goal of our work is to build higher-order field solvers for plasma applications, these results are interesting from the perspective of

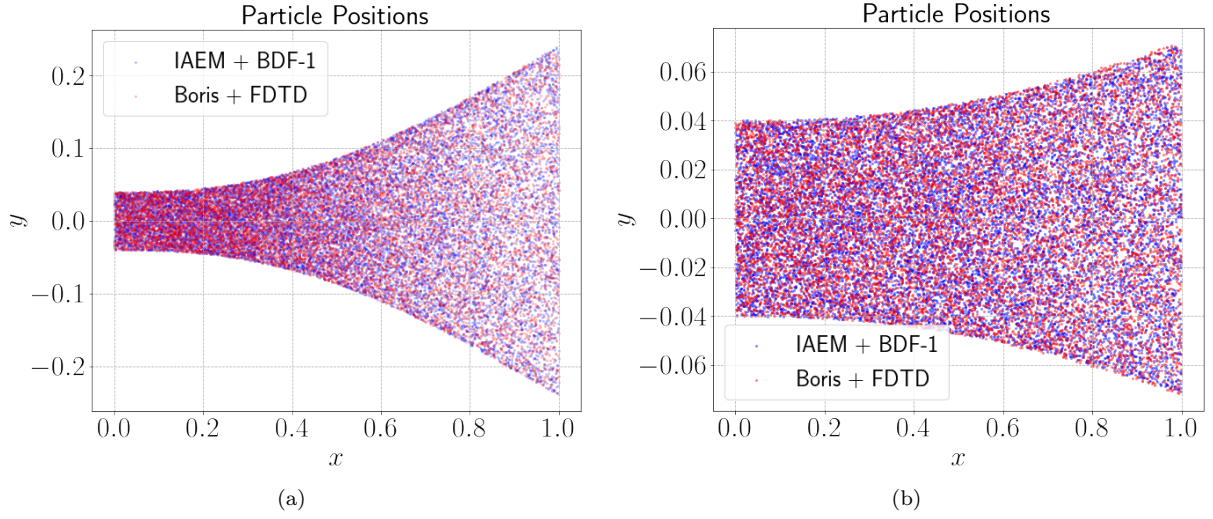


Figure 18: We compare the proposed PIC method against the standard FDTD-PIC method for the beam configurations specified in Tables 5 (shown on the left) and 6 (shown on the right). In each case, the particle positions generated by the two methods after 3000 crossings are plotted together to track the shape of the beam. The beams in the proposed methods remain intact after many particle crossings without the use of a cleaning method. Moreover, the beams generated by the proposed methods show excellent agreement with the beam profiles from the benchmark FDTD-PIC method.

practicality. More specifically, they demonstrate that it is possible to obtain a reasonable solution in a fairly inexpensive manner.

5.3 Summary

In this section, we presented a collection of numerical results for the proposed wave solver that demonstrate its application to a variety of wave propagation problems. This includes applications to plasmas, where the wave solver is used to update fields in a new PIC method that is based on a generalized momentum formulation. First, we analyzed the methods for evolving the potentials as well as the novel techniques for computing derivatives on the mesh. We considered several types of boundary conditions of relevance to the plasma examples presented in this work. In each case, the proposed methods for derivatives displayed space-time convergence rates that are identical to those of the wave solver used for the potentials. After establishing the convergence properties of the wave solver and the methods for derivatives, we then considered several applications involving plasmas using the new PIC method. The accuracy of the new PIC method was confirmed through a comparison of results obtained with standard PIC approaches. In particular, the new methods displayed superior numerical heating properties over the benchmark FDTD-PIC method used for electromagnetic problems. This seems to be true even in cases where the grid resolution is comparable to the plasma Debye length, which may allow for coarser grids to be used in PIC calculations. Additionally, the methods showed excellent agreement with the benchmark FDTD-PIC method for the expanding particle beam tests without resorting to the use of a divergence cleaning method. While current results are generally encouraging, aspects concerning the efficiency of the proposed methods will be explored in our future work.

6 Conclusions and Future Directions

In this paper, we developed a new PIC method for solving the Vlasov-Maxwell system. Using the Lorenz gauge condition, we expressed Maxwell's equations as a collection of wave equations for potentials, which

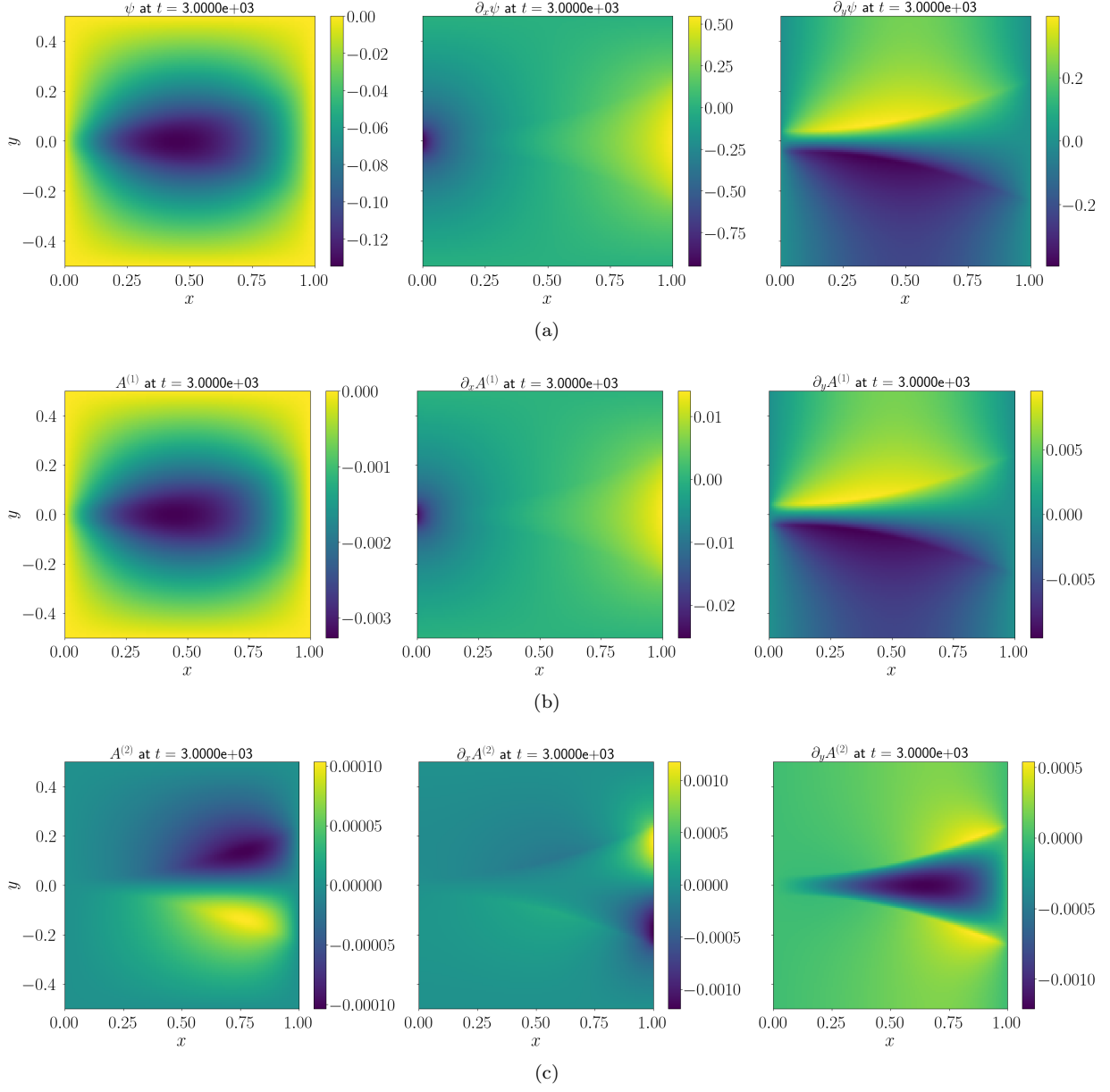


Figure 19: Here we show the potentials (and their derivatives) for the expanding beam problem with the parameters listed in Table 5. We show the fields after 3000 particle crossings and note that a divergence cleaning method is not used in this approach. In each row, we plot a field quantity and its corresponding derivatives. The top row shows the scalar potential ψ and its derivatives, while the middle and last row show the vector potential components $A^{(1)}$ and $A^{(2)}$, respectively, along with their derivatives. We can see that the proposed methods generate smooth fields for subsequent use in the particle updates.

are evolved on a co-located grid with a BDF wave solver. The equations of motion for the particles were also expressed in terms of these potentials as well as their spatial derivatives through the use of generalized momentum. We proved that the semi-discrete Lorenz gauge formulation considered in this work induces a corresponding semi-discrete equivalence between the Lorenz gauge condition and the continuity equation. Although this proof ignores errors due to dimensional splittings, our experimental results suggest that these effects are not significant. Additionally, the potential formulation naturally ensures that the involution $\nabla \cdot \mathbf{B} = 0$. Inspired by integral equation methods, we developed new approaches for the evaluation of spatial derivatives appearing in the particle updates. The proposed methodologies enjoy rates of convergence identical to the wave solver used to evolve the potentials and naturally inherit the stability and geometric flexibility offered by the BDF wave solver. The equations of motion for the particles in this formulation comprise a non-separable Hamiltonian system, which was solved using a semi-implicit Euler update that applies a (linear) Taylor correction. We applied the new PIC method, which combines the BDF wave solver (and related methods for derivatives) with the new particle advance, to a range of classic test problems, such as the two-stream instability, electrostatic and electromagnetic heating tests, the Bennett equilibrium pinch, and the expanding particle beam. We find that the new method performs notably better than traditional PIC methods in critical test problems such as numerical heating and the expanding particle beam and is indistinguishable to traditional PIC for the remaining problems. In particular, it is worth noting that, at the cost of an explicit method, the new algorithm displays mesh-independent heating properties. This suggests that it may be possible to perform PIC simulations using coarser grids than what is typically permitted by existing explicit codes. For example, when the mesh spacing is approximately 2.5 Debye lengths per cell, the new method heats less than one-tenth of a percent over 1000 angular plasma periods.

There are many interesting opportunities for improving the methods presented in this work. Naturally, we would like to develop high-order extensions, which requires new methods for the particles as well as higher-order methods for the fields. We have already started exploring higher-order alternatives for the field solver, which seems to necessitate cleaning methods to properly enforce the gauge condition. These results will be presented in a subsequent paper, which aims to establish a foundation for a family of high-order PIC methods. Though not explored in this work, the proposed methodologies for the derivatives naturally retain the geometric capabilities of the method used for the fields. This will allow us to study plasmas in certain devices with more complex geometric features. Other algorithms targeting non-separable Hamiltonian systems should be explored and compared with the results presented in this work. We remark that despite the added complexity (attributed to its non-separability), the generalized momentum formulation for the particles eliminates the need to compute the time derivatives of the vector potential. This provides an interesting opportunity for the potential development of new asymptotic preserving PIC methods [51]. Lastly, it would be interesting to consider (non-split) boundary integral formulations that utilize new fast summation methods [77, 78] developed for GPUs.

7 Acknowledgements

Some of the simulations presented in this work were supported by computational resources made available through the Institute for Cyber-Enabled Research at Michigan State University. Andrew Christlieb would like to thank both the Air Force Office of Scientific Research and the National Science Foundation for their support of our group under grants FA9550-19-1-0281, FA9550-17-1-0394, and DMS-1912183. The authors also would like to express their gratitude for the valuable feedback and suggestions offered by Professor John P. Verboncoeur of Michigan State University and Dr. John W. Luginsland at the Air Force Research Laboratory. Additionally, we would like to acknowledge the discussions with Dr. Eric M. Wolf, who provided us with sample codes that were helpful in our implementation of the Bennett pinch.

A Non-dimensionalization

In this section, we discuss the scalings used to non-dimensionalize the components of the models explored in this work. Our choice in exploring the normalized form of these models is simply to reduce the number of floating point operations with small or large numbers. We first non-dimensionalize the equations of motion for the particles, then focus on the field equations obtained with the Lorenz gauge. To minimize repetition, we shall illustrate the process for parts of the formulation and simply state the results for those that follow an identical pattern.

The setup for the non-dimensionalization process used in this paper considers the following substitutions:

$$\begin{aligned} \mathbf{x} &\rightarrow L\tilde{\mathbf{x}}, \quad t \rightarrow T\tilde{t}, \\ \mathbf{v} &\rightarrow V\tilde{\mathbf{v}} \equiv \frac{L}{T}\tilde{\mathbf{v}}, \quad \mathbf{P} \rightarrow P\tilde{\mathbf{P}} \equiv \frac{ML}{T}\tilde{\mathbf{P}}, \\ \psi &\rightarrow \psi_0\tilde{\psi}, \quad \mathbf{A} \rightarrow A_0\tilde{\mathbf{A}}, \\ \rho &\rightarrow Q\bar{n}\tilde{\rho}, \quad \mathbf{J} \rightarrow Q\bar{n}V\tilde{\mathbf{J}} \equiv \frac{Q\bar{n}L}{T}\tilde{\mathbf{J}}. \end{aligned}$$

Here, we use \bar{n} to denote a reference number density [m^{-3}], Q is the scale for charge in [C], and we also introduce M , which represents the scale for mass [kg]. The values for Q and M are set according to the electrons, so that $Q = |q_e|$ and $M = m_e$. We choose the scales for the potentials ψ_0 and A_0 to be

$$\psi_0 = \frac{ML^2}{QT^2}, \quad A_0 = \frac{ML}{QT}. \quad (99)$$

A natural choice of the scales for L and T are the Debye length and angular plasma period, which are defined, respectively, by

$$L = \lambda_D = \sqrt{\frac{\epsilon_0 k_B \bar{T}}{\bar{n} q_e^2}} \quad [\text{m}], \quad T = \omega_{pe}^{-1} = \sqrt{\frac{m_e \epsilon_0}{\bar{n} q_e^2}} \quad [\text{s/rad}],$$

where k_B is the Boltzmann constant, m_e is the electron mass, q_e is the electron charge, and \bar{T} is an average macroscopic temperature for the plasma. We choose to select these scales for all test problems considered in section 5 with the exception of the expanding beam problems, which are the last two test problems in that section. For these problems, the length scale L corresponds to the longest side of the simulation domain and T is the crossing time for a particle that is injected into the domain. Generally, the user will need to provide a macroscopic temperature \bar{T} [K] in addition to the reference number density \bar{n} to compute λ_D and ω_{pe}^{-1} . Note that the plasma period can be obtained from the angular plasma period T after multiplying the latter by 2π . Having introduced the definitions for the normalized variables, we proceed to non-dimensionalize the models, beginning with the equations for particles, before addressing the field equations for the potentials in the Lorenz gauge formulation.

A.1 Equations of Motion for the Generalized Hamiltonian

Here, we non-dimensionalize the generalized Hamiltonian model for the particles, which is given by equations (23) and (24). For convenience, these are given by

$$\begin{aligned} \frac{d\mathbf{x}_i}{dt} &= \frac{1}{m_i} (\mathbf{P}_i - q_i \mathbf{A}), \\ \frac{d\mathbf{P}_i}{dt} &= q_i \left(-\nabla\psi + \frac{1}{m_i} (\nabla\mathbf{A}) \cdot (\mathbf{P}_i - q_i \mathbf{A}) \right). \end{aligned}$$

Substituting the scales introduced at the beginning of the section into the position equation, and rearranging terms, we obtain

$$\frac{d\tilde{\mathbf{x}}_i}{d\tilde{t}} = \frac{1}{r_i} \left(\frac{TP}{ML} \tilde{\mathbf{P}}_i - \frac{QTA_0}{ML} \tilde{q}_i \tilde{\mathbf{A}} \right) \equiv \tilde{\mathbf{v}}_i.$$

This equation can be simplified further by using the definition of A_0 from (99) and noting that the scale for momentum is $P = MLT^{-1}$. Therefore, we obtain the non-dimensionalized position equation

$$\frac{d\tilde{\mathbf{x}}_i}{d\tilde{t}} = \frac{1}{r_i} \left(\tilde{\mathbf{P}}_i - \tilde{q}_i \tilde{\mathbf{A}} \right) \equiv \tilde{\mathbf{v}}_i.$$

Following an identical treatment for the generalized momentum equation and appealing to the definition (99), after some simplifications, we obtain

$$\frac{d\tilde{\mathbf{P}}_i}{d\tilde{t}} = \tilde{q}_i \left(-\tilde{\nabla}\tilde{\psi} + \frac{1}{r_i} \left(\tilde{\nabla}\tilde{\mathbf{A}} \right) \cdot \left(\tilde{\mathbf{P}}_i - \tilde{q}_i \tilde{\mathbf{A}} \right) \right).$$

Therefore, the non-dimensional system is (again, dropping tildes for simplicity)

$$\frac{d\mathbf{x}_i}{dt} = \frac{1}{r_i} \left(\mathbf{P}_i - q_i \mathbf{A} \right) \equiv \mathbf{v}_i, \quad (100)$$

$$\frac{d\mathbf{P}_i}{dt} = q_i \left(-\nabla\psi + \frac{1}{r_i} (\nabla\mathbf{A}) \cdot (\mathbf{P}_i - q_i \mathbf{A}) \right). \quad (101)$$

The next section presents the non-dimensionalization of the field equations obtained with the Lorenz gauge condition.

A.2 Maxwell's Equations in the Lorenz Gauge

Substituting scales introduced at the beginning of the section into the equations (8) - (10), we find that

$$\begin{aligned} \frac{1}{c^2} \frac{\psi_0}{T^2} \frac{\partial^2 \tilde{\psi}}{\partial \tilde{t}^2} - \frac{\psi_0}{L^2} \tilde{\Delta} \tilde{\psi} &= \frac{Q\bar{n}}{\epsilon_0} \tilde{\rho}, \\ \frac{1}{c^2} \frac{A_0}{T^2} \frac{\partial^2 \tilde{\mathbf{A}}}{\partial \tilde{t}^2} - \frac{A_0}{L^2} \tilde{\Delta} \tilde{\mathbf{A}} &= \frac{\mu_0 Q\bar{n}L}{T} \tilde{\mathbf{J}}, \\ \frac{A_0}{L} \tilde{\nabla} \cdot \tilde{\mathbf{A}} + \frac{1}{c^2} \frac{\psi_0}{T} \frac{\partial \tilde{\psi}}{\partial \tilde{t}} &= 0. \end{aligned}$$

The first equation can be rearranged to obtain

$$\frac{L^2}{c^2 T^2} \frac{\partial^2 \tilde{\psi}}{\partial \tilde{t}^2} - \tilde{\Delta} \tilde{\psi} = \frac{L^2 Q\bar{n}}{\epsilon_0 \psi_0} \tilde{\rho}.$$

Similarly, with the second equation we obtain

$$\frac{L^2}{c^2 T^2} \frac{\partial^2 \tilde{\mathbf{A}}}{\partial \tilde{t}^2} - \tilde{\Delta} \tilde{\mathbf{A}} = \frac{Q\bar{n}VL^2}{c^2 \epsilon_0 A_0} \tilde{\mathbf{J}},$$

where we have used $V = LT^{-1}$ as well as the fact that $c^2 = (\mu_0 \epsilon_0)^{-1}$. Finally, the gauge condition becomes

$$\tilde{\nabla} \cdot \tilde{\mathbf{A}} + \frac{\psi_0 V}{c^2 A_0} \frac{\partial \tilde{\psi}}{\partial \tilde{t}} = 0.$$

Introducing the normalized speed of light $\kappa = c/V$, and selecting ψ_0 and A_0 according to (99), we find that the above equations simplify to (dropping the tildes)

$$\frac{1}{\kappa^2} \frac{\partial^2 \psi}{\partial t^2} - \Delta \psi = \frac{1}{\sigma_1} \rho, \quad (102)$$

$$\frac{1}{\kappa^2} \frac{\partial^2 \mathbf{A}}{\partial t^2} - \Delta \mathbf{A} = \sigma_2 \mathbf{J}, \quad (103)$$

$$\nabla \cdot \mathbf{A} + \frac{1}{\kappa^2} \frac{\partial \psi}{\partial t} = 0, \quad (104)$$

where we have introduced the new parameters

$$\sigma_1 = \frac{M\epsilon_0}{QT\bar{n}}, \quad \sigma_2 = \frac{Q^2 L^2 \bar{n} \mu_0}{M}. \quad (105)$$

These are nothing more than normalized versions of the permittivity and permeability constants in the original equations.

B Elements of the Integral Solution

This section supplies additional details concerning the derivation and construction of methods to evaluate the integral solution used by the field solver proposed in this work. First, we discuss the recursive fast summation method, which computes the global convolution integral using an accumulation of local integrals. Then, we discuss the quadrature rules developed for the evaluation of these local integrals. We also provide an example that sketches the general development of such quadrature rules.

B.1 Fast Summation Method

In order to compute the inverse operators according to (46)-(48), suppose we have discretized the one-dimensional computational domain $[a, b]$ into a mesh consisting of $N + 1$ grid points:

$$a = x_0 < x_1 < \cdots < x_N = b,$$

with the spacing defined by

$$\Delta x_j = x_j - x_{j-1}, \quad j = 1, \cdots, N.$$

If we directly evaluate the function $w(x)$ at each of the mesh points, according to (47), we obtain

$$w(x_i) = \frac{\alpha}{2} \int_a^b e^{-\alpha|x_i-y|} f(y) dy + A e^{-\alpha(x_i-a)} + B e^{-\alpha(b-x_i)}, \quad i = 0, \cdots, N.$$

Since the evaluation of the integral term in the variable y requires with quadrature requires $\mathcal{O}(N)$ operations, this direct approach requires a total of $\mathcal{O}(N^2)$ operations. The cost of evaluating these terms can be reduced from $\mathcal{O}(N^2)$ to $\mathcal{O}(N)$ by first introducing the operators

$$\mathcal{I}_x^R[f](x) \equiv \alpha \int_a^x e^{-\alpha(x-y)} f(y) dy, \quad (106)$$

$$\mathcal{I}_x^L[f](x) \equiv \alpha \int_x^b e^{-\alpha(y-x)} f(y) dy, \quad (107)$$

so that the total integral over $[a, b]$ can be expressed as

$$\mathcal{I}_x[f](x) = \frac{1}{2} \left(\mathcal{I}_x^R[f](x) + \mathcal{I}_x^L[f](x) \right). \quad (108)$$

Then, the task now relies on computing these integrals in an efficient manner. To develop a recursive

expression, consider evaluating the right-moving convolution integral (106) at a grid point x_i . It follows that

$$\begin{aligned}
\mathcal{I}_x^R[f](x_i) &= \alpha \int_a^{x_i} e^{-\alpha(x_i-y)} f(y) dy, \\
&= \alpha \int_a^{x_{i-1}} e^{-\alpha(x_i-y)} f(y) dy + \alpha \int_{x_{i-1}}^{x_i} e^{-\alpha(x_i-y)} f(y) dy, \\
&= \alpha \int_a^{x_{i-1}} e^{-\alpha(x_i-x_{i-1}+x_{i-1}-y)} f(y) dy + \alpha \int_{x_{i-1}}^{x_i} e^{-\alpha(x_i-y)} f(y) dy, \\
&= e^{-\alpha\Delta x_i} \left(\alpha \int_a^{x_{i-1}} e^{-\alpha(x_{i-1}-y)} f(y) dy \right) + \alpha \int_{x_{i-1}}^{x_i} e^{-\alpha(x_i-y)} f(y) dy, \\
&\equiv e^{-\alpha\Delta x_i} \mathcal{I}_x^R[f](x_{i-1}) + \mathcal{J}_x^R[f](x_i).
\end{aligned}$$

In the last line, we have introduced the local integral

$$\mathcal{J}_x^R[f](x_i) = \alpha \int_{x_{i-1}}^{x_i} e^{-\alpha(x_i-y)} f(y) dy. \quad (109)$$

Through similar manipulations, one obtains the recursive expression for (107) given by

$$\mathcal{I}_x^L[f](x_i) = e^{-\alpha\Delta x_{i+1}} \mathcal{I}_x^L[f](x_{i+1}) + \mathcal{J}_x^L[f](x_i),$$

with

$$\mathcal{J}_x^L[f](x_i) = \alpha \int_{x_i}^{x_{i+1}} e^{-\alpha(y-x_i)} f(y) dy. \quad (110)$$

We see that the integrals can be expressed through a recursive weighting of an accumulated value plus an additional term that is localized in space. The recursive relations are initialized by setting

$$\mathcal{I}_x^R[f](x_0) = 0, \quad \mathcal{I}_x^L[f](x_N) = 0,$$

which follows directly from the definitions (106) and (107). Since the calculations of the local integrals (109) and (110) use quadrature over a collection of M points, the cost of evaluating each integral is now of the form $\mathcal{O}(MN)$. Additionally, since the number of localized quadrature points M is independent of the mesh size N , and we select $M \ll N$, the resulting approach scales as $\mathcal{O}(N)$. A similar argument is made for the other integral so that the final cost of evaluating their sum (108) is also $\mathcal{O}(N)$.

B.2 Approximating the Local Integrals

Here, we present the general process used to obtain quadrature rules for the local integrals defined by (109) and (110), in the case of a uniform grid, i.e.,

$$\Delta x = x_j - x_{j-1}, \quad j = 1, \dots, N.$$

Rather than use numerical quadrature rules, e.g., Gaussian quadrature or Newton-Cotes formulas, for purposes of stability, it was discovered that a certain form of analytical integration was required [68]. In this approach, the operand $f(x)$ is approximated by an interpolating function, which is then analytically integrated against the kernel. We provide a sketch of the approach to illustrate the idea. Specific details can be found in several papers, e.g., [47, 79].

First, it is helpful to transform the integrals (109) and (110) using a change of variable. Consider the integral (109) and let

$$y = (x_j - x_{j-1})\tau + x_{j-1} \equiv \Delta x\tau + x_{j-1}, \quad \tau \in [0, 1].$$

Then we can write

$$\mathcal{J}_x^R[f](x_i) = \alpha \Delta x e^{-\alpha\Delta x} \int_0^1 e^{\alpha\tau\Delta x} f(\tau\Delta x + x_{i-1}) d\tau. \quad (111)$$

Next, we approximate $f(x)$ in (111) using interpolation of some desired order of accuracy. As an example, suppose that we want to use linear interpolation with the data $\{f_{i-1}, f_i\}$ using the basis $\{1, x - x_{i-1}\}$, which is shifted for convenience to cancel with the shift in (111). A direct calculation shows that the interpolating polynomial is

$$p(x) = f_{i-1} + \frac{f_i - f_{i-1}}{\Delta x} (x - x_{i-1}).$$

By replacing f in (111) with the above interpolant, and integrating the result analytically, we find that

$$\begin{aligned} \mathcal{J}_x^R[f](x_i) &\approx \alpha \Delta x e^{-\alpha \Delta x} \int_0^1 e^{\alpha \tau \Delta x} \left(f_{i-1} + (f_i - f_{i-1}) \tau \right) d\tau, \\ &= w_0 v_{i-1} + w_1 v_i, \end{aligned}$$

where the weights for integration are

$$\begin{aligned} w_0 &= \frac{1 - e^{-\alpha \Delta x} - \alpha \Delta x e^{-\alpha \Delta x}}{\alpha \Delta x}, \\ w_1 &= \frac{(\alpha \Delta x - 1) + e^{-\alpha \Delta x}}{\alpha \Delta x}. \end{aligned}$$

Modifications of the above can be made to accommodate additional interpolation points, as well as techniques for shock capturing. In the latter case, methods have been devised following the idea of WENO reconstruction [80] to create quadrature methods that can address non-smooth features including shocks and cusps [79, 69, 81]. Additional details on the WENO quadrature, including the reconstruction stencils can be found in chapter 3. In [69], we developed a quadrature rule using the exponential polynomial basis, which offers additional flexibility in capturing localized features through a “shape” parameter introduced in the basis. These tools offer a promising approach to addressing problems with discontinuities in the material properties as well as more complex domains with non-smooth boundaries. Despite the notable differences in the type of approximating function used for the operand, the process is essentially identical to the example shown here. We also wish to point out that certain issues may arise when $\alpha \gg 1$ (i.e., $\Delta t \ll 1$). In such circumstances, when the weights are computed on-the-fly, the kernel function can be replaced with a Taylor expansion [52]. Otherwise, this results in a “narrow” Green’s function that is vastly under-resolved by the mesh, which causes wave phenomena to remain stagnant. Our experience has found this situation to be quite rare, but it is something to be aware of when a small CFL number is used in a simulation.

References

- [1] C. K. Birdsall and A. B. Langdon, *Plasma Physics via Computer Simulation*. McGraw-Hill Book Company, 1985.
- [2] R. W. Hockney and J. W. Eastwood, *Computer Simulation Using Particles*, First. CRC Press, 1988.
- [3] B. B. Godfrey, “Review and recent advances in PIC modeling of relativistic beams and plasmas,” *AIP Conference Proceedings*, vol. 1777, 1 2016.
- [4] S. Biedron, L. Brouwer, D. L. Bruhwiler, N. M. Cook, A. L. Edelen, D. Filippetto, C. K. Huang, A. Huebl, N. Kuklev, R. Lehe, S. Lund, C. Messe, W. Mori, C. -. Ng, D. Perez, P. Piot, J. Qiang, R. Roussel, D. Sagan, A. Sahai, A. Scheinker, F. Tsung, J.-L. Vay, D. Winklehner, and H. Zhang, *Snowmass21 accelerator modeling community white paper*, 2022.
- [5] J. P. Verboncoeur, “Particle simulation of plasmas: Review and advances,” *Plasma Physics and Controlled Fusion*, vol. 47, A231–A260, 5A 2005.
- [6] *Relativistic Plasma Simulation-Optimization of a Hybrid Code*, (Naval Research Laboratory, Washington, D. C.), 1970, pp. 3–67.
- [7] A. Langdon, B. Cohen, and A. Friedman, “Direct implicit large time-step particle simulation of plasmas,” *Journal of Computational Physics*, vol. 51, pp. 107–138, 1 1981.

- [8] J. Brackbill and D. Forslund, "An implicit method for electromagnetic plasma simulation in two dimensions," *Journal of Computational Physics*, vol. 46, pp. 271–308, 2 1982.
- [9] R. Mason, "An electromagnetic field algorithm for 2D implicit plasma simulation," *Journal of Computational Physics*, vol. 71, pp. 429–473, 2 1987.
- [10] B. Cohen, A. Langdon, D. Hewett, and R. Procassini, "An implicit method for electromagnetic plasma simulation in two dimensions," *Journal of Computational Physics*, vol. 81, pp. 151–168, 1 1989.
- [11] G. Lapenta, J. Brackbill, and P. Ricci, "Kinetic approach to microscopic-macroscopic coupling in space and laboratory plasmas," *Physics of Plasmas*, vol. 13, 5 2006.
- [12] S. Markidis and G. Lapenta, "The energy conserving particle-in-cell method," *Journal of Computational Physics*, vol. 230, pp. 7037–7052, 18 2011.
- [13] G. Chen, L. Chacón, and D. Barnes, "An energy- and charge-conserving, implicit, electrostatic particle-in-cell algorithm," *Journal of Computational Physics*, vol. 230, pp. 7018–7036, 18 2011.
- [14] D. Knoll and D. Keyes, "Jacobian-free Newton–Krylov methods: A survey of approaches and applications," *Journal of Computational Physics*, vol. 193, pp. 357–397, 2 2004.
- [15] G. Chen, L. Chacón, C. Leibs, D. Knoll, and W. Taitano, "Fluid preconditioning for Newton–Krylov-based, fully implicit, electrostatic particle-in-cell simulations," *Journal of Computational Physics*, vol. 258, pp. 555–567, 2014.
- [16] L. Chacón, G. Chen, and D. Barnes, "A charge-and energy-conserving implicit, electrostatic particle-in-cell algorithm on mapped computational meshes," *Journal of Computational Physics*, vol. 233, pp. 1–9, 2012.
- [17] G. Chen, L. Chacón, L. Yin, B. Albright, J. Stark, and R. Bird, "A semi-implicit, energy- and charge-conserving particle-in-cell algorithm for the relativistic Vlasov-Maxwell equations," *Journal of Computational Physics*, vol. 407, p. 109 228, 2020.
- [18] O. Koshkarov, L. Chacón, G. Chen, and L. F. Ricketson, "Fast nonlinear iterative solver for an implicit, energy-conserving, asymptotic-preserving charged-particle orbit integrator," *Journal of Computational Physics*, vol. 459, 2022.
- [19] G. Chen and L. Chacón, *An implicit, conservative and asymptotic-preserving electrostatic particle-in-cell algorithm for arbitrarily magnetized plasmas in uniform magnetic fields*, 2022.
- [20] K. S. Yee, "Numerical solution of initial boundary value problems involving Maxwell's equations in isotropic media," *IEEE Transactions on Antennas and Propagation*, vol. 14, pp. 302–307, 3 1966.
- [21] A. Taflov and S. C. Hagness, *Computational electrodynamics: the finite-difference time-domain method*, Third. Artech House Publishers, 2005.
- [22] P. Mardahl and J. Verboncoeur, "Charge conservation in electromagnetic PIC codes; spectral comparison of Boris/DADI and Langdon-Marder methods," *Computer Physics Communications*, vol. 106, pp. 219–229, 1997.
- [23] A. D. Greenwood, K. L. Cartwright, J. W. Luginsland, and E. A. Baca, "On the elimination of numerical Cerenkov radiation in PIC simulations," *Journal of Computational Physics*, vol. 201, pp. 665–684, 2 2004.
- [24] J.-L. Vay, R. Lehe, H. Vincenti, B. Godfrey, I. Haber, and P. Lee, "Recent advances in high-performance modeling of plasma-based acceleration using the full PIC method," *Nuclear Instruments and Methods in Physics Research Section A: Accelerators, Spectrometers, Detectors and Associated Equipment*, vol. 829, pp. 353–357, 2016, 2nd European Advanced Accelerator Concepts Workshop - EAAC 2015, ISSN: 0168-9002. DOI: <https://doi.org/10.1016/j.nima.2015.12.033>.
- [25] R. Lehe, M. Kirchen, I. A. Andriyash, B. B. Godfrey, and J.-L. Vay, "A spectral, quasi-cylindrical and dispersion-free particle-in-cell algorithm," *Computer Physics Communications*, vol. 203, pp. 66–82, 2016, ISSN: 0010-4655. DOI: <https://doi.org/10.1016/j.cpc.2016.02.007>.
- [26] J. P. Verboncoeur, "Aliasing of electromagnetic fields in stair step boundaries," *Computer physics communications*, vol. 164, pp. 344–352, 1 2004.

- [27] C. S. Meierbachtol, A. D. Greenwood, J. P. Verboncoeur, and B. Shanker, “Conformal electromagnetic particle in cell: A review,” *IEEE Transactions on Plasma Science*, vol. 43, 11 2015.
- [28] Y. Wang, J. Wang, Z. Chen, G. Cheng, and P. Wang, “Three-dimensional simple conformal symplectic particle-in-cell methods for simulations of high power microwave devices,” *Computer Physics Communications*, vol. 205, pp. 1–12, 2016.
- [29] B. Engquist, J. Häggblad, and O. Runborg, “On energy preserving consistent boundary conditions for the Yee scheme in 2D,” *BIT Numerical Mathematics*, vol. 52, pp. 615–637, 3 2012.
- [30] E. Sonnendrücker, J. Ambrosiano, and S. Brandon, “A finite element formulation of the Darwin PIC model for use on unstructured grids,” *Journal of Computational Physics*, vol. 121, pp. 281–297, 2 1995.
- [31] J. Eastwood, W. Arter, N. Brealey, and R. Hockney, “Body-fitted electromagnetic pic software for use on parallel computers,” *Computer Physics Communications*, vol. 87, pp. 155–178, 1-2 1995.
- [32] C.-D. Munz, P. Omnes, R. Schneider, E. Sonnendrücker, and U. Voss, “Divergence correction techniques for Maxwell solvers based on a hyperbolic model,” *Journal of Computational Physics*, vol. 161, no. 2, pp. 484–511, 2000.
- [33] G. Jacobs and J. Hesthaven, “High-order nodal discontinuous Galerkin particle-in-cell method on unstructured grids,” *Journal of Computational Physics*, vol. 214, pp. 96–121, 1 2006.
- [34] —, “Implicit–explicit time integration of a high-order particle-in-cell method with hyperbolic divergence cleaning,” *Journal of Computational Physics*, vol. 180, pp. 1760–1767, 10 2009.
- [35] M. Pinto, S. Jund, S. Salmon, and E. Sonnendrücker, “Charge-conserving FEM–PIC schemes on general grids,” *Comptes Rendus Mécanique*, vol. 342, pp. 570–582, 10-11 2014.
- [36] M. Pinto, K. Kormann, and E. Sonnendrücker, *Variational framework for structure-preserving electromagnetic particle-in-cell methods*, 2021. DOI: [10.48550/ARXIV.2101.09247](https://arxiv.org/abs/2101.09247). [Online]. Available: <https://arxiv.org/abs/2101.09247>.
- [37] S. O’Connor, Z. D. Crawford, J. P. Verboncoeur, J. Luginsland, and B. Shanker, “A set of benchmark tests for validation of 3-D particle in cell methods,” *IEEE Transactions on Plasma Science*, vol. 49, pp. 1724–1731, 5 Apr. 2021.
- [38] S. O’Connor, Z. D. Crawford, O. H. Ramachandran, J. Luginsland, and B. Shanker, “Time integrator agnostic charge conserving finite element PIC,” *Physics of Plasmas*, vol. 28, p. 092111, 9 Sep. 2021.
- [39] Z. D. Crawford, S. O’Connor, J. Luginsland, and B. Shanker, “Rubrics for charge conserving current mapping in finite element electromagnetic particle in cell methods,” *IEEE Transactions on Plasma Science*, vol. 49, pp. 3719–3732, 11 Nov. 2021.
- [40] Y. Saad and M. H. Schultz, “GMRES: A generalized minimal residual algorithm for solving nonsymmetric linear systems,” *SIAM Journal on Scientific and Statistical Computing*, vol. 7, pp. 856–869, 3 1986.
- [41] D. Appelö, L. Zhang, T. Hagstrom, and F. Li, “An energy-based discontinuous Galerkin method with tame CFL numbers for the wave equation,” 2021. DOI: [10.48550/ARXIV.2110.07099](https://arxiv.org/abs/2110.07099). [Online]. Available: <https://arxiv.org/abs/2110.07099>.
- [42] O. Beznosov and D. Appelö, “Hermite-discontinuous Galerkin overset grid methods for the scalar wave equation,” *Communications on Applied Mathematics and Computation*, vol. 3, pp. 391–418, 3 2021.
- [43] F. Zheng, Z. Chen, and J. Zhang, “A finite-difference time-domain method without the Courant stability conditions,” *IEEE Microwave and Guided Wave Letters*, vol. 9, pp. 497–523, 11 1999.
- [44] —, “Toward the development of a three-dimensional unconditionally stable finite-difference time-domain method,” *IEEE Transactions on Microwave Theory and Techniques*, vol. 48, pp. 1550–1558, 9 2000.
- [45] J. Lee and B. Fornberg, “Some unconditionally stable time stepping methods for the 3D Maxwell’s equations,” *Journal of Computational and Applied Mathematics*, vol. 166, pp. 497–523, 2 2004.
- [46] M. F. Causley, A. J. Christlieb, Y. Güçlü, and E. Wolf, “Method of lines transpose: A fast implicit wave propagator,” 2013. DOI: [10.48550/ARXIV.1306.6902](https://arxiv.org/abs/1306.6902). [Online]. Available: <https://arxiv.org/abs/1306.6902>.

- [47] M. Causley, A. Christlieb, and E. Wolf, “Method of lines transpose: An efficient unconditionally stable solver for wave propagation,” *Journal of Scientific Computing*, vol. 70, no. 2, pp. 896–921, 2017.
- [48] A. Christlieb, R. Krasny, J. Verboncoeur, J. Emhoff, and I. Boyd, “Grid-free plasma simulation techniques,” *IEEE Transactions on Plasma Science*, vol. 34, pp. 149–165, 2 2006.
- [49] M. Maïsek and P. Gibbon, “Mesh-free magnetoinductive plasma model,” *IEEE Transactions on Plasma Science*, vol. 38, pp. 2377–2382, 9 2010.
- [50] L. Siddi, G. Lapenta, and P. Gibbon, “Mesh-free Hamiltonian implementation of two dimensional Darwin model,” *Physics of Plasmas*, vol. 24, pp. 1–11, 8 2017.
- [51] Y. Cheng, A. J. Christlieb, W. Guo, and B. Ong, “An asymptotic preserving Maxwell solver resulting in the Darwin limit of electrodynamics,” *Journal of Scientific Computing*, vol. 71, no. 3, pp. 959–993, 2017.
- [52] M. F. Causley and A. J. Christlieb, “Higher order A-stable schemes for the wave equation using a successive convolution approach,” *SIAM Journal on Numerical Analysis*, vol. 52, no. 1, pp. 220–235, 2014.
- [53] A. J. Christlieb, P. T. Guthrey, W. A. Sands, and M. Thavappiragasm, “Parallel algorithms for successive convolution,” *Journal of Scientific Computing*, vol. 86, pp. 1–44, 1 2021.
- [54] M. Thavappiragasm, A. Christlieb, J. Luginsland, and P. Guthrey, “A fast local embedded boundary method suitable for high power electromagnetic sources,” *AIP Advances*, vol. 10, p. 115 318, 11 2020.
- [55] E. M. Wolf, M. Causley, A. Christlieb, and M. Bettencourt, “A particle-in-cell method for the simulation of plasmas based on an unconditionally stable field solver,” *Journal of Computational Physics*, vol. 326, pp. 342–372, 2016.
- [56] A. J. Christlieb, R. Krasny, and J. P. Verboncoeur, “A treecode algorithm for simulating electron dynamics in a Penning–Malmberg trap,” *Computer physics communications*, vol. 164, pp. 306–310, 1-3 2004.
- [57] —, “Efficient particle simulation of a virtual cathode using a grid-free treecode poisson solver,” *IEEE Transactions on Plasma Science*, vol. 32, pp. 384–389, 2 2004.
- [58] S. K. Veerapaneni, D. Gueyffier, D. Zorin, and G. Biros, “A boundary integral method for simulating the dynamics of inextensible vesicles suspended in a viscous fluid in 2D,” *Journal of Computational Physics*, vol. 228, pp. 2334–2353, 7 2009.
- [59] F. Vico, M. Ferrando, L. Greengard, and Z. Gimbutas, “The decoupled potential integral equation for time-harmonic electromagnetic scattering,” *Communications on Pure and Applied Mathematics*, vol. 69, pp. 771–812, 4 2016.
- [60] A. Barnett, L. Greengard, and T. Hagstrom, “High-order discretization of a stable time-domain integral equation for 3D acoustic scattering,” *Journal of Computational Physics*, vol. 402, p. 109 047, 2020.
- [61] S.-H. Chiu, M. N. J. Moore, and B. Quaife, “Viscous transport in eroding porous media,” *Journal of Fluid Mechanics*, vol. 893, A3, 2020. DOI: [10.1017/jfm.2020.228](https://doi.org/10.1017/jfm.2020.228).
- [62] M. C. A. Kropinski and B. D. Quaife, “Fast integral equation methods for Rothe’s method applied to the isotropic heat equation,” *Computers and Mathematics with Applications*, vol. 61, pp. 2436–2446, 9 2011.
- [63] M. Thavappiragasam, A. Viswanathan, and A. Christlieb, “MOLT based fast high-order three dimensional A-stable scheme for wave propagation,” *Journal of Coupled Systems and Multiscale Dynamics*, vol. 5, no. 2, pp. 151–163, 2017.
- [64] G. B. Folland, *Introduction to Partial Differential Equations: Second edition*. Princeton University Press; 1995, ISBN: 978-0691213033.
- [65] D. G. Duffy, *Green’s Functions with Applications*. CRC Press, 2001, ISBN: 978-1584881100.
- [66] L. Greengard and V. Rokhlin, “A fast algorithm for particle simulations,” *Journal of Computational Physics*, vol. 73, no. 2, pp. 325–348, 1987.

- [67] M. Causley, H. Cho, and A. Christlieb, “Method of lines transpose: Energy gradient flows using direct operator inversion for phase-field models,” *SIAM Journal on Scientific Computing*, vol. 39, no. 5, B968–B992, 2017.
- [68] M. Causley, A. Christlieb, B. Ong, and L. Van Groningen, “Method of lines transpose: An implicit solution to the wave equation,” *Mathematics of Computation*, vol. 83, no. 290, pp. 2763–2786, 2014.
- [69] A. Christlieb, W. Sands, and H. Yang, “A kernel-based explicit unconditionally stable scheme for Hamilton-Jacobi equations on nonuniform meshes,” *Journal of Computational Physics*, vol. 415, pp. 1–25, 2020, Art. No. 109543.
- [70] H. Kreiss, N. Petersson, and J. Yström, “Difference approximations of the Neumann problem for the second order wave equation,” *SIAM Journal of Numerical Analysis*, vol. 42, pp. 1292–1323, 3 2004.
- [71] E. Wolf, “A particle-in-cell method for the simulation of plasmas based on an unconditionally stable wave equation solver,” Ph.D. dissertation, Michigan State University, 2015.
- [72] R. Liboff, *Kinetic Theory: Classical, Quantum, and Relativistic Descriptions*. Springer-Verlag New York, 2003, ISBN: 978-0-387-95551-3.
- [73] S. Ichimaru, *Statistical Plasma Physics: Volume 1 Basic Principles*. CRC Press, 2004, ISBN: 978-0813341781.
- [74] W. H. Bennett, “Magnetically self-focussing streams,” *Phys. Rev.*, vol. 45, pp. 890–897, 12 Jun. 1934. DOI: [10.1103/PhysRev.45.890](https://doi.org/10.1103/PhysRev.45.890). [Online]. Available: <https://link.aps.org/doi/10.1103/PhysRev.45.890>.
- [75] J. A. Bittencourt, *Fundamental of Plasma Physics*, Third. Springer-Verlag, 2010.
- [76] J. Barnes and P. Hut, “A hierarchical $O(N \log N)$ force-calculation algorithm,” *Nature*, vol. 324, pp. 446–449, 1986.
- [77] N. Vaughn, L. Wilson, and R. Krasny, “A GPU-accelerated barycentric Lagrange treecode,” in *2020 IEEE International Parallel and Distributed Processing Symposium Workshops (IPDPSW)*, 2020, pp. 701–710. DOI: [10.1109/IPDPSW50202.2020.00125](https://doi.org/10.1109/IPDPSW50202.2020.00125).
- [78] L. Wilson, N. Vaughn, and R. Krasny, “A GPU-accelerated fast multipole method based on barycentric Lagrange interpolation and dual tree traversal,” *Computer Physics Communications*, vol. 265, 2021, ISSN: 0010-4655. DOI: <https://doi.org/10.1016/j.cpc.2021.108017>. [Online]. Available: <https://www.sciencedirect.com/science/article/pii/S0010465521001296>.
- [79] A. Christlieb, W. Guo, Y. Jiang, and H. Yang, “Kernel based high order explicit unconditionally-stable scheme for nonlinear degenerate advection-diffusion equations,” *Journal of Scientific Computing*, vol. 82:52, pp. 1–29, 3 2020.
- [80] G.-S. Jiang and C.-W. Shu, “Efficient implementation of weighted eno schemes,” *Journal of computational physics*, vol. 126, no. 1, pp. 202–228, 1996.
- [81] A. Christlieb, W. Guo, and Y. Jiang, “A WENO-based method of lines transpose approach for Vlasov simulations,” *Journal of Computational Physics*, vol. 327, pp. 337–367, 2016.